Superprotonic Solid Acids
Thermochemistry, Structure, and Conductivity

Thesis by

Ayako Ikeda

In Partial Fulfillment of the Requirements

For the Degree of

Doctor of Philosophy

California Institute of Technology

Pasadena, California

2013

(Defended August 10, 2012)

Acknowledgements

I got great help from many people to complete my research. I would like to state my appreciation in this section.

First, I thank my advisor, Dr. Sossina Haile for a lot of things. She gave me an opportunity to have very valuable experience in the U.S. She accepted me even though I had a language issue. I got strong support from her. The advice which she gave me was very valuable, not only for my research as a great scientist but also for my everyday life as a mother of young kids. I was very happy to join her group.

I thank Dr. Tetsuya Uda, who instructed me when I started my research as a volunteer. I could not get the idea that I can construct any measurement equipment by myself until he suggested I make humidified TG. I learned how to survive in the lab at that time as my first step.

I thank a machinist, Mike Vondrus for his great help and friendship. I could not build my measurement systems without his powerful help by his magical hands and deep knowledge. I thank his wife, Masako Vondrus for her kindness and friendship. I was very happy to meet them and spend time with them.

I thank Dr. Mary Louie, who was my labmate, for her kindness, help, advice and discussion. It was fun to spend time with her during trips for conferences. I thank Dr. Calum Chisholm and Dr. Dane Boysen for giving me advice, Dr. William Chow, Dr. Yoshihiro Yamazaki, and TaeSik Oh for giving me great suggestions and discussions.

I thank Chih-Kai Yang for helping my XRD duty a lot. Also, he encouraged me when we were taking ESL class together. I am so happy that both of us passed the SPEAK test just before my graduation.

I thank Jack Geasland for his big effort to teach me writing and speaking English.

I deeply thank Carolyn Richmonds for great help in checking up my English in the thesis. She kindly accepted the tough work with friendly smile. I could not have finished writing without her.

I would like to thank all my labmates and friends for their help and friendship.

Finally, I thank my husband, Teruyuki, for supporting me always with great patience and love. He helped me as my husband, our son's father, and a scientist.

Abstract

In this work, in order to investigate the thermochemistry and property of the superprotonic solid acid compounds, the measurement methods were established for in-situ observation, because superprotonic phases are neither stable at room temperature nor freezable to room temperature. A humidity-controlled TG, DSC and AC impedance measurement system, and high temperature stage for XRD were built for thermal analysis and characterization of the solid acid compounds.

The thermodynamic and kinetics of the dehydration and hydration of CsH_2PO_4 is investigated by TG, DSC, and XRD analysis. By making use of the enhanced kinetics afforded by SiO_2, the phase boundary between CsH_2PO_4, $CsPO_3$, and dehydrated liquid was precisely determined. The stability of CsH_2PO_4 and the liquid dehydrate, $CsH_{2(1-x)}PO_{4-x}$(l), were confirmed by the complete reversal of dehydration to recover these phases in the appropriate temperature and water partial pressure ranges. Rehydration and conversion of $CsPO_3$(s) to CsH_2PO_4(s) occurs over a period of several hours, depending on temperature, water partial pressure, and morphology of the metaphosphate. High and small particles favor rapid dehydration, whereas the temperature dependence of the rehydration kinetics is nonmonotonic, reaching its fastest rate in the vicinity of the superprotonic transition.

Doping Rb and K into CDP was examined and the stable region of $Cs_{1-x}Rb_xH_2PO_4$ and $Cs_{1-x}K_xH_2PO_4$ are determined by *in situ* XRD and DSC measurement. Then the effects of doping to the structure and conductivity are discussed. It was found that Rb has whole-range solubility for both cubic and monoclinic CDP. T_s increases and T_d decrease

with Rb content. K has 27% solubility for cubic CDP, T_s and T_d decrease with K content. The eutectic temperature is 208 ± 2°C. The lattice size of Rb- or K- doped CDP depends on the averaged cation size. Conductivity linearly decreases by dopant concentration. The impact of K doping is deeper than that of Rb for the equivalent averaged cation size.

In situ XRD measurement was carried out using single-crystal CsH_2PO_4 in order to study the phase transformation mechanism of this compound. A plate-like single crystal with (100) orientation was prepared, and the phase transition was observed by heating and cooling with ramp rate 0.2 K/min. From the obtained XRD profile — the after-first-phase transition (monoclinic→cubic) — the distribution of the domain orientation was estimated. It was found that (100) is the preferential orientation after phase transition, however, the amount of the domains with other orientation is not ignorable. Therefore, it is considered that the phase transformation in CsH_2PO_4 is not simple martensitic, but that some other event, such as recrystallization, happens during the transition process.

Table of contents

List of figures

List of Tables

List of Acronyms

ACIS alternating current impedance spectroscopy

CDP cesium dihydrogen phosphate, CsH_2PO_4

CHP cesium hydrogen phosphite, $CsHPO_3H$

CHS cesium hydrogen sulfate, CsHSO4

DSC Differential scanning calorimetry

DTA Differential thermal analysis

EDS energy dispersive spectroscopy

KDP potassium dihydrogen phosphate, KH_2PO_4

RDP rubidium dihydrogen phosphate, RbH_2PO_4

SEM scanning electron microscopy

TG Thermogravimetry

XRD X-ray diffraction

Chapter 1 Introduction

1.1 Overview

Solid acid compounds, which are composed of half normal salt and half acid, are solid-state materials with protons in the structure. An example is $CsHSO_4$, which is formed by the reaction of a cesium salt and sulfuric acid,

$$½Cs_2SO_4 + ½H_2SO_4 = CsHSO_4 \quad (1)$$

Solid acids have similar properties to salts in that they are brittle ionic crystals which are insulating at room temperature. Some of them are highly water soluble. One of the biggest differences between salts and solid acids is that most solid acid compounds are not truly stable at dry atmosphere. The reason that solid acid compounds can keep their form for a very long time in the laboratory is that the saturated water vapor pressure is too low at room temperature to cause rapid decomposition. It is known that some solid acid compounds have high proton conductivity phases, with proton conductivity higher than 1×10^{-3} $\Omega^{-1}cm^{-1}$, at elevated temperature. Such phases are called superprotonic, and the phase transformation from low to high conductivity phase; as called superprotonic transition. These compounds are attractive materials for fuel cell electrolytes because they are solid and are ideal for work in the moderate temperature range ($100 < T < 300$ °C). In this temperature range, it is expected that fuel cells can have both portability and high efficiency. In order to explore new fuel cell electrolyte materials and to reveal the origin of the high conductivity, several solid acid compounds have been investigated.

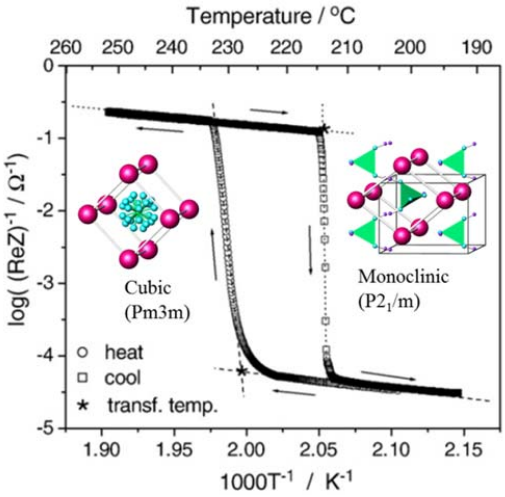

Figure 1.1. Conductivity change of CsH_2PO_4 with phase transition between cubic and monoclinic structure.[1]

Through these investigations, it was made clear that the rotation of the oxyanion has a major role in the proton migration of solid acid compounds. This oxyanion rotation rate strongly depends on the crystal structure. In cases where the compounds have high symmetry structures, the oxyanion can easily rotate because the lattice has many equivalent O atom sites. Protons in such high symmetry structured compounds can move with O atoms when the oxyanion rotates, which contributes to the high proton conduction in such compounds. However, in the case that the compounds have low symmetry structures, the rotation or movement of the oxyanion is restricted. Therefore, the proton jump rate from one site to another site is slow, and these compounds have low conductivity.

The explorations of the high conductivity compounds have been carried out primarily by AC impedance measurements within the form of a pellet or a single crystal. However, since solid acid compounds are not stable in a dry atmosphere and their decomposition rates at the tested temperatures are observably fast, it was hard to observe

pure superprotonic phases by more conclusive methods, like XRD or DSC analysis on their powder forms. Due to these difficulties, there is a lack of consistency in the literature on solid acids and their superprotonic phases. In these reports, the absence of knowledge of the thermochemistry of these compounds is apparent. In order to understand a variety of solid acid material properties, it is necessary for the compounds to be in equilibrium condition.

In this work, I present my efforts to obtain reliable data under equilibrium conditions. I built several measurement systems with humidification and developed methods to obtain reliable property data on solid acid compounds (mainly phosphates) in order to ascertain what conditions are necessary for high conductivity compounds with broader stable temperature region.

1.2 High-proton-conductive solid acid compounds and phase transition

The compounds which are reported as superprotonic, grouped by structure are:

- Cubic (Pm3m); CsH_2PO_4, RbH_2PO_4, CsH_2AsO_4[2] and $CsHPO_3H$[3]
- Tetragonal (I41/amd); $CsHSO_4$[4] and CsH_2PO_4[5]
- Hexagonal (P3m); $Cs_5H_3(SO_4)_4 \cdot nH_2O$, $Cs_5H_3(SeO_4)_4 \cdot nH_2O$[3], $K_5H_3(SO_4)_4 \cdot nH_2O$[3], $Rb_5H_3(SO_4)_4$

There are several mechanisms for proton migration. The first one is the combination of the rotation of oxyanion and the proton jump as typified by $CsHSO_4$[4] and CsH_2PO_4[5]. It is known that cubic phase CsH_2PO_4, RbH_2PO_4, CsH_2AsO_4[2], and $CsHPO_3H$[3], and tetragonal phase $CsHSO_4$ and $CsHSeO_4$[4] belong to this group.

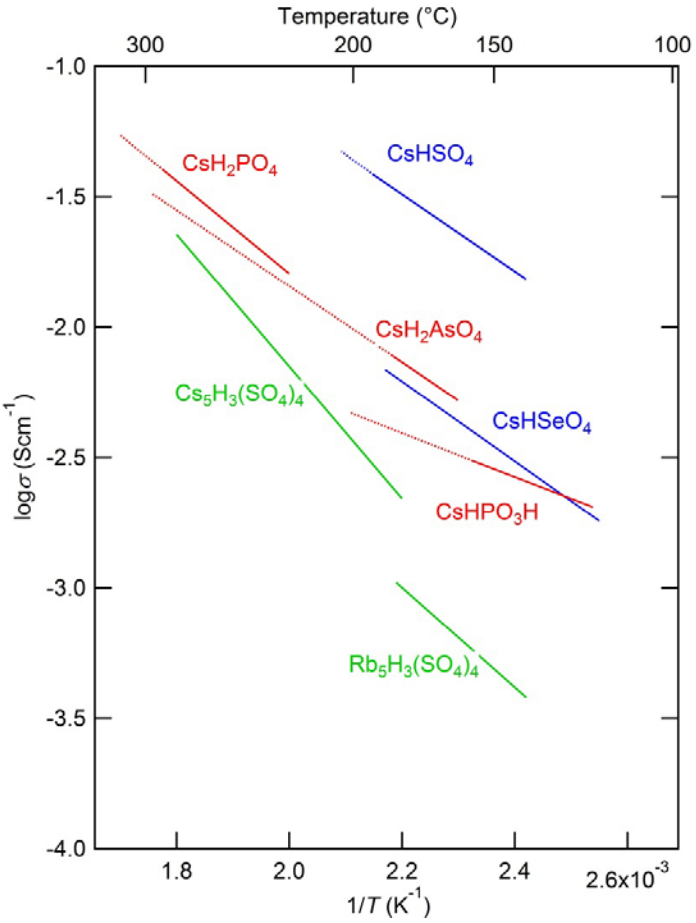

Figure 1.2. The conductivities of superprotonic phases of solid acid compounds (CsH_2PO_4[6], RbH_2PO_4, CsH_2AsO_4[2], $CsHPO_3H$[7], $CsHSO_4$[4], $CsHSeO_4$[4], $Cs_5H_3(SO_4)_4 \cdot nH_2O$[8], $Rb_5H_3(SO_4)_4$[9]; Red lines are cubic, blue lines are tetragonal and Green lines are hexagonal structured compounds. The broken lines are the extrapolation to melting temperatures.

The second one is the diffusion of the proton from crystal water as typified by $Cs_5H_3(SO_4)_4 \cdot nH_2O$[3]. It is known that $Cs_5H_3(SO_4)_4 \cdot nH_2O$, $Cs_5H_3(SeO_4)_4 \cdot nH_2O$[3] and $K_5H_3(SO_4)_4 \cdot nH_2O$[3] belong to this group of compounds[10]. The crystal water concentration depends on water vapor pressure as well as conductivity in this case. Recently, $Rb_5H_3(SO_4)_4$ was found to have the same crystal structure as this compound[9]. It is expected that its behavior in proton conduction is similar to $Cs_5H_3(SO_4)_4 \cdot nH_2O$ though it has been not studied yet. Figure 1.2 shows the conductivities of these compounds in the

corresponding temperature range. In this group of solid acid compounds, $CsHSO_4$ has the highest conductivity and $Rb_5H_3(SO4)_4$ has the lowest conductivity. The others have very similar conductivities at corresponding temperatures.

Since the superprotonic phases exist at high temperature (100~300°C), the phase transition events are observed during heating up or cooling down the sample. The enthalpy of the phase transitions agrees well with values calculated from the differences in the entropy, which is caused by the change of the proton configurations from ordered to random state.[11] Under the following rules, the configuration of the protons is expressed by Equation (2). [11]

(1) Each oxygen atom has two and only two protons.

(2) Each hydrogen bond has one and only one proton.

(3) The hydrogen bonds are directed towards the neighboring oxygen atoms.

(4) Interaction between nonneighboring H_2O molecules does not influence the distribution of hydrogen bond configurations.

The enthalpy change by phase transition is then described by Equation (3).

$$\Omega = \begin{pmatrix}\text{number of proton}\\ \text{configurations}\end{pmatrix} \times \begin{pmatrix}\text{probability a proton}\\ \text{site is open}\end{pmatrix}^{\begin{pmatrix}\text{number of}\\ \text{protons}\end{pmatrix}} \times \begin{pmatrix}\text{number of oxygen}\\ \text{positions}\end{pmatrix} \quad (2)$$

$$\Delta H_s = T_s \Delta S_s = T_s R \ln(\Omega) \quad (3)$$

The reported ΔH_{sp} for CsH2PO4 is 11.4 kJ/mol[12], and the calculated value is 11.7 kJ/mol. For $CsHSO_4$, the reported value is 6.11 kJ/mol, and the calculated is 6.15 kJ/mol.

1.3 Chemical stability

In order to operate a fuel cell with solid acid electrolyte, it is required that the electrolytes are stable under a hydrogen, oxygen, and humidified atmosphere. Unfortunately, all sulfates and serenates are not stable under a hydrogen atmosphere because they form H_2S or H_2Se. For example, cesium hydrogen sulfate and hydrogen gas react to form hydrogen sulfate[13] by the reaction,

$$\frac{1}{2}\ CsHSO_4(s) + H_2(g) \rightarrow \frac{1}{4}\ Cs_2SO_4(s) + H_2O(g) + \frac{1}{4}\ H_2S(s) \qquad (4)$$

Even worse, H_2S and H_2Se act to poison the platinum catalyst, leading to decreased activity of the fuel cell. Therefore these compounds are not suitable as electrolytes. Phosphates, phosphites and arsenates react with neither hydrogen nor oxygen below their melting temperature.

Since whole solid acid compounds have hydrogen and oxygen atoms in the structure, they dehydrate at certain temperatures. The dehydration temperatures of solid acid compounds depend on the water vapor pressure. For example, CsH_2PO_4 dehydrates at 290°C when p_{H2O} is 0.8 atm and at 240°C when p_{H2O} is 0.2 atm[14]. Some compounds pass liquid forms when these dehydrate with elevating the temperature as figure 1.3. This makes the rate of the dehydration reaction very slow. Many previous studies in the literature have inaccurately reported the dehydration of the solid acid as a phase change (melting) through their failure to note the weight change. In this study, I have defined the melting of solid acid compounds as the solid to liquid reaction occurring without weight loss. In order to operate the solid acid fuel cells, controlling the water vapor pressure of

the atmosphere in the cell is very important. In Chapter 3, the details of the dehydration behavior of CsH_2PO_4 are reported.

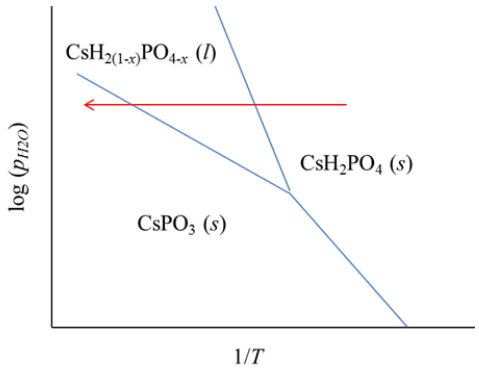

Figure 1.3. Dehydration process of CsH_2PO_4 during elevating temperature under the constant water vapor pressure

Because solid acid compounds have acids in the structure, they react with many metals and ceramics, as acids do at high temperatures. It is known that Pt, SiO_2, TiO_2, and some polymers are stable with solid acid compounds at high temperature. However, the number of compatible materials for use in the components of fuel cells, such as catalysts and electrodes, is very limited.

Most solid acid compounds are water soluble and some of these are deliquescent materials. The typical deliquescent compounds are $CsHPO_3H$ or $KHPO_3H$. These materials absorb water from the atmosphere very quickly and their solid forms are not stable under ambient atmosphere at room temperature. It is reported that these compounds can be stabilized by putting high surface area SiO_2 powder in the compounds[7] or nano-sized SiO_2[15]. On the other hand, the water insoluble compounds, $Ba_{3-x}K_xH_x(PO_4)_2$ (x~1.0, R3m:H[a]) is reported though it has relatively low conductivity (~$10^{-4}\Omega^{-1}cm^{-1}$)[16]. On the preliminary work, it is observed that the conductivity of this compound depends on the water vapor pressure.

1.4 Fuel cell application of solid acid compounds

CsH_2PO_4 is the most promising compound for fuel cell applications because it is stable under humidified hydrogen and oxygen gas atmosphere. The stack performance which was commercially developed by SAFCell was demonstrated as 250W (Figure 1.4).

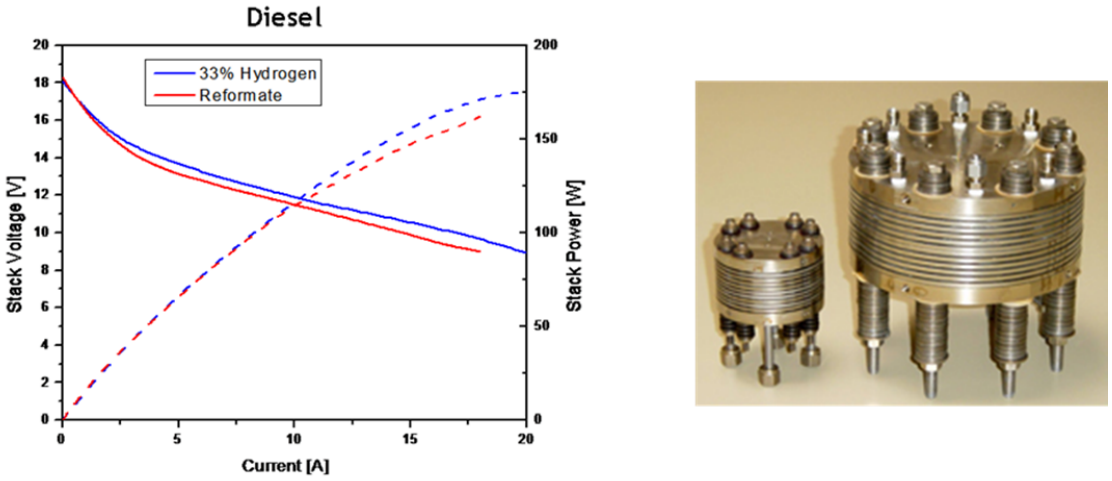

Figure 1.4. The fuel cell performance[17] of the commercial stack[17] (SAFCell)

In order to obtain higher efficiency operation of the fuel cell, catalysis of the cathode reaction is most important. Many approaches have been tried to improve the cathode performance by forming nanostructured CsH_2PO_4 to introduce a large area of contact area between the solid acid and the catalyst.[18,19] In such a fine structure, the kinetics of dehydration, recrystallization, and grain growth of CsH_2PO_4 are fast and obvious. In addition, the large surface area makes CsH_2PO_4 deliquescent. We can control dehydration and hydration if we have accurate thermodynamic information about the reaction. On the other hand, in order to prevent the destruction of the nanostructure by recrystallization, grain growth, or water absorption, support materials must be added. High-surface-area (nano) SiO_2[19] or PVP[18] are used for these purposes. It is known that the surface of SiO_2

absorbs water and it is used as a solid desiccant. Also, SiO_2 has good wettability with CsH_2PO_4[14].

Due to the narrow window of operation temperatures for CsH_2PO_4 (230~280 °C at p_{H2O} = 0.6 atm) new compounds for the fuel cell electrolytes in different temperature ranges have been explored. Doping is a common method for modifying the stable temperature region. For CsH_2PO_4, Rb and K doping were tried.[20,21] When CsH_2PO_4 is doped with Rb, the phase transition temperature increases and the dehydration temperature decreases. When CsH_2PO_4 is doped with K, both the phase transition temperature and dehydration temperature decrease. The lowest transition temperature achieved is just below 210 °C. However, it was found that the conductivity largely decreases with K doping.

Cubic $CsHPO_3H$, which is stable in the temperature range 120~200 °C[7], is another promising compound. It was found that by adding 20 at.% high-surface-area silica powder, the deliquescency of this compound at room temperature can be overcome. This composite has relatively high conductivity (~ 10^{-3} Scm^{-1}) in humidified atmosphere, and improvement of the conductivity is expected by decreasing the ratio of support materials. The advantages of this compound are that no dehydration happens, even under dry conditions, and no phase transition, which causes mechanical destruction by lattice mismatch between matrix and transformed domains of the fuel cell, happens unless it is kept dry.

Bibliography

1 Louie, M. W., Kislitsyn, M., Bhattacharya, K. & Haile, S. M. "Phase transformation and hysteresis behavior in $Cs_{1-x}Rb_xH_2PO_4$". *Solid State Ionics* **181**, 173-179, (2010).

2 Baranov, A. I., Khiznichenko, V. P. & Shuvalov, L. A. "High-Temperature Phase-Transitions and Proton Conductivity in Some KDP-Family Crystals". *Ferroelectrics* **100**, 135-141, (1989).

3 Chisholm, C. R. I., Merle, R. B., Boysen, D. A. & Haile, S. M. "Superprotonic phase transition in $CsH(PO_3H)$". *Chemistry of Materials* **14**, 3889-3893, (2002).

4 Baranov, A. I., Shuvalov, L. A. & Shchagina, N. M. "Superion Conductivity and Phase-Transitions in $CsHSO_4$ and $CsHSeO_4$ Crystals". *Jetp Letters* **36**, 459-462, (1982).

5 Baranov, A. I., Khiznichenko, V. P., Sandler, V. A. & Shuvalov, L. A. "Frequency Dielectric-Dispersion in the Ferroelectric and Superionic Phases of CsH_2PO_4". *Ferroelectrics* **81**, 1147-1150, (1988).

6 Ikeda, A., Kitchaev, D. & Haile, S. M. "Phase behavior of doped (Rb, K) cubic CsH_2PO_4". *Chemistry of the materials*, (2012).

7 Nagao, M., Ikeda, A. & Haile, S. M. "Proton conduction in $CsH(PO_3H)$ under dry or humid conditions". *ECS proceedings*, (2012).

8 Lavrova, G. V., Ponomareva, V. G. & Burgina, E. B. "Proton conductivity and structural dynamics in $Cs_5H_3(SO_4)_4/SiO_2$ composites". *Solid State Ionics* **176**, 767-771, (2005).

9 Panithipongwut, C. & Haile, S. M. "High-temperature phase behavior in the $Rb_3H(SO_4)_2$-$RbHSO_4$ pseudo-binary system and the new compound $Rb_5H_3(SO_4)_4$". *Solid State Ionics* **213**, 53-57, (2012).

10 Baranov, A. I., Sinitsyn, V. V., Vinnichenko, V. Y., Jones, D. J. & Bonnet, B. "Stabilisation of disordered superprotonic phases in crystals of the $M_5H_3(AO_4)_4 \bullet xH_2O$ family". *Solid State Ionics* **97**, 153-160, (1997).

11 Chisholm, C. R. I. & Haile, S. M. "Entropy evaluation of the superprotonic phase of $CsHSO_4$: Pauling's ice rules adjusted for systems containing disordered hydrogen-bonded tetrahedra". *Chemistry of Materials* **19**, 270-279, (2007).

12 Haile, S. M., Chisholm, C. R. I., Sasaki, K., Boysen, D. A. & Uda, T. "Solid acid proton conductors: from laboratory curiosities to fuel cell electrolytes". *Faraday Discussions* **134**, 17-39, (2007).

13 Uda, T., Boysen, D. A. & Haile, S. M. "Thermodynamic, thermomechanical, and electrochemical evaluation of $CsHSO_4$". *Solid State Ionics* **176**, 127-133, (2005).

14 Ikeda, A. & Haile, S. M. "The thermodynamics and kinetics of the dehydration of CsH_2PO_4 studied in the presence of SiO_2". *Solid State Ionics* **213**, 63-71, (2012).

15 Bondarenko, A. S., Zhou, W. & Bouwmeester, H. J. M. "Superprotonic $KH(PO_3H)$–SiO_2 composite electrolyte for intermediate temperature fuel cells". *Journal of Power Sources* **194**, 843-846, (2009).

16 Chisholm, C. R. I., Toberer, E. S., Louie, M. W. & Haile, S. M. "Engineering the Next Generation of Solid State Proton Conductors: Synthesis and Properties of $Ba_{3-x}K_xH_x(PO_4)_2$". *Chemistry of Materials* **22**, 1186-1194, (2010).

17 Safcell_Inc, http://www.safcell.com/_img/DieselPerformance.png

18 Varga, A., Brunelli, N. A., Louie, M. W., Giapis, K. P. & Haile, S. M. "Composite nanostructured solid-acid fuel-cell electrodes via electrospray deposition". *Journal of Materials Chemistry* **20**, 6309-6315, (2010).

19 Papandrew, A. B., Chisholm, C. R. I., Elgammal, R. A., Ozer, M. M. & Zecevic, S. K. "Advanced Electrodes for Solid Acid Fuel Cells by Platinum Deposition on CsH_2PO_4". *Chemistry of Materials* **23**, 1659-1667, (2011).

20 Louie, M. W., Kislitsyn, M., Bhattacharya, K. & Haile, S. M. "Phase transformation and hysteresis behavior in $Cs_{1-x}Rb_xH_2PO_4$". *Solid State Ionics* **181**, 173-179, (2010).

21 Ikeda, A. & Haile, S. M. "Examination of the superprotonic transition and dehydration behavior of $Cs_{0.75}Rb_{0.25}H_2PO_4$ by thermogravimetric and differential thermal analyses". *Solid State Ionics* **181**, 193-196, (2010).

Chapter 2 Experimental methods

2.1 Synthesis

For many water-soluble solid acid compounds, the most common method used to obtain the target compounds is precipitation. Generally, acids and carbonates are used as starting materials. An aqueous solution with stoichiometric ratio of the carbonate and acid is prepared and then the product is precipitated by evaporating the water or by adding organic solvents. In cases where the precipitation reaction occurs very quickly, small grains with uniform composition are obtained; however, sometimes secondary phases are formed as well. On the other hand, by the slow precipitation method it is possible to obtain very large crystals, as large as several centimeters. These large crystals are high purity and single phase.

For compounds that are insoluble in water, such like $BaHPO_4$, pH-controlled basic solutions are used for precipitation. Acetates are used for making the aqua-solution with alkali earth metal ions. In order to obtain large crystals of these compounds, it is necessary to control the precipitation rate. The gel method has been reported for this purpose. In this method, high viscosity liquid solution glass is filled to a tube, then the other solution is poured. Since ionic species in the high viscosity solution are provided very slowly, the precipitation rate can be controlled.

The melting method is favorable for solid solutions, such as $Cs_{1-x}Rb_xH_2PO_4$, or compounds with multiple anion species, for example, $Cs_3(H_2PO_4)(HSO_4)_2$. In this method, the starting material (a mixed powder) is heated to above its melting temperature (>

200 °C) in a sealed or humidified atmosphere to prevent decomposition. The product is then cooled down slowly. Here is the list of the synthesis methods for several solid acid compounds in Table 2.1.

Table 2.1. The synthesis methods (M = Cs, Rb, K, Na, Li, X = S, Se, A = Ba, Sr, Ca)

Method	Description	Compounds
Precipitation and grain growth in aqua-solution	Large single crystal available High purity	MH_2PO_4, $MHXO_4$, $M_3H(XO_4)_2$, $M_5H_3(XO_4)_4$, $MHPO_3H$, $A(H2PO_4)_2$
Rapid precipitation	Uniform composition Secondary phase formation Small grain size Water insoluble compounds OK	Aqua-solution with organic solvent: MH_2PO_4, $MHPO_3H$, $MHXO_4$ Two basic solutions: $AHPO_4$, $Ba_{3-x}K_xH_xPO_4$
Complete evaporation of aqua-solution	Easy to put additive (e.g. silica) Quick synthesis	CsH_2PO_4, $CsHPO_3H$
Melting method	Good for solid solutions	$Cs_2(H_2PO_4)(HSO_4)$, $Cs_{1-x}Rb_xH_2PO_4$

2.2 Thermogravimetry

Thermogravimetry (TG) is used to observe weight changes of a sample accompanying a change in temperature. This method can detect any reactions causing a mass change in the sample, such as decomposition, oxidation, or hydration. A TG system consists of a scale, thermocouple for the sample, and heaters which control the sample temperature. There are three configurations of components (Figure 2.1).

In this study, the hook type was adopted to introduce the controlled humidifier used in the investigation of the dehydration behavior of CsH_2PO_4. A schematic overview of the high-humidity TG system constructed in this work is shown in Figure 2.2 (a), and a photo of the actual setup is shown in (b). With the exception of the electronic balance, the

entire apparatus is placed inside an oven. The sample environment is humidified by flowing nitrogen gas at ~ 15 sccm through a heated water bath. The water partial pressure is measured at the outlet from the water bath using a humidity sensor (rotronic HygroLab), and the gas is then flowed into a heated quartz tube where the sample is located.

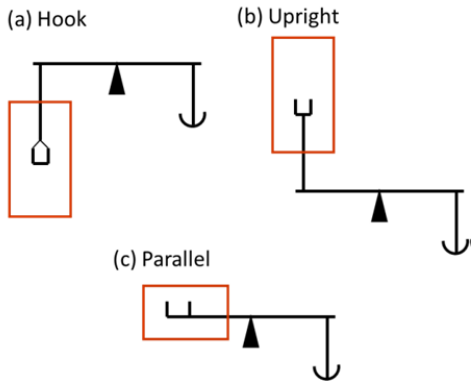

Figure 2.1. Balance/furnace configurations of TG.[1] (a) hook, (b)upright, and (c) parallel type

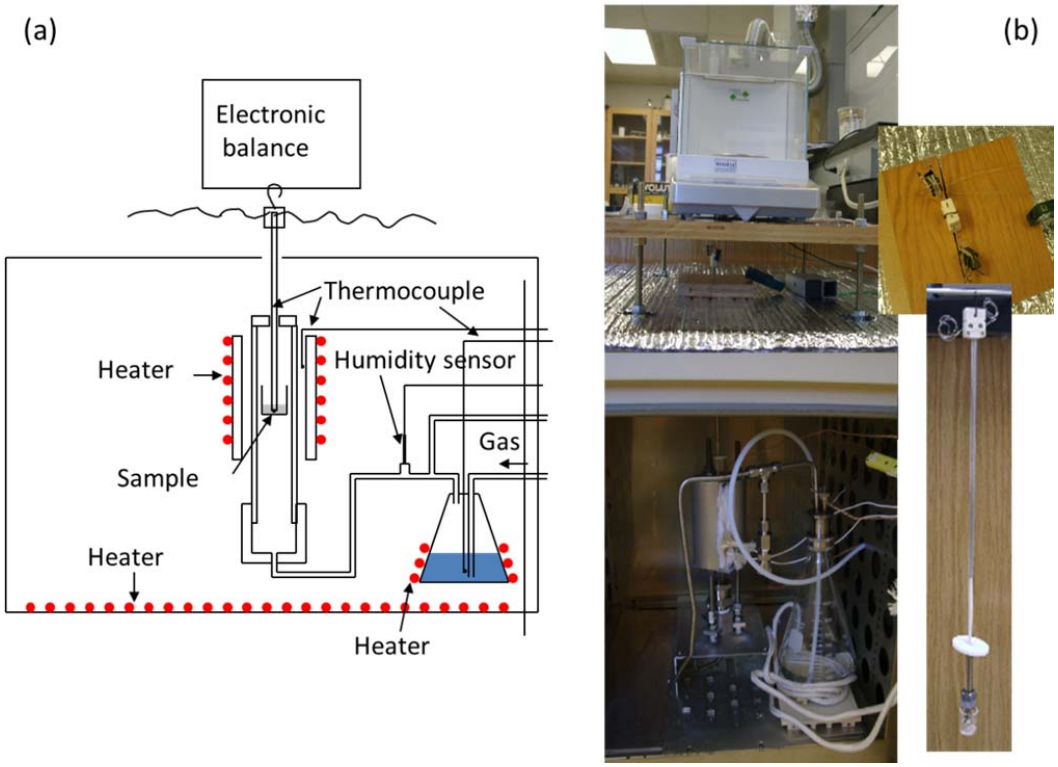

Figure 2.2. (a) Schematic view, (b) actual setup of the system

The humidity stability is ± 0.01 atm in water vapor pressure. The sample is placed in a Pt holder hung from a scale (Mettler Toledo AL54) with resolution ± 0.2 mg using a thermocouple (Type E). The sample weight used is 150 mg, implying a resolution in the weight measurement of 0.1%. The thermocouple junction is directly contacted to the bottom of the quartz glass sample holder to maximize accuracy in both the weight and temperature measurements. In order to obtain the reasonable result, measurement programs need to be considered carefully with appropriate ramp rate, dwell time or gas flow. Especially, in the case that the reaction of the sample is very slow, it is important to make sure the sample is in the equilibrium condition. TG analysis is a powerful method to obtain the equilibrium mass or reaction rate at certain temperatures.

2.3 Differential scanning calorimetry

Differential scanning calorimetry (DSC) is used to measure the heat production generated by the reaction of the sample. When heating or cooling a compound in the temperature range where a reaction occurs, the sample temperature may change as figure 2.3 (top). First, the sample temperature linearly changes. When the temperature reaches the reaction temperature, it remains constant while the reaction proceeds. Finally, after the reaction is finished, the temperature changes the same way as before the reaction occurred. By taking the differential between the sample and reference temperatures, the heat productionor absorption in the reaction is obtained as the area of the peak in figure 2.3 (bottom). The melting of pure metals (In, Sn, Pb, etc..) are used for calibration of heat flow.

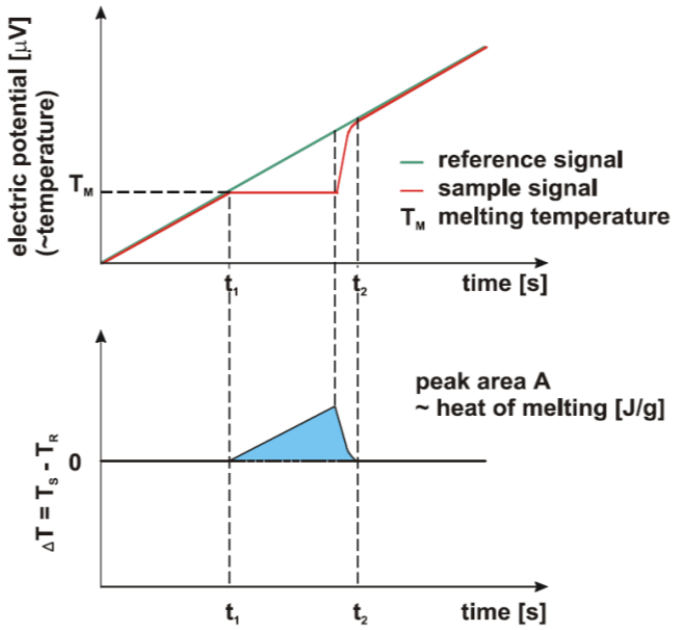

Figure 2.3. The principle of DSC measurement. (top) Temperature change of the sample and reference by heating. (bottom) The differential temperature between sample and reference. [2]

There are two principal types of DSC: power compensated and heat-flux. Figure 2.4 shows the schematic representation of these setups. A power compensated DSC maintains the temperature difference of zero between the sample and reference in the independent furnaces. The difference of the power consumptions between two furnaces is then monitored as the heat emission or absorption. In this method, the heat flow is obtained directly. A heat-flux DSC heats both the reference and the sample at same time with a single heater. The heat flow from the sample to the reference pan is monitored by a differential thermocouple which has two junctions on a heat flux disc at the sample and reference sides. The differential heat flow is proportional to the temperature difference between the two points. Resistance temperature detectors (RTDs) can be used here instead of thermocouples.

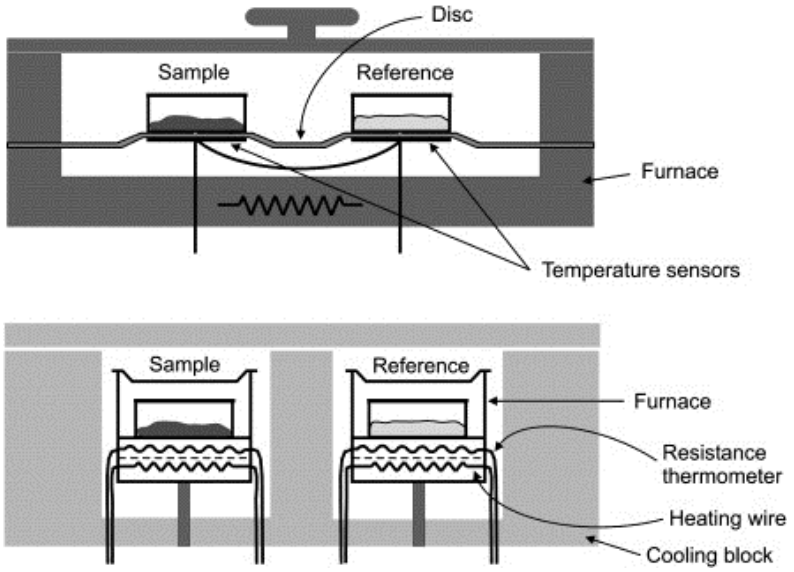

Figure 2.4. The schematic representation of the setup in heat flux DSC (top) and power compensation DSC (bottom) [3]

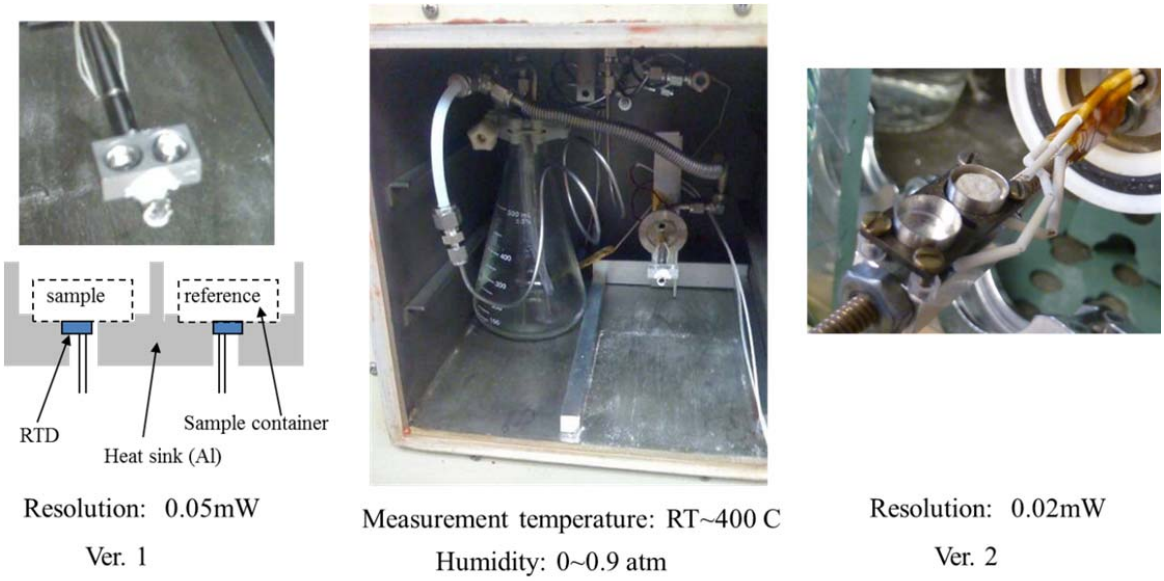

Figure 2.5. The actual setup of DSC system (center), ver.1 cell (left) and ver.2 cell (right)

In this work, a heat-flux DSC with the humidifier was built for investigation of solid acid compounds. For ver.1, RTDs are used for the sample cell and for ver.2, E-type thermocouples are used. Figure 2.5 shows the actual setup of the DSC system.

2.4 AC impedance spectroscopy

To obtain the ionic conductivity of solid electrolytes, AC impedance spectroscopy is usually used. When a DC voltage is applied to solid electrolytes, all movable ions migrate to the electrodes and then stop moving. On the other hand, when AC voltage is applied, the ions oscillate parallel to the direction of the potential gradient with a frequency that depends on the AC voltage frequency. The current $I(\omega)$ is measured and the impedance, $Z(\omega)$ is calculated from the voltage $E(\omega)$ and current as

$$Z(\omega) = \frac{E(\omega)}{I(\omega)} \tag{1}$$

where ω is the frequency of the AC voltage. The absolute value of the impedance $|Z|$ can be obtained by the measured voltage, current, and phase difference θ (obtained from delay of signals). The impedance of a solid electrolyte is equivalent to a parallel circuit of resistance R and capacitance C (Figure 2.6); this impedance is analytically expressed by equation (2).

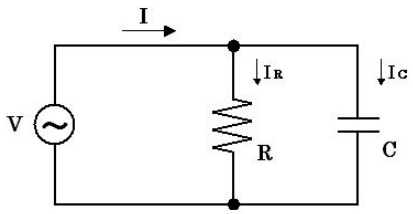

Figure 2.6. The equivalent circuit (parallel of R and C) of solid electrolyte

$$Z = \frac{R}{1 + i\omega CR} \tag{2}$$

By transforming Equation (2), the relation between Z_r, the real component of Z, and Z_i, the imaginary component, is expressed as equation (3).

$$\left(Z_r - \frac{R}{2}\right)^2 + Z_i^2 = \left(\frac{R}{2}\right)^2 \quad (3)$$

In the case of solid acid compounds, the impedance profiles are shown on a Cole-Cole Plot as in Figure 2.7(a) for low conductivity and (b) for superprotonic phase. In the profile, the resistance of the electrolyte appears as the diameter of the semicircle. However, in the case of superprotonic phase, the semicircle is not observed because the proton mobility is very large. Here the conductivities of the superprotonic phases are calculated as the distance between real axis and the plots, as shown in Figure 2.7(b).

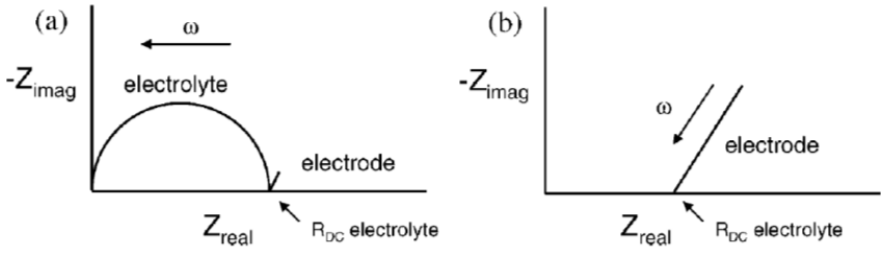

Figure 2.7. The impedance profiles of low conductivity and superprotonic phases of solid acid compounds.[4]

2.5 Energy-dispersive spectroscopy

Energy-dispersive spectroscopy (EDS) is used to evaluate the elemental composition of the sample. The accuracy of composition given by this method is better for materials composed of heavier elements and poor for materials consisting of elements lighter than potassium. The measurement results are also affected by the surface conditions of the sample or the angle at which the electron beam strikes the sample surface plain. For solid acid compounds, the measurements are carried out on the powder

form of the sample. Since many compounds are destroyed by the electron beam, lower accelerating voltages (< 10 kV) are suitable. When the sample contains two phases, they can be distinguished from the back-scattered electron image (Figure 2.8).

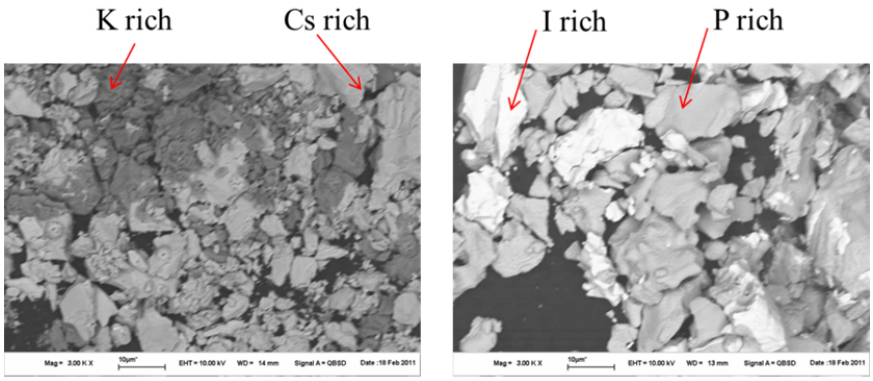

Figure 2.8. The back scattered electron image of the annealed and quenched composite of (left) CsH_2PO_4 : KH_2PO_4 (7:3), (right) CsH_2PO_4 : CsI

The solubility limit of the dopant elements are measured by the annealing and quenching method as follows:

- A composite is annealed at certain temperature under humidified atmosphere.
- It is rapidly cooled by putting the sample container into a water bath.
- The phases are identified from the back scattered electron image.
- EDS measurements are carried out on the phases.
- The composition is determined by the results of at least five measurement points.

2.6 Lattice parameter refinement

Powder X-ray diffraction analysis is a powerful method for characterizing phases and obtaining structure parameters. Structure parameters can be obtained very precisely

by using Nelson-Riley extrapolation method or by combination of the internal standard and Rietveld refinement.

The high temperature sealed stage was built to keep samples from dehydration while observing the superprotonic phases of solid acid compounds. Figure 2.9 shows the actual setup of the stage. In this system, the sample is sealed and the chamber wall is heated to around 150 °C. A drop of water is placed inside the chamber and the water evaporates, providing humidity. The inside gas pressure is controlled by a check valve so as not to exceed 1.2 atm. The sample is heated separately from the chamber by an embedded heater in the stage.

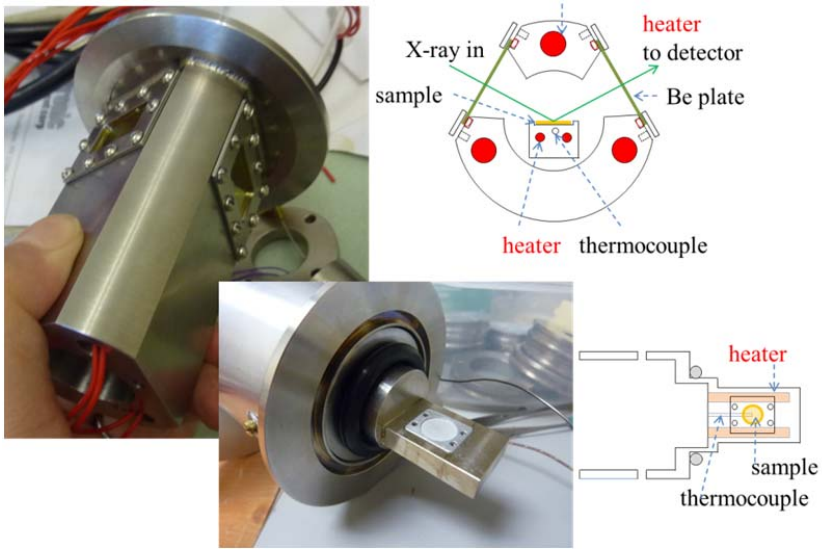

Figure 2.9. The actual setup of the high temperature sealed stage for XRD.

2.6.1 Nelson-Riley extrapolation method[5]

The main cause of peak shifts in XRD profiles is sample displacement which is perpendicular to diffraction surface of the sample (Figure 2.10).

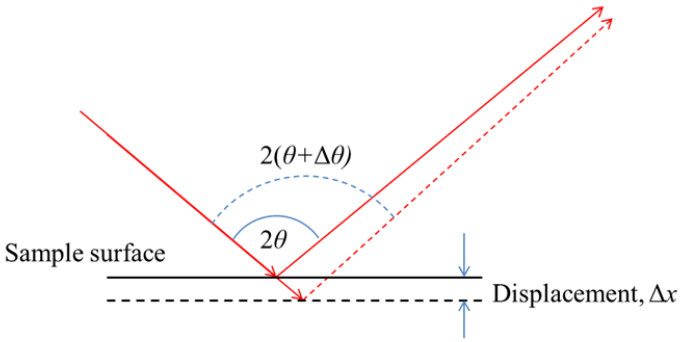

Figure 2.10. The relation of the sample displacement and the error in the angle

The error of the plane distance Δd which is obtained from each peak location 2θ is expressed by Nelson-Riley equation as Equation (4).

$$\frac{\Delta d}{d} = K\left(\frac{\cos^2\theta}{\sin\theta} + \frac{\cos^2\theta}{\theta}\right) \tag{4}$$

Where K is constant value which is corresponding to Δx. The contents of the parentheses in Equation (4) are called the Nelson-Riley parameter. Figure 2.11 shows an example of a plot of the lattice parameter obtained from the peaks of an actual measurement for a cubic structured compound. In this method, the extrapolation to zero for Nelson-Riley parameter gives the true lattice parameter. Usually, the smaller 2θ gives the scattered value against the fitting line. Therefore, the peaks which are located in larger 2θ value than 60° are very important. If the sample does not have a cubic structure, it is necessary to pick specific peaks to obtain each parameter. The number of such peaks is not large like cubic phases. For example, in order to determine two lattice parameters a and c in a tetragonal phase, the calculation should be carried out on the (hk0) peaks for the a value and on (00l) for the c value. In this work on the cubic phase of CsH_2PO_4, unfortunately, the intensity of peaks at 2θ angles greater than 60° is very small; therefore, this method was not applied for the lattice parameter refinement.

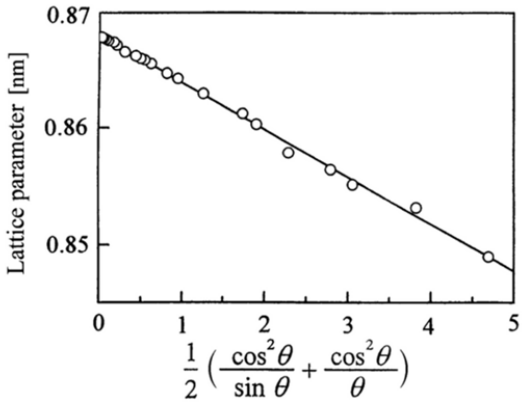

Figure 2.11. Extrapolation of measured lattice parameters using the Nelson-Riley method[6]

2.6.2 Internal standard

By addition of a compound with a well-known lattice parameter into the sample, the experimental errors of the angle can be corrected using the peaks from the known compound. Si, SiO_2 or Al_2O_3 are commonly used for this purpose as internal standard materials. The requirements for internal standard materials are:

- Minimum overlap of peaks from the internal standard with those of sample
- Low number of the peaks
- No reaction between the standard material and sample

In this work, Si is used as internal standard with CsH_2PO_4 and related compounds. No reaction between Si and samples were observed at the measurement temperature (~300°C).

2.6.3 Rietveld refinement

Rietveld method is used to refine the structure by finding the parameters which give the minimum difference between the measured and simulated profiles. In this study,

the lattice constants of solid acid phases were obtained by this method using RIETAN-FP software[7]. The parameters which were refined by this method are shown in Table 2.2.

Table 2.2. The parameters which are refined using Rietveld method

Description	Parameters	Note
lattice parameters	a, b, c, β	$a = b = c$, $\beta = 90°$ for cubic
scale factors	s	
FWHM parameters	u, v, w	
mixing parameters	eta_1, eta_2, eta_3, eta_4	
asymmetry	a_0, a_1, a_2	
scale factors	s	
background	b_0, b_1, b_2, b_3, b_4, b_5, b_6	
peak shift parameter	t_0, t_1, t_2, t_3	
atomic parameters	occupancy, g	
	coordinate, x, y, z	
	isotopic atomic displacement, B_{11}, B_{12}, B_{13}, B_{22}, B_{23}, B_{33}	$B_{11} = B_{22} = B_{33}$, $B_{12} = B_{13} = B_{23} = 0$ for cubic

Since the peak intensities of XRD profiles of superprotonic phases in the large angle region ($2\theta > 60°$) are very small, internal standard method was adopted in order to obtain the precise lattice constants. When lattice parameters of one of the phases are known, reasonable values of the peak shift parameters can be determined because the peak shift parameters and the lattice constants are not independent. In this study, Si powder was used in samples as the internal standard. The fixed values are used for all Si phase parameters except for the scale factor in the calculations. The reported value is applied for the Si lattice constant at each temperature. The other parameters for Si phase are determined from independent measurements at each temperature. The atomic coordinate, x, y, z for O atoms is restricted to be the distance which between P and O atoms is equal to 1.52 Å.

Bibliography

1 Price, D., www.sump4.com/downloads/TGA.ppt

2 Netzsch, http://www.benelux-scientific.be/fileadmin/user_files/pdf/workshop_netzsch2009/intro_to_thermal_analysis.pdf

3 Bunjes, H. & Unruh, T. "Characterization of lipid nanoparticles by differential scanning calorimetry, X-ray and neutron scattering". *Advanced Drug Delivery Reviews* **59**, 379-402, (2007).

4 Haile, S. M., Chisholm, C. R. I., Sasaki, K., Boysen, D. A. & Uda, T. "Solid acid proton conductors: from laboratory curiosities to fuel cell electrolytes". *Faraday Discussions* **134**, 17-39, (2007).

5 Cullity, B. D. *ELEMENTS OF X-RAY DIFFRACTION 3rd edition*. 326 (1956).

6 Yoshio Waseda, E. M., Kozo Shinoda. *X-Ray Diffraction Crystallography: Introduction, Examples and Solved Problems*. (2011).

7 Izumi, F. & Momma, K. "Three-dimensional visualization in powder diffraction". *Applied Crystallography XX* **130**, 15-20, (2007).

Chapter 3 Dehydration-hydration of CsH_2PO_4 [1]

3.1. Introduction

Under sufficient humidification, the compound CsH_2PO_4 transforms at 228 °C and 1 atm total pressure to a stable, cubic phase of high conductivity, recognized as the superprotonic phase. The conductivity in the superprotonic state renders CsH_2PO_4 an attractive material for fuel cell and other electrochemical applications [2]. As discussed in a recent overview of the literature regarding the high temperature properties of CsH_2PO_4, some have suggested that the jump in conductivity at the purported transition is an artifact of dehydration, but the evidence in favor of a polymeric transformation is overwhelming [3]. Essential to the observation and utilization of the superprotonic phase is the application of sufficient humidity so as to prevent the dehydration that otherwise occurs under ambient levels of humidification above the transition temperature [2]. Several recent studies have appeared describing the dehydration thermodynamics and kinetics of CsH_2PO_4. The first semi-quantitative study was that of Boysen [2] who reported the dehydration temperature of CsH_2PO_4 at selected water vapor pressures (over the T and p_{H_2O} ranges 205~280 °C and 0.01~0.35 atm, respectively) by detecting, in closed chamber cells, small humidity increases resulting from dehydration. Taninouchi et al. determined the dehydration temperature through a combination of thermogravimetric analysis and conductivity measurements at p_{H_2O} = 0.008 ~ 0.4 atm [4-6]. At temperatures below 265 °C and water partial pressures below 0.22 atm, CsH_2PO_4 was observed to undergo direct dehydration to the solid product $CsPO_3$. At higher p_{H_2O} and intermediate temperatures, however, a stable liquid product corresponding to incomplete dehydration

($CsH_{2(1-x)}PO_{4-x}$(*l*) with *x* close to 0.4 but dependent on p_{H_2O}) was detected. Thus, a triple point corresponding to the three-phase equilibrium between CsH_2PO_4(*sp,s*), $CsH_{2(1-x)}PO_{4-x}$(*l*), and $CsPO_3$(*s*) was observed at T = 265 °C and p_{H_2O} = 0.22 atm.

While these studies have revealed the general features of the T- p_{H_2O} phase behavior of CsH_2PO_4, several aspects remain unresolved. For example, under high humidity conditions, as reported by Taninouchi et. al. [6], different values for dehydration temperatures were obtained from thermogravimetric and conductivity measurements. Furthermore, the phase stability in the near vicinity of the triple point has not been fully clarified. Because the dehydration kinetics of CsH_2PO_4 are extremely slow (even the solid-solid dehydration remains undetectable by TG for as long as 20 hours under isothermal, isobaric conditions [4]), it is plausible that in such experiments equilibrium was not attained and is responsible for the differences, despite the fact that the results were extrapolated to zero heating rates. Kinetic effects are expected to be particularly acute for high-humidity, fixed-heating-rate experiments that traverse the liquid phase, due to sample consolidation by capillary forces generated by the presence of the liquid and the concomitant loss of surface area. In the present work we re-examine the thermodynamics and kinetics of dehydration of CsH_2PO_4 by thermal analysis. The measurements are facilitated by the use of high-surface-area silica as an additive to enhance the overall rates of the process and ensure access to thermodynamic behavior. The rehydration behavior of $CsPO_3$, which sheds light on both thermodynamic and kinetic properties of this system, is also evaluated.

3.2. Experimental details

Polycrystalline powders of CsH_2PO_4 were prepared by combining the starting reagents of Cs_2CO_3 (Alfa Aesar, 99.99%) and H_3PO_4 (ACS, 85% w/w aqueous solution) in a molar ratio of 1:2 in aqueous solution. Rapid precipitation of CsH_2PO_4 was induced by injecting the solution into methanol, yielding material with a particle size of ~ 10 μm. The CsH_2PO_4 was then combined with 20 wt % amorphous silica powder (Alfa Aesar, S.A 330-410, 325 mesh) and homogenized by mechanical agitation. For thermogravimetric (TG) experiments, the composite was used in loose powder form, whereas for differential scanning calorimetry (DSC) experiments, the powder was lightly pressed into solid compacts (~ 85% theoretical density) using a uniaxial press. Selected experiments were further performed using cesium metaphosphate, $CsPO_3$, the preparation of which is described below along with the associated measurements.

Microstructural features were observed by scanning electron microscopy (LEO 1550 VP FESEM). The accelerating voltage was 10 kV. The phase structure was determined by Rietveld refinement from X-ray powder diffraction (Philips X'Pert Pro, CuKα radiation).

Thermogravimetric (TG) analysis was carried out using an in-house-constructed system, the operation of which is discussed in detail elsewhere [4]. In brief, the sample is placed on a glass container incorporating a thermocouple junction (Type E) which, in turn, is hung from a balance (Mettler Toledo AL54) into a humidified oven that also incorporates a humidity sensor. The accessible water partial pressure and temperature ranges are, respectively, 0.02~0.75 atm and 50~400 ºC, with stabilities of ± 0.01 atm and

± 0.04 ºC, respectively. The mass resolution of the system is 0.1 mg, implying for a typical sample weight of 130 mg a relative resolution of 0.08%.

Heat flow measurements were carried out using a second, in-house-constructed system, shown schematically in Figure 3.1. The sample and reference containers are placed on an Al heat sink holder incorporating Pt resistance temperature devices (RTD). The resistances of the two RTDs are measured by a multimeter (KEITHLEY 2420) and converted to temperature values. The difference between the two is converted to heat flow, calibrated using melting enthalpy of pure Sn (7.03 kJ/mol) at its normal melting temperature 231.9 ºC. Humid N_2 gas is introduced to the chamber and humidity is observed by humidity sensor (rotronic Hygrolab). The accessible temperature and water partial pressure ranges are, respectively, 0.02~0.90 atm and 100~400 ºC, with stabilities of ± 0.01 atm and ± 0.01 ºC, respectively. The heat flow resolution of the system is 0.05 mW. For a typical heating rate of 0.5 ºC/min and a typical sample weight of 63 mg, the resolution for the thermal signature was 0.02 J/g. For both TG and DSC measurements, the actual rather than nominal p_{H_2O} is reported throughout.

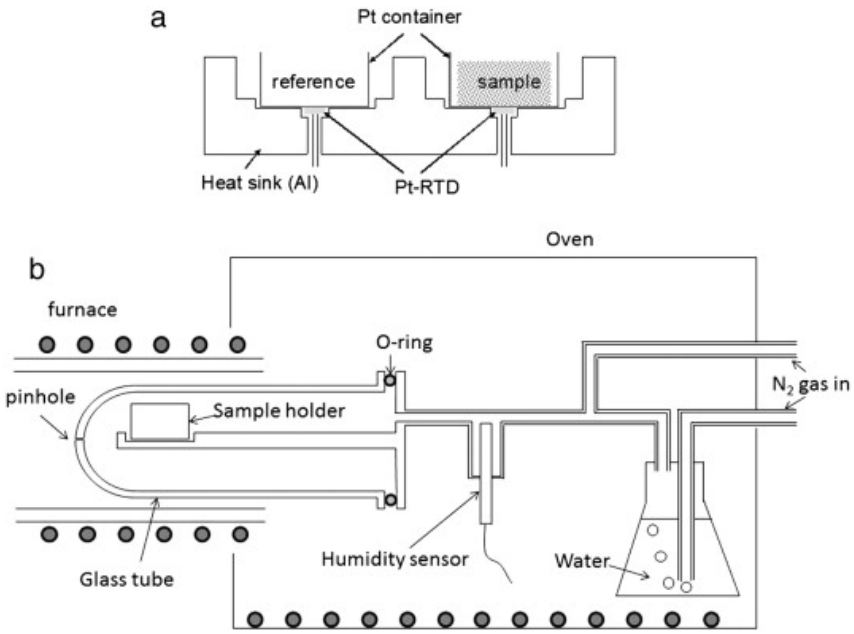

Figure 3.1. The schematic diagram of the in-house-constructed DSC chamber: (a) expanded view of sample region with integrated RTDs (resistant temperature device), and (b) overview of the entire system including the chamber, humidity generator, and humidity sensor

3.3. Results and discussion

3.3.1. Interaction of CsH_2PO_4 with SiO_2

Figure 3.2 shows XRD patterns of the products of dehydration of (a) neat CsH_2PO_4 powder and (b) CsH_2PO_4 with silica, as well as (c) the product of rehydration of the dehydrated composite of (b). While the specific method of dehydration did not impact phase behavior or the resulting morphology, we note that in this case dehydration of neat CsH_2PO_4 was achieved by exposure to p_{H_2O} = 0.02 atm at 320 ºC, whereas the composite product was obtained after several heating and cooling process under high humidity conditions (p_{H_2O} = 0.37~0.76 atm, T = 190~400 ºC). The first two patterns are in excellent agreement with one another, with the exception of an additional peak appearing in the

product of the composite that corresponds to silica. The pattern of (a) is furthermore identical to that obtained previously by Taninouchi et al. [4] for the complete dehydration of CsH_2PO_4. In light of the observed weight loss, this product is identified as $CsPO_3$, despite differences from the ICDD reference pattern attributed to this material [7,8]. Upon rehydration, the phosphate phase in the composite reverted to CsH_2PO_4, with lattice constants, as determined by Rietveld refinement, Table 3.1, matching the literature values of CsH_2PO_4 [9]. These results indicate that CsH_2PO_4 does not react with silica during either dehydration or rehydration.

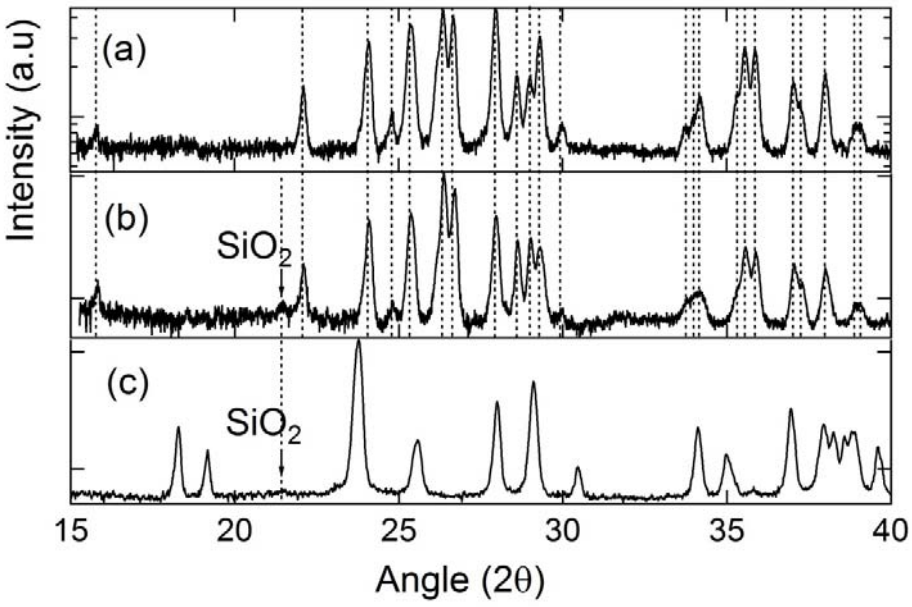

Figure 3.2. XRD profiles of (a) the dehydration product of neat CsH_2PO_4 powder, (b) the dehydration product of composite CsH_2PO_4 and silica, and (c) the rehydration product of (b). Dotted lines are guides to the eye.

Table 3.1. Lattice constants of CsH_2PO_4 as measured post thermal cycling in the presence of SiO_2, compared to standard literature values

Material	a (Å)	b (Å)	c (Å)	β (°)
Rehydrated CsH_2PO_4 + silica	7.9032(6)	6.3889(4)	4.8763(3)	107.650(4)
CsH_2PO_4 [10]	7.90065(8)	6.36890(9)	4.87254(12)	107.742

Scanning electron microscopy images of the dehydration products are shown in Figure 3.3, where (a) corresponds to a composite sample, and (b) to a sample of CsH_2PO_4 alone. It is immediately apparent that the neat phosphate forms large particles of $CsPO_3$ that are several tens of microns in diameter. In contrast, the composite retains submicron feature sizes, with typical grains of $CsPO_3$ that are ~ 200 nm in diameter and reasonably well separated in the porous, composite structure.

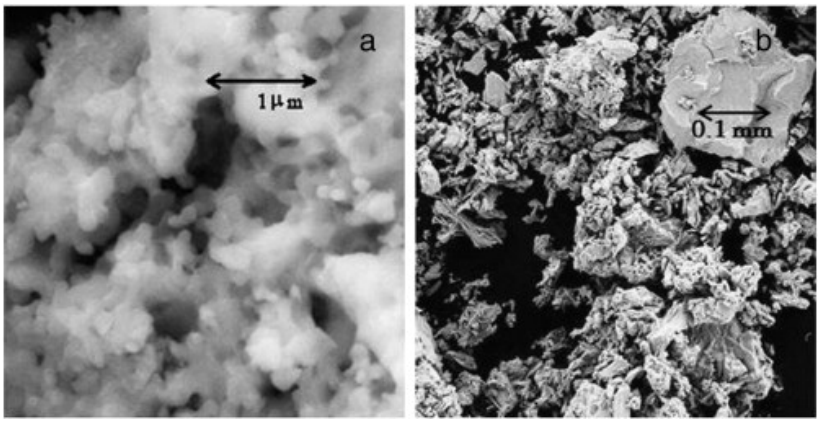

Figure 3.3. Scanning electron microscopy images obtained in secondary electron mode of (a) the dehydration product of composite CsH_2PO_4 and silica and (b) of neat $CsPO_3$

3.3.2. General dehydration characteristics and data analysis methodology

Typical isobaric gravimetric and differential calorimetry curves for CsH_2PO_4 in both the presence and absence of SiO_2 are presented in Figures 3.4 and 3.5, where the former corresponds to humidity conditions falling below the triple-point and the latter to conditions passing above it. The selected data demonstrate the general characteristics of

the dehydration behavior under different heating rates and different water partial pressures, and the role of SiO_2. The most significant features of the data collected at low humidification (p_{H_2O} ~ 0.25 atm) are as follows. At sufficiently low heating rates, e.g., 0.01 and 0.1 K/min [Figures 3.4(a) and (b)], the composite samples undergo a single-step dehydration, with an onset designated T_d. At higher heating rates, e.g., 0.5 K/min, the behavior of the composite changes, undergoing a two-step dehydration reaction that extends over a broader temperature window. The neat CsH_2PO_4 displays extremely slow dehydration kinetics and even at a low heating rate of 0.1 K/min, the data suggest a complex, multistep process that reaches completion only upon exposure to high temperature for prolonged times. Irrespective of the duration and pathway of dehydration or the presence or absence of SiO_2, however, the final product obtained at the completion of the reactions by 360 ºC corresponds, by weight, to $CsPO_3$. Thus, the introduction of SiO_2 has the effect of greatly enhancing kinetics without modifying the thermodynamic outcome of the dehydration reaction, consistent with the diffraction data analysis and microstructural evaluation.

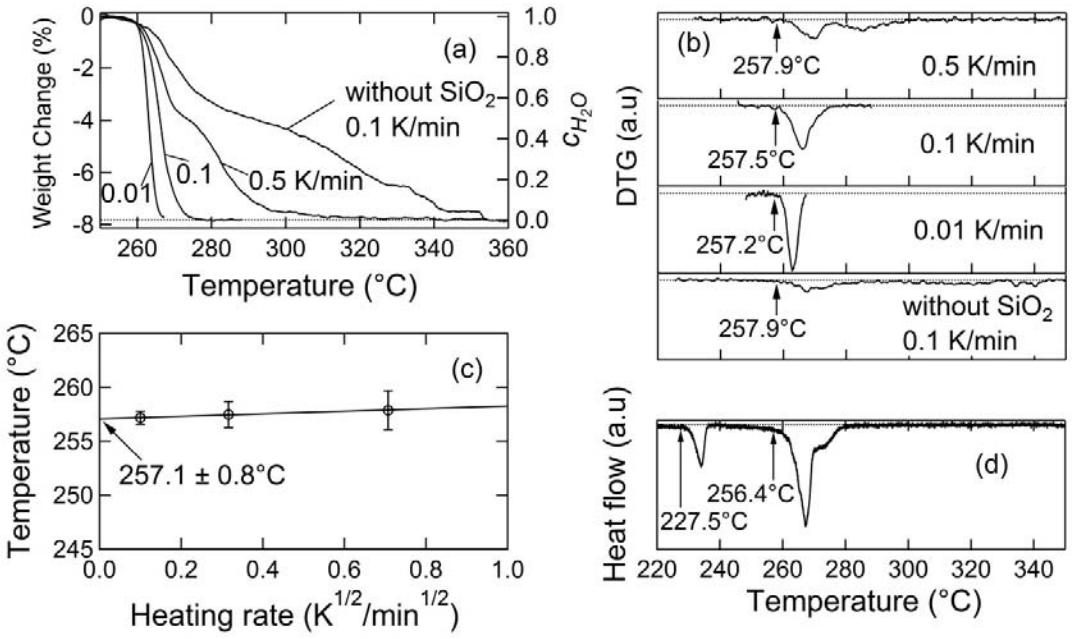

Figure 3.4. Typical dehydration behavior of CsH_2PO_4 below the triple point: (a) thermogravimetry (TG) profile of composite and neat CsH_2PO_4 at p_{H2O} = 0.26 atm at the heating rates indicated. (b) Differential weight loss curves corresponding to the profiles in part (a). (c) Dependence of observed dehydration temperature in composite samples on heating rate. (d) Differential scanning calorimetry (DSC) curve at p_{H2O} = 0.27 atm and a heating rate of 0.5 K/min.

The data in Figure 3.4 further reveal that the onset of the dehydration reaction at low humidity is largely independent of heating rate and of the presence or absence of silica. For the example of p_{H_2O} = 0.26 atm indicated in the TG data, the onset temperatures vary by just 0.7 ºC, from 257.2 to 257.9 ºC. The thermal significance of this dehydration is clearly captured in the DSC data, Figure 3.4(d), with a T_d that matches the TG results. The DSC curve (collected from a composite sample at a heating rate of 0.5 K/min) further displays an anomaly with an onset at 228 ºC due to the polymorphic transition to the cubic phase. The data unequivocally demonstrate (as has been shown previously in the literature) that this transition is not connected to dehydration as weight loss under these humidification conditions does not occur until much higher temperatures. The

enthalpy recorded is 11.7 ± 1.1 kJ/mol, consistent with the values summarized in reference [3] and validating the calibration of the heat signal. The TG data for the same sample type and experimental conditions, shown in differential form in Figure 3.4(b), indicate that the second dehydration step is relatively well defined, with an onset of ~ 280 ºC, but that the signal is barely detectable by DSC. The composite sample is considered to be out of equilibrium at a heating rate of 0.5 K/min and thus the nature of this second dehydration was not further investigated.

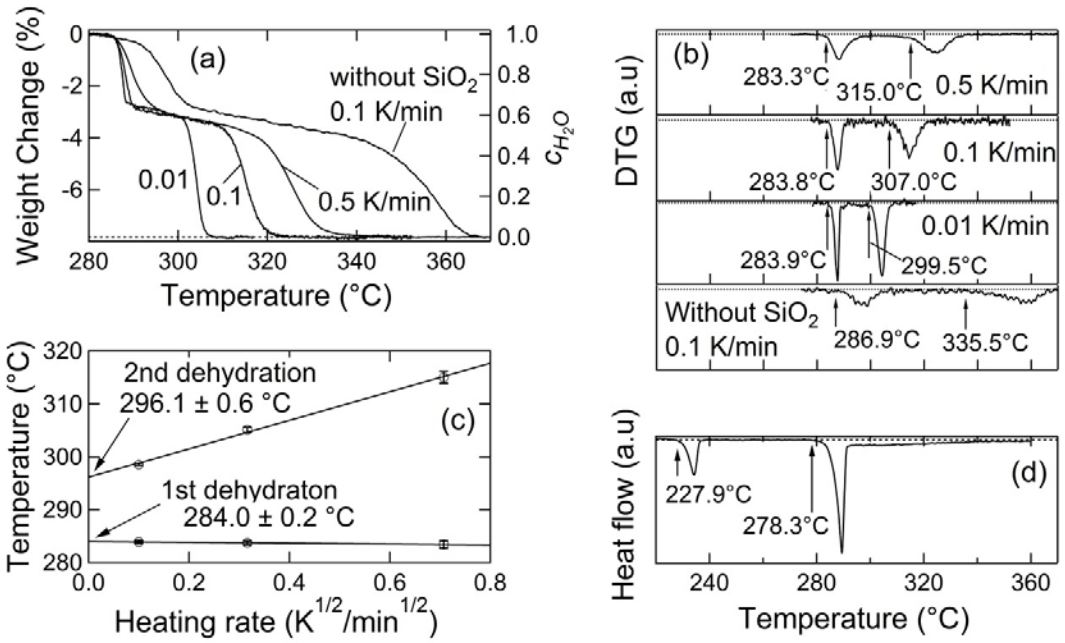

Figure 3.5. Typical dehydration behavior of CsH_2PO_4 above the triple point: (a) Thermogravimetry (TG) profile of composite and neat CsH_2PO_4 at p_{H2O} = 0.64 atm at the heating rates indicated. (b) Differential weight loss curves corresponding to the profiles in part (a). (c) Dependence of observed dehydration temperature in composite samples on heating rate. (d) Differential scanning calorimetry (DSC) curve at p_{H2O} = 0.60 atm and a heating rate of 0.5 K/min

The dehydration behavior of CsH_2PO_4 under high humidification conditions, Figure 3.5, shows both differences and similarities to that under low humidification. The most significant difference is that for both types of samples and all heating rates explored,

the dehydration process occurs in two distinct and well-resolved steps. An initial sharp weight change is followed by a slight, monotonic weight loss (a sloping plateau in the TG plot), and then a second, sharp weight change. Thus, as suggested by Taninouchi [4], an intermediate phase of variable H_2O content is stable at high p_{H_2O} and intermediate temperatures. The magnitudes of the weight changes reveal that the intermediate phase has a composition $CsH_{2(1-x)}PO_{4-x}$ with an initial, low-temperature x value of 0.33 and a final, high-temperature value of 0.4 ~ 0.5, depending on heating rate. All samples that displayed this two-step dehydration process emerged from the experimental TG apparatus as densified, almost glassy compacts, whereas those that displayed only a single-step process remained in the form of loose powders, suggesting, in agreement with the observations of Taninouchi, that the intermediate phase is a liquid.

Close examination of the data in Figures 3.5(a) and (b) reveals that, amongst the composite samples, the onset of the first dehydration event, T_{d1}, is independent of heating rate for rates between 0.01 and 0.5 K/min (occurring in this case at 284.0 ± 0.2 ºC). As in the low humidity experiments, the absence of SiO_2 greatly decelerates the overall kinetics. The effect is so significant here, however, that the onset of this first dehydration event is retarded by 5 to 6 ºC. Turning to the second dehydration step, the data reveal that not only is this process sensitive to the nature of the sample, it is highly sensitive to heating rate, unlike the first dehydration step. Specifically, the apparent onset temperature, T_{d2}, shifts to increasingly higher values with increasing heating rate, $dT/dt = R$. Such behavior, also observed by Taninouchi [6], suggests that the dehydration of $CsH_{2(1-x)}PO_{4-x}(l)$ to form $CsPO_3(s)$ is a substantially slower reaction than the dehydration of CsH_2PO_4. To account for the thermal/kinetic lag in the system and to extract the thermodynamic value of the

onset of dehydration, the observed T_{d2} values were plotted against $R^{½}$, Figure 3.5(c), and extrapolated to $R = 0$. The DSC data, Figure 3.5(d), reveal clear thermal events associated with the superprotonic transition (with an onset value again of 228 ºC), and the first dehydration event, with T_{d1} = 278.3 ºC, at a temperature generally consistent with the TG data. Reminiscent of the low humidity data, however, the second dehydration event is barely detectable in the DSC profile. Such behavior is consistent with a kinetically constrained reaction for which heat release is too gradual to be recorded as a thermal anomaly.

With the overall dehydration characteristics understood, the behavior of CsH_2PO_4 over a wide range of water partial pressures was explored. From the discussion presented above, the dehydration reactions of interest are

(A) $$CsH_2PO_4(s,sp) \leftrightarrow CsPO_3(s) + H_2O(g) \quad (1)$$

(B) $$CsH_2PO_4(s,sp) \leftrightarrow CsH_{2(1-x_i)}PO_{4-x_i}(l) + x_iH_2O(g) \quad (2)$$

(C) $$CsH_{2(1-x_f)}PO_{4-x_f}(l) \leftrightarrow CsPO_3(s) + x_fH_2O(g) \quad (3)$$

where x_i and x_f reflect the respective stoichiometries of the intermediate liquid phase when it is first formed and then finally consumed during heating. The TG experiments can detect all three of these dehydration steps and were performed using composite samples at water partial pressures between 0.26 and 0.76 atm and a fixed heating rate of 0.01 K/min. At this slow heating rate the onset temperatures of Reactions (A) and (B) are accurately obtained from TG data, whereas the overestimation of T_{d2} (Reaction C) is less than 3 ºC. The DSC measurements can detect Reactions (A) and (B) as well as the superprotonic transition, the onset behavior of which is largely independent of heating

rate. Measurements were performed at 0.5 K/min over the water partial pressures range of 0.06 atm to 0.90 atm. To ensure accurate positioning of the triple point, measurements in the p_{H_2O} range of 0.29 to 0.42 atm were repeated multiple times (and results confirmed to be reproducible). At low humidities, at which dehydration would be expected to occur at the lowest temperatures, additional isothermal gravimetric measurements were carried out using partially dehydrated samples (composed of CsH_2PO_4, $CsPO_3$, and SiO_2) at conditions in the near vicinity of the low temperature phase boundary of Reaction (A). It was anticipated that the presence of both phosphate phases would overcome any nucleation barrier and hence aid the transformation kinetics.

For each individual, constant ramp-rate measurement, the decomposition temperature was defined as the onset of the thermal event, as implied through-out the preceding discussion. In the case of the DSC profiles, a numerical procedure described in detail elsewhere [10] was employed to precisely establish this onset. In the case of the TG profiles, the onset was determined from the dTG plots by evaluating the intersection between the baseline and the tangent of the dTG peak. Overall, it is to be emphasized that the presence of SiO_2 in composite samples here is believed to allow rapid access to thermodynamic conditions, and for this reason is an advance over previous studies of dehydration behavior.

3.3.3. Thermodynamics of dehydration

The TG and DSC data obtained from composite samples over the wide range of conditions explored are presented in Figures 3.6 and 3.7, respectively. In agreement with the discussion above, at low humidities ($p_{H_2O} < 0.5$ atm) a single-step dehydration process occurs, whereas at high humidities a two-step process is evident (Figure 3.6). In addition,

the dehydration generally shifts to higher temperatures with increasing p_{H_2O}, as evidenced in both datasets. At p_{H_2O} = 0.10 and 0.083 atm the DSC peak due to dehydration overlaps with that due to the superprotonic transition, and the dehydration temperature for these conditions were not evaluated further. Moreover, at p_{H_2O} = 0.083 and 0.059 atm, an additional thermal event at a temperature beyond the initial dehydration is evident in each profile. This is believed to be due to the crystallization of amorphous $CsPO_3$ and is not considered further.

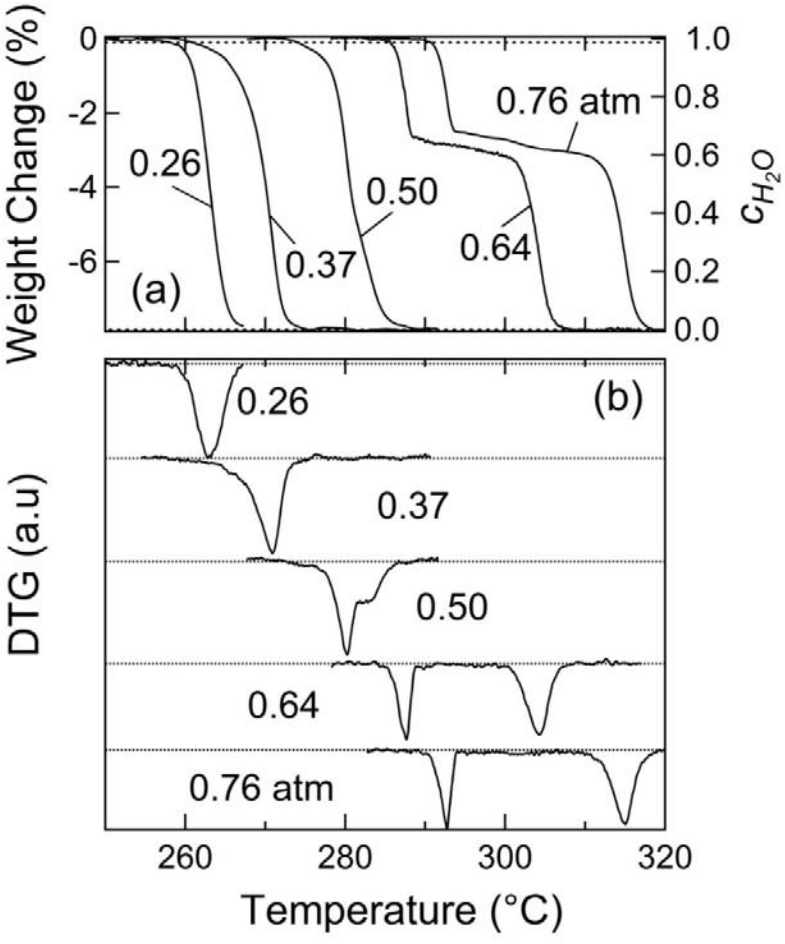

Figure 3.6. Weight change behavior of CsH_2PO_4 (in composite form with SiO_2) at a heating rate of 0.01 K/min and under the water partial pressures indicated: (a) Thermogravimetric data; and (b) differential TG data

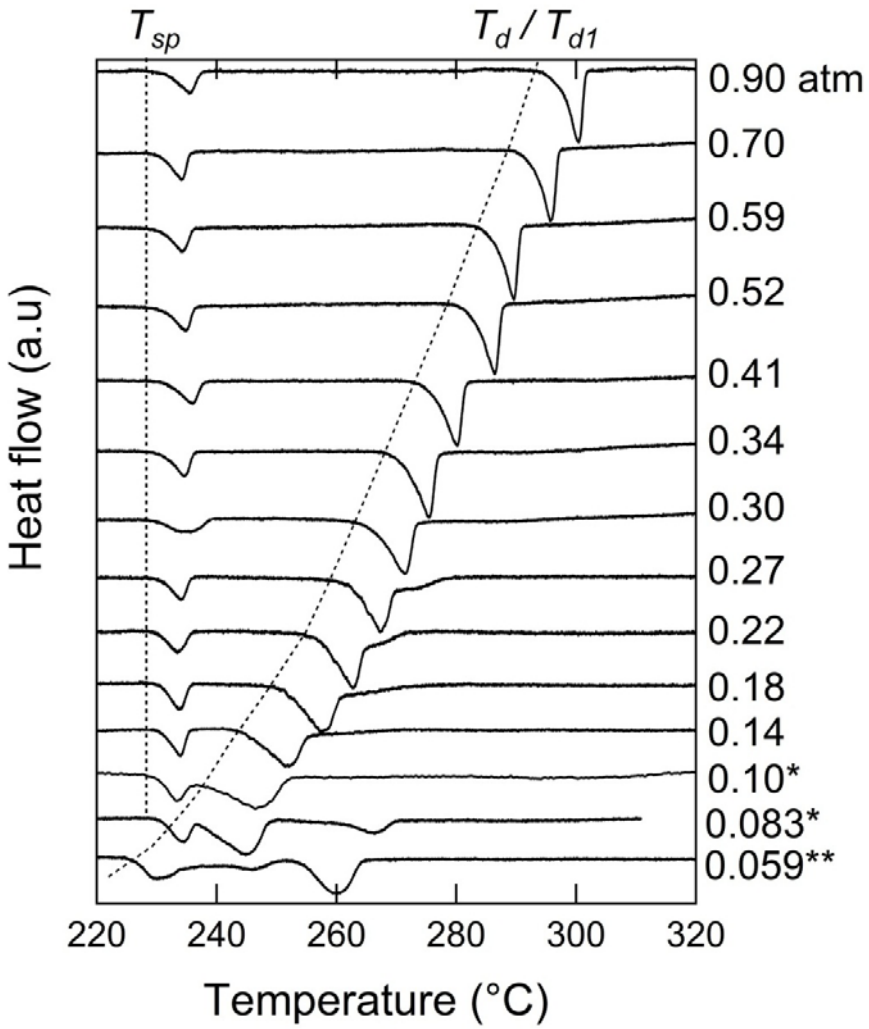

Figure 3.7. Thermal behavior of CsH_2PO_4 (in composite form with SiO_2) at a heating rate of 0.5 K/min and under the water partial pressures indicated. * indicates curves for which the data were not used to evaluate phase behavior due to the poor resolution of peaks.

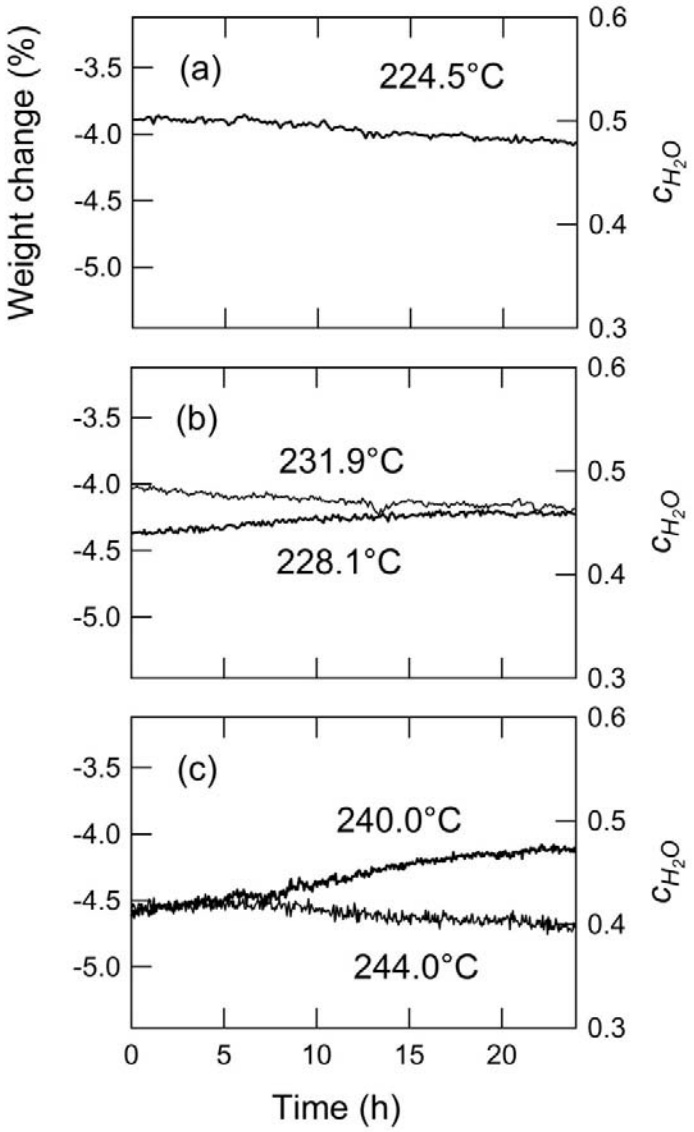

Figure 3.8. Isothermal weight change behavior of composite samples of $CsPO_3$, CsH_2PO_4, and SiO_2 at (a)p_{H2O} = 0.09 atm. (b) p_{H2O} = 0.13 atm, and (c) p_{H2O} = 0.18 atm.

The isothermal weight change results under low p_{H_2O} conditions, 0.09, 0.13 and 0.18 atm, are presented in Figure 3.8. The results reveal that at p_{H_2O} = 0.13 atm the phase boundary occurs between 228.1 and 231.9 °C, whereas at p_{H_2O} = 0.18 it shifts to a temperature between 240 and 244 °C. In contrast, the raw DSC curves, obtained under finite heating rates, suggest phase boundary temperatures of 242 and 250 °C, respectively,

for these two atmosphere conditions (Figure 3.7). From the p_{H_2O} = 0.09 atm data, it is evident that the phase boundary lies somewhere below 225 °C, a temperature significantly lower than what has been previously suggested in the literature. The results thus further demonstrate that extremely long times are required to observe the equilibrium weight change behavior. While the change in weight is extremely gradual in these datasets (0.0202 to 0.0234 mg/hr), the change is statistically greater than the instrument drift and hence the results indeed reveal the location of the phase boundary.

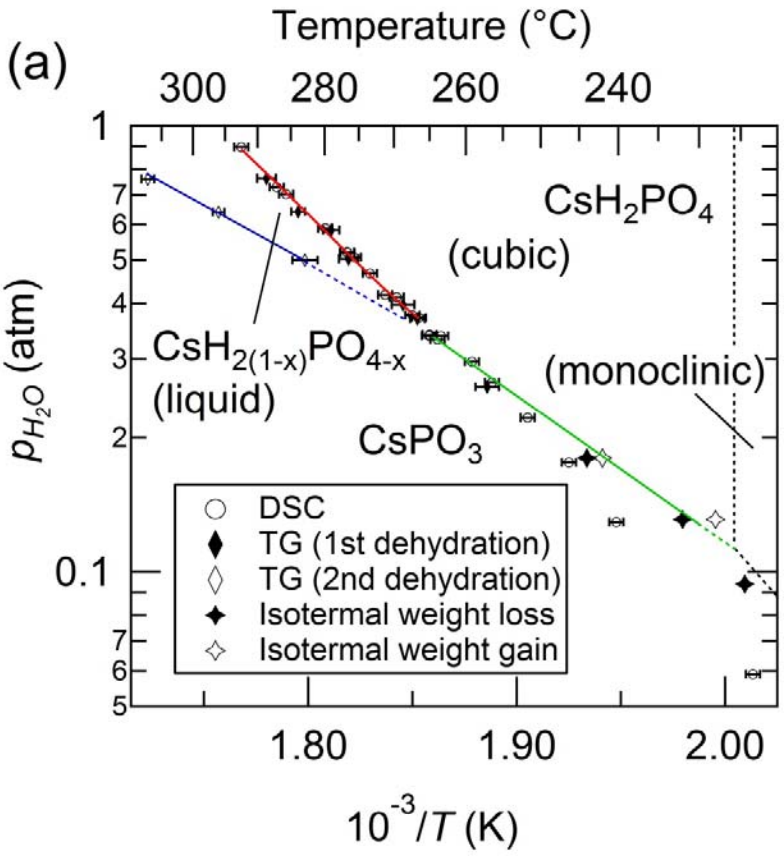

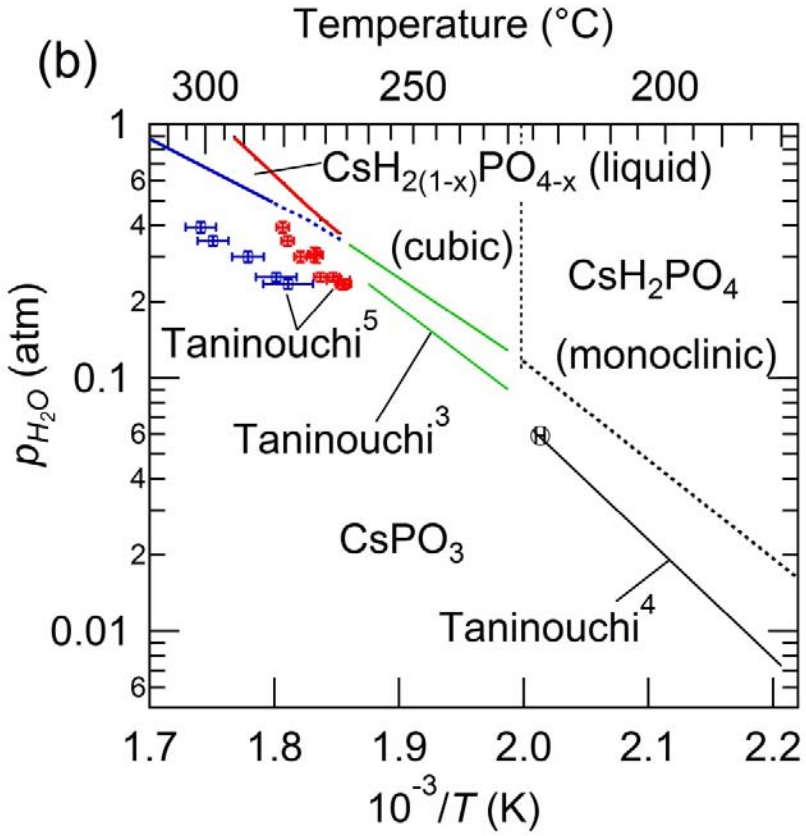

Figure 3.9. The T–p_{H2O} phase diagram of CsH_2PO_4 (a) in the vicinity of the triple point as determined in this work and (b) over a broader range of conditions, and shown in comparison with previous determinations of the phase boundaries. Red line (between the liquid and cubic regions) corresponds to reaction B, blue (between the liquid and $CsPO_3$ regions) to reaction C, green (between cubic and $CsPO_3$ regions) to reaction A above the superprotonic transition, and black (between monoclinic and $CsPO_3$ regions) to reaction A* below the transition.

From the data of Figures 3.6-3.8, the dehydration temperature of CsH_2PO_4 as a function of p_{H_2O} was determined and the results were compiled to yield the phase diagram presented in Arrhenius form in Figure 3.9. Part (a) shows just the results of the present work and part (b) a comparison with literature data over the water partial pressure range p_{H_2O} = 0.05 ~ 0.90 atm and temperature range 215 to 320 °C. The general features of the phase diagram constructed here are in agreement with those previously reported in

the literature. Solid CsH_2PO_4 exists at the low-temperature, high-humidity region of the phase diagram, solid $CsPO_3$ at the high-temperature, low-humidity region, and liquid $CsH_{2(1-x)}PO_{4-x}$ exists in a narrow range of conditions at high temperature and high humidity. The results differ from the earlier studies in that the phase boundaries are shifted to higher p_{H_2O}, or equivalently, lower temperatures. That is, for a given temperature, higher levels of humidification are required to stabilize CsH_2PO_4 than had been previously reported [4,6]. We interpret the difference in results as arising, as suspected at the outset, from kinetic stabilization of CsH_2PO_4, behavior which is largely eliminated in the presence of SiO_2.

The hydration/dehydration characteristics, shown for example for a temperature ramp rate of 0.01 K/min and a water vapor pressure of 0.76 atm, reveal aspects of the thermodynamic stability of the phases involved, Figure 3.10. The onset of the first dehydration event on heating occurs at $T_{d1} = 288.6 \pm 0.5$ °C, confirming that CsH_2PO_4 is thermodynamically unstable above this temperature for the given p_{H_2O}. The onset of rehydration on cooling is found to occur at a temperature, $T_{h1} \sim 294$ °C, that is higher than T_{d1}. Because CsH_2PO_4 is unstable above T_{d1}, this result implies that the weight recovery that occurs between T_{h1} and T_{d1} is due to the transformation of $CsPO_3$ to a phase other than CsH_2PO_4, presumably $CsH_{2(1-x)}PO_{4-x}(l)$. Such behavior is strong evidence for the thermodynamic stability of the liquid dehydrate. At temperatures below T_{d1}, complete weight recovery eventually occurs. This, in combination with the diffraction data which showed only CsH_2PO_4 and SiO_2 to be present in the composite after complete rehydration, confirms the stability of CsH_2PO_4 under high-humidity conditions.

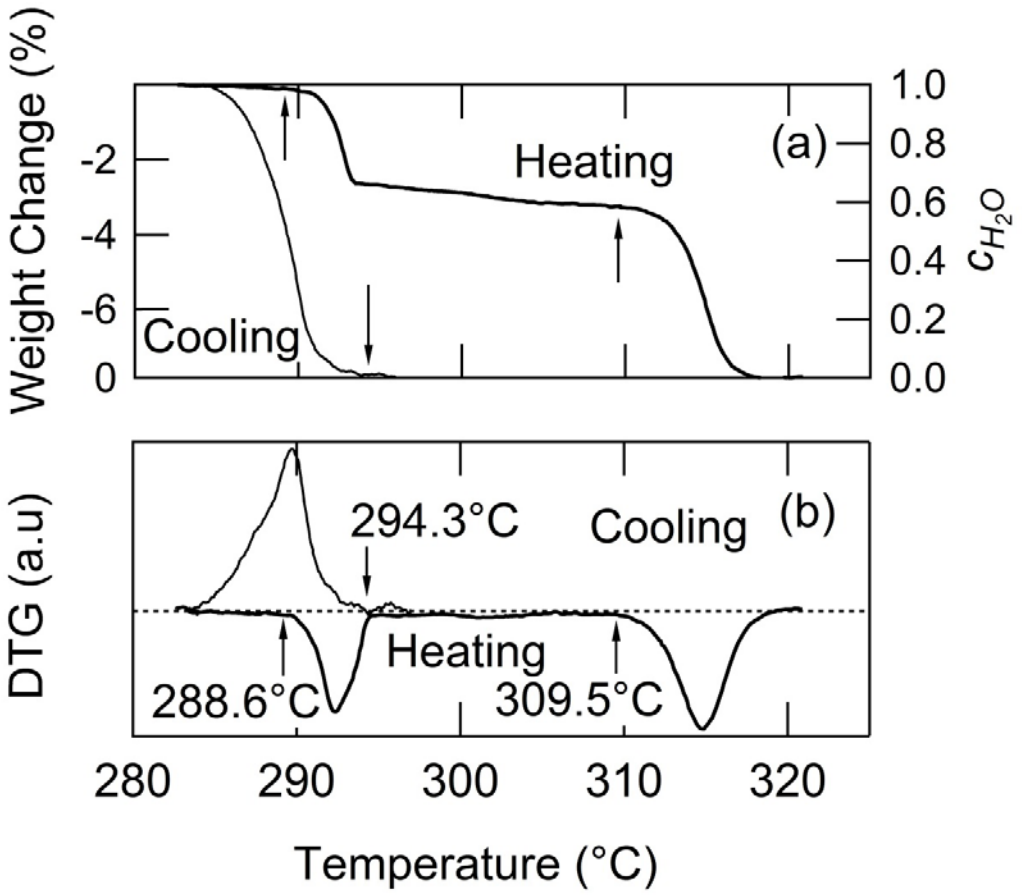

Figure 3.10. Comparison of dehydration and rehydration behavior of CsH_2PO_4 and $CsPO_3$ respectively, (in composite form with SiO_2) at a temperature ramp rate of 0.01 K/min and under p_{H2O}= 0 .76 atm. (a) Thermogravimetric and (b) differential TG curves. Temperatures corresponding to onset of phase change are indicated.

Our revised phase diagram reveals that the triple point (at which $CsH_2PO_4(s)$, $CsPO_3(s)$, and $CsH_{2(1-x)}PO_{4-x}(l)$ are in simultaneous equilibrium) occurs is at p_{H_2O} = 0.35 ± 0.2 atm and T = 267.5 ± 1.0 ºC, again, reflecting a shift to a somewhat higher p_{H_2O} as compared to the previous work. This point corresponds to the position at which a change in slope of the boundary defining the stability limit of CsH_2PO_4 was observed by DSC measurements. In principle, the TG data should reveal a two-step dehydration process at all conditions in the triple-point, however, such behavior could not be clearly resolved at

p_{H_2O} = 0.37 atm (Figure 3.6). This is attributed to the extremely narrow stability region of the liquid at this humidification level and to the slow dehydration kinetics, and is not considered inconsistent with the proposed phase behavior. At all higher humidification levels, two-step dehydration is clearly observed. At low humidification levels, a strong difference between the isothermal (TG) and finite heating rate (DSC) results are clearly evident. The phase boundary points determined from the isothermal measurements fall on the line extrapolated from the high temperature boundary, supporting the conclusion that the isothermal data reflect the true equilibrium.

All three phase boundaries determined in this study are linear in the Arrhenius representation. Linear best fits to these boundaries yield the following expressions:

Reaction (A) $$\log p_{H_2O} = 5.66 \pm 0.17 - (3.29 \pm 0.09)\frac{1000}{T} \quad (5)$$

Reaction (B) $$\log p_{H_2O} = 7.90 \pm 0.13 - (4.50 \pm 0.07)\frac{1000}{T} \quad (6)$$

Reaction (C) $$\log p_{H_2O} = 4.06 \pm 0.19 - (2.42 \pm 0.11)\frac{1000}{T} \quad (7)$$

.

Under the assumption of unit thermodynamic activity of the condensed phases and ideal gas behavior of vapor phase H_2O, the expressions above provide a direct measure of the standard Gibbs free energy of the dehydration reactions of interest, $\Delta_{dehy}G^{\circ}$. Specifically, these assumptions imply the following relationships

$$\ln p_{H_2O} = -\frac{\Delta_{dehy}G^{\circ}_{(A)}(T)}{RT} \quad (8)$$

$$\ln p_{H_2O} = -\frac{\Delta_{dehy}G^{\circ}_{(B)}(T)}{x_i RT} \quad (9)$$

$$\ln p_{\mathrm{H_2O}} = -\frac{\Delta_{\mathrm{dehy}} G^{\circ}_{(\mathrm{C})}(T)}{(1-x_f)\mathrm{R}T} \tag{10}$$

where the stoichiometric coefficient for H_2O in reactions B and C is accounted for. Because the dehydrated liquid, $CsH_{2(1-x)}PO_{4-x}$, is not a stoichiometric compound, with x varying over the range of approximately 0.30 to 0.60 for the range of conditions examined, the assumption here of unit activity in this phase introduces a finite but small error. The standard Gibbs free energy of dehydration, in turn, can be expressed in terms of the standard enthalpy, $\Delta_{\mathrm{dehy}}H^{\circ}$, and entropy, $\Delta_{\mathrm{dehy}}S^{\circ}$, of dehydration according to

$$\Delta_{\mathrm{dehy}}G^{\circ} = \Delta_{\mathrm{dehy}}H^{\circ} - T\Delta_{\mathrm{dehy}}S^{\circ}. \tag{11}$$

Using the best-fit linear values reported in Eqs. (5)–(7), and taking the averaged x values, $x_i = 0.31 \pm 0.03$ and $x_f = 0.40 \pm 0.02$, the standard enthalpy and entropy of dehydration for reactions (A)–(C) were computed. The values are summarized in Table 3.2, along with relevant prior literature estimates of these parameters. The standard enthalpy of reaction (B) was further evaluated directly from the intensity of the DSC signal, and is also provided in the table. The direct-calorimetric and the phase boundary based results are in good agreement with one another. Data for an additional reaction, the low temperature dehydration of monoclinic CsH_2PO_4 to solid $CsPO_3$, referred to as A*, are also included in the table. Because reaction A* can be considered a two-step process in which CsH_2PO_4 first transforms to the superprotonic phase then undergoes dehydration, the enthalpy and entropy values can be computed according to $\Delta_{\mathrm{dehy}}H^{\circ}_{(\mathrm{A}^*)} = \Delta_{\mathrm{dehy}}H^{\circ}_{(\mathrm{A})} + \Delta H_{\mathrm{sp}}$ and $\Delta_{\mathrm{dehy}}S^{\circ}_{(\mathrm{A}^*)} = \Delta_{\mathrm{dehy}}S^{\circ}_{(\mathrm{A})} + \Delta S_{\mathrm{sp}}$. The calculation was carried out using the enthalpy and entropy values of the superprotonic transition determined here by calorimetry (ΔH_{sp} = 11.7 ± 1.1

kJ/mol, ΔS_{sp} 23.4 ± 2.2 =, T_{sp} = 228°C) in combination with the thermodynamic characteristics of reaction A determined as described above. Overall, the slow dehydration and rehydration kinetics below 228 °C precluded a direct evaluation of this phase boundary.

Table 3.2. Summary of thermodynamic parameters for the dehydration of CsH_2PO_4. See text for definition of reactions (A)–(C). Unless otherwise stated, in the work the parameters were determined from an evaluation of the slopes of the phase boundaries in the Arrhenius representation of the phase diagram.

Reaction	$\Delta_{dehy}H^\circ$ (kJ/mol)	$\Delta_{dehy}S^\circ$ (J/mol·K)	T (°C)	p_{H_2O} (atm)	source
A	63.1 ± 1.7	108.3 ± 3.1	230 ~ 267	0.13 ~0.34	This work
A	69.5 ± 8.0	117 ± 16	230 ~ 260	0.09~0.24	[3]
A*	74.8 ± 2.8	131.7 ± 5.3			Calculated
A*	81.5	137.65		vacuum	[10]
A*	84.6 ± 10.7	146 ± 23	190 ~ 220	0.0085~0.035	[4]
B	30.2 ± 1.1	53.1 ± 1.9	268 ~ 292	0.37~0.89	This work
B	30.7 ± 3.0			0.59	This work (DSC)
C	27.8 ± 1.8	46.6 ± 3.2	282 ~307	0.37~0.89	This work

*CsH_2PO_4(*s*, *monoclinic*) → $CsPO_3$(*s*) + H_2O(*g*)

As with the phase diagram itself, the tabulated summary reveals qualitative, but not quantitative, agreement with earlier results. An important aspect concerns the phase behavior in the vicinity of the triple point. Thermodynamic principles dictate that not only should the phase boundaries meet at a single point, but also that the slope of the lower temperature boundary, Reaction A, be intermediate to those of the two higher temperature boundaries, Reactions B and C. Such behavior is indeed apparent in Figure 3.9 and in the values of the reaction enthalpies listed in Table 3.2, after accounting for the respective stoichiometric coefficients in Equations. (9) and (1). The internal consistency

of the present set of thermodynamic parameters can be further evaluated as follows. For a liquid phase of fixed stoichiometry Reaction A is the chemical sum of Reactions B and C, and hence the thermodynamic quantities $\Delta_{\text{dehy}}H^{\circ}$ and $\Delta_{\text{dehy}}S^{\circ}$ must sum in an analogous sense, i.e., $\Delta_{\text{dehy}}H^{\circ}_{(\text{A})} = \Delta_{\text{dehy}}H^{\circ}_{(\text{B})} + \Delta H^{\circ}_{(\text{C})}$. The enthalpy and entropy sums, 58.0 ± 2.9 kJ/mol and 99.7± 5.1 J/mol K, respectively, are somewhat lower that the measured values for reaction A, a difference reasonably attributed to the variable stoichiometry of the liquid phase. Overall, the relatively small differences between the present set of values and those reported in the earlier literature are taken to result from differences in experimental conditions that either prevented access to equilibrium conditions at low temperatures [5] or led to a convolution of the two-step dehydration behavior at high temperatures [11].

3.3.4. Kinetics of rehydration

As with dehydration of CsH_2PO_4, the rehydration kinetics of $CsPO_3$ were found to be highly dependent on the presence or absence of SiO_2, as well as general sample morphology. The isothermal (T = 238 ºC), fixed-humidity (p_{H_2O} = 0.51 atm), weight gain behavior of three different types of samples are shown in Figure 3.11: (a) a composite of $CsPO_3$ and SiO_2 of the type shown in Figure 3.3(a) obtained by annealing a composite of CsH_2PO_4 and SiO_2 at T = 400 ºC and p_{H_2O} = 0.51 atm; (b) a loose powder of $CsPO_3$ of the type shown in Figure 3.3(b) obtained by annealing CsH_2PO_4 at 320 ºC and p_{H_2O} = 0.02 atm; and (c) a dense, semi-transparent compact of $CsPO_3$ obtained by annealing CsH_2PO_4 at T = 400 ºC and p_{H_2O} = 0.76 atm. Consistent with the phase behavior of Figure 3.8, the samples undergo weight gain that plateaus only when the H_2O uptake corresponds to complete conversion of $CsPO_3$ to CsH_2PO_4. More significantly, the hydration of the

composite sample is clearly much more rapid than that of the neat $CsPO_3$ powder, which, in turn, is more rapid than that of the dense $CsPO_3$ pellet. Specifically, the time for 50% rehydration is about 100 times shorter for the composite than it is for the neat $CsPO_3$ powder, which, in turn, is about 10 times shorter than it is for the dense $CsPO_3$ pellet. The small $CsPO_3$ particle sizes in the composite present the shortest H_2O diffusion distances and the highest specific surface area, both of which facilitate rapid kinetics. In the case of dense $CsPO_3$, weight gain remains virtually undetectable for approximately 3 hr, emphasizing the significance of accelerating reaction kinetics in order to accurately capture thermodynamic and even valuable transient behavior. Accordingly, all studies of rehydration characteristics were carried out using composite samples of $CsPO_3$ and SiO_2.

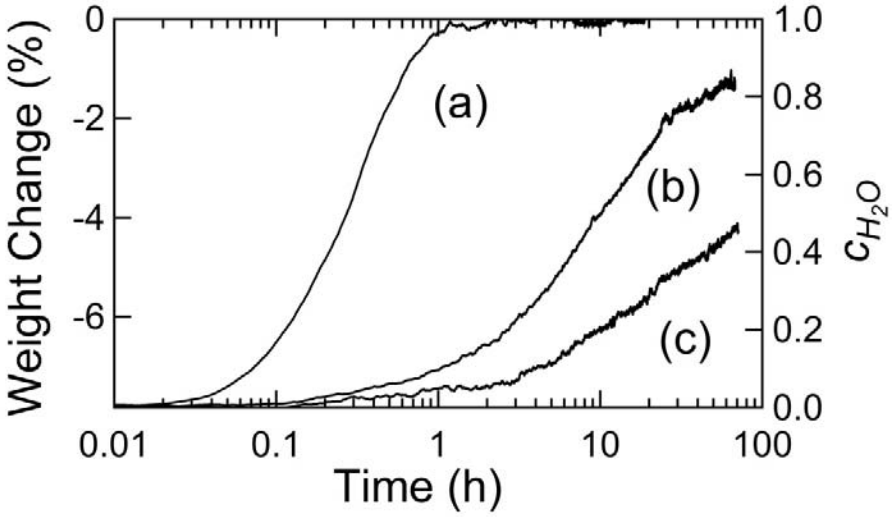

Figure 3.11. Isothermal hydration behavior of $CsPO_3$ in various forms at T = 238 °C under p_{H_2O} = 0.51 atm: (a) fine-grained material, obtained by dehydration of SiO_2 and CsH_2PO_4 composites; (b) neat, micro-particulate (1–100 μm) $CsPO_3$powder; and (c) large grained $CsPO_3$ with 1–2mm grain

All hydration experiments were performed using composite samples dehydrated by annealing at T = 330 °C and p_{H_2O} = 0.64, conditions corresponding to the stability

field of $CsPO_3$. A first series of rehydration measurements were carried out at several temperatures within the range 205 to 282 ºC. After complete dehydration was achieved, the system was rapidly cooled to the measurement temperature. The thermal lag of the system is estimated at 5 min, much shorter than the many hours required to attain full rehydration. A second series of measurements were carried out a fixed temperature of 243 ºC and several different water partial pressures. In this case, the p_{H_2O} was set to the desired value while the sample was at 330 ºC. From this condition the sample was again quenched to the measurement temperature and the weight gain monitored as a function of time. For each series, a single sample was cycled through the relevant conditions.

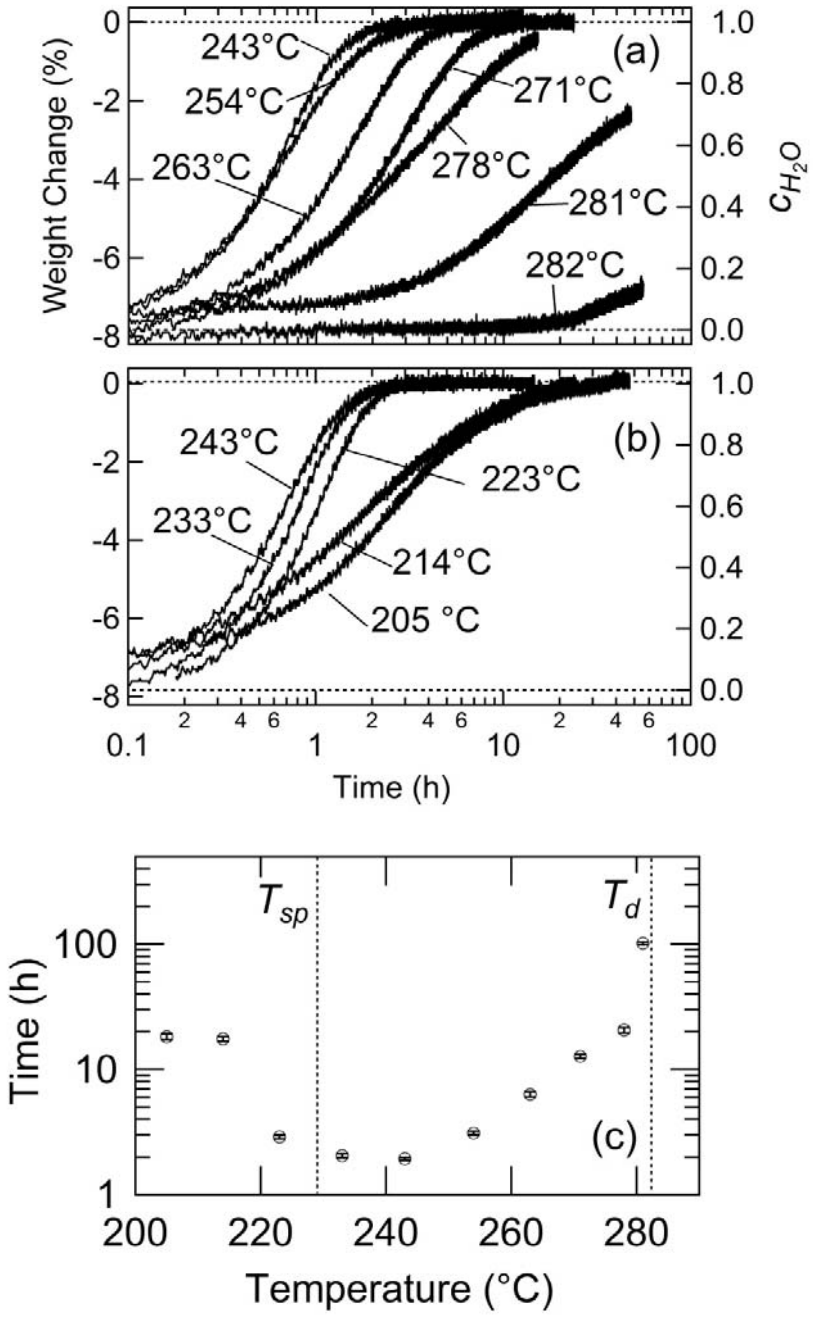

Figure 3.12. Isothermal hydration behavior of composite $CsPO_3$(s) and SiO_2 at several different temperatures underp_{H2O} = 0.63 atm: (a) time dependent behavior at high temperature; (b) time-dependent behavior at low temperature; and (c) hydration rate, defined as time to 99% of reaction completion.

The isothermal rehydration behavior under fixed p_{H_2O} = 0.64 atm shows a strong dependence on temperature, Figure 3.12. The curves are similar in that each displays a monotonic increase in weight without any plateau, indicative of a single-step transformation of $CsPO_3$(*s*) to CsH_2PO_4(*s*), despite the fact that the quench from 330 ºC requires the system to traverse the stability field of (*l*). The differences are reflected in the dramatically differing time constants. At the highest temperature, 282 ºC, detectable weight gain occurs only after 20 hr under the humid conditions. Its eventual occurrence confirms the location of the phase boundary between CsH_2PO_4(*s*) and $CsH_{2(1-x)}PO_{4-x}$(*l*). As the temperature of the isothermal hold is decreased, the rate first increases, plateaus in the mid-temperature range, and then increases again at the lowest temperatures, although not becoming as sluggish as the high temperature measurement. The temperature dependence of the hydration process is captured more directly in Figure 3.12 (b), in which the time to reach 99% rehydration is shown. Rather remarkable on this plot is the sharp difference in rehydration kinetics between 223 and 214 ºC: at 223 ºC the time to 99% rehydration is just 3 hr, whereas at 214 ºC it is 19 hr, virtually identical to the rehydration time at 205 ºC.

The nonmonotonic dependence of the hydration rate constant on temperature can be interpreted in terms of phase behavior. In the high temperature region, between 233 and 282 ºC, the hydration reaction occurs in the stability field of CsH_2PO_4 in its superprotonic phase and thus the reaction can be presumed to directly yield CsH_2PO_4 (*s*, *sp*). The increase in hydration rate with decreasing temperature (243 ºC and higher) can be attributed to an increase in the thermodynamic driving force for the reaction, and the behavior is unremarkable. At temperatures of 223 ºC and lower, the hydration reaction

occurs in the stability field of CsH_2PO_4 in its monoclinic phase. In general, at the lower temperatures the rate of hydration decreases, but the trend is not gradual. Instead, a sharp drop in rate is observed between 223 and 214 ºC, strongly suggesting a change in mechanism, despite the occurrence of the rehydration within the same stability field. We suggest that the behavior may be explained by the metastable occurrence of superprotonic CsH_2PO_4 at 223 ºC. It has been observed elsewhere that, on cooling superprotonic CsH_2PO_4, the high temperature phase can be retained in a supercooled state for long periods below the thermodynamic transition temperature of 228 ºC [12]. In the present experiments, it is plausible that the cubic phase is nucleated during the process of cooling to the anneal temperature of 223 ºC and further transformation at this temperature leads to continued growth of the cubic phase. The discontinuity in rehydration rates between 223 and 214 ºC would then be directly attributable to a difference in the crystalline structure of the hydrated phase. If this interpretation is correct, the implication is that the diffusion coefficient of neutral water through polycrystalline CsH_2PO_4 is substantially higher for the cubic, superprotonic form than the monoclinic, paraelectric form. The slight decrease in kinetics as temperature is lowered from 243 to 223 ºC may be a result of a decrease in the diffusion coefficient in cubic CsH_2PO_4 with decreasing temperature.

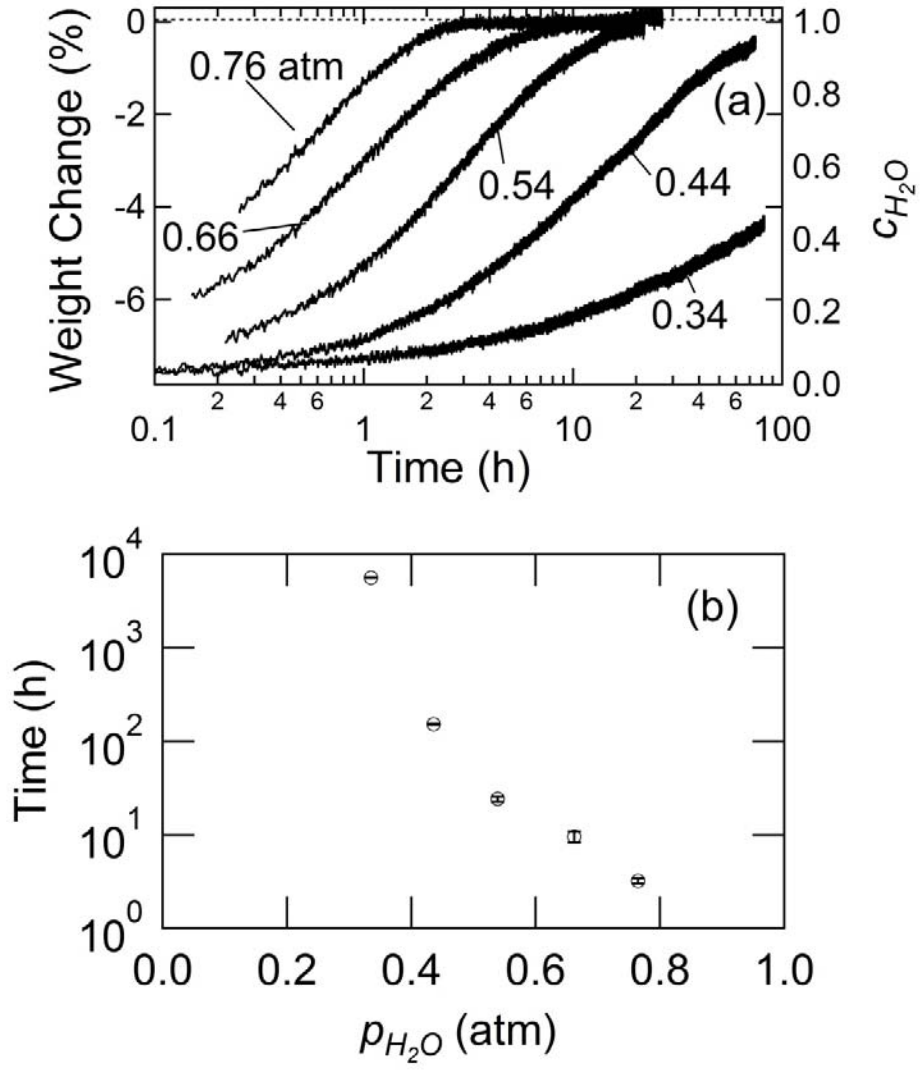

Figure 3.13. Isothermal hydration behavior of composite CsPO3(s) and SiO2 under several different p_{H2O} at T = 243 °C: (a) time dependent behavior; and (b) hydration rate, defined as time to 99% of reaction completion.

The isothermal rehydration behavior, evaluated in the second set of experiments, shows a similarly strong dependence on water partial pressure p_{H_2O}, Figure 3.13 (for the given temperature of 243 ºC). It is first noted that because a different sample, with different microstructure, than the first series is employed, the absolute behavior cannot be

compared between the two series. Furthermore, in this case, initial weight gain under high humidity occurs before the measurement system is stabilized in the new condition, and the effective zero-point in time has been estimated by fitting an Avrami expression to the later time data. As with the first set of experiments, the quench step from 330 ºC requires the system to traverse the stability field of the liquid phase. Nevertheless, again, the weight gain is monotonic and no plateaus are evident, indicating a single-step hydration from $CsPO_3$(s) to CsH_2PO_4(s, sp). Not surprisingly, the time to 99% completion of the hydration reaction, Figure 3.13 (b), decreases monotonically with increasing water partial pressure. By definition, the driving force for the reaction increases with increasing p_{H_2O}. In addition to this factor, enhanced surface kinetics may also contribute to the enhanced rate at high p_{H_2O}.

4. Conclusions

By making use of silica as an additive, equilibrium phase behavior of CsH_2PO_4 with respect to dehydration was accessed. The silica, which does not react with CsH_2PO_4, leads to a fine microstructure that facilitates equilibration with the atmosphere on measurable timescales. All aspects of the phase behavior so determined are consistent with thermodynamic expectations. The phase boundaries in the Arrhenius phase diagram (Figure 3.9) are, furthermore, linear, and permit evaluation of the enthalpies and entropies of the associated dehydration reactions (Table 3.2). The phase boundaries meet at the triple point connecting CsH_2PO_4(*s*,*sp*), $CsPO_3$(*s*), and $CsH_{2(1-x)}PO_{4-x}$(*l*), located at p_{H_2O} = 0.35 ± 0.2 atm and T = 267.5 ± 1.0 ºC, with slopes also consistent with thermodynamic expectations. The thermodynamic stabilities of the liquid dehydrate, $CsH_{2(1-x)}PO_{4-x}$(*l*), and

of CsH_2PO_4 are demonstrated by the fact that, in the relevant stability fields, any dehydration is reversed and the compounds recovered. On heating under low p_{H_2O}, dehydration occurs via a single step reaction, reflecting the direct formation of $CsPO_3(s)$ from $CsH_2PO_4(s,sp)$, whereas at high p_{H_2O}, it occurs via a two-step process involving the appearance of $CsH_{2(1-x)}PO_{4-x}(l)$ at intermediate temperatures. The much greater heating rate dependence of the second step suggests a sluggish mechanism involving H_2O diffusion through a continuous liquid layer. Overall, the dehydration temperatures determined in this work are shifted to lower values than those previously reported, where the discrepancy can be understood in terms of the extreme challenge in attaining equilibrium behavior, particularly at lower temperatures. Rehydration and conversion of $CsPO_3(s)$ to $CsH_2PO_4(s)$ occurs over a period of several hours, depending on temperature, water partial pressure, and morphology of the metaphosphate. As might be expected, high p_{H_2O} and small particles favor rapid rehydration, whereas the temperature dependence of rehydration behavior is nonmonotonic, reaching its fastest rate in the vicinity of the superprotonic transition.

Bibliography

1 Ikeda, A. & Haile, S. M. "The thermodynamics and kinetics of the dehydration of CsH_2PO_4 studied in the presence of SiO_2". *Solid State Ionics* **213**, 63-71, (2012).

2 Boysen, D. A., Uda, T., Chisholm, C. R. I. & Haile, S. M. "High-performance solid acid fuel cells through humidity stabilization". *Science* **303**, 68-70, (2004).

3 Haile, S. M., Chisholm, C. R. I., Sasaki, K., Boysen, D. A. & Uda, T. "Solid acid proton conductors: from laboratory curiosities to fuel cell electrolytes". *Faraday Discussions* **134**, 17-39, (2007).

4 Taninouchi, Y.-k., Uda, T., Awakura, Y., Ikeda, A. & Haile, S. M. "Dehydration behavior of the superprotonic conductor CsH_2PO_4 at moderate temperatures: 230 to 260 °C". *Journal of Materials Chemistry* **17**, 3182, (2007).

5 Taninouchi, Y.-k., Hatada, N., Uda, T. & Awakura, Y. "Phase Relationship of CsH_2PO_4-$CsPO_3$ System and Electrical Properties of $CsPO_3$". *Journal of the Electrochemical Society* **156**, B572, (2009).

6 Taninouchi, Y.-k., Uda, T. & Awakura, Y. "Dehydration of CsH_2PO_4 at temperatures higher than 260 °C and the ionic conductivity of liquid product". *Solid State Ionics* **178**, 1648-1653, (2008).

7 ICDD 45-0617

8 ICDD 37-0027

9 Uesu, Y. & Kobayashi, J. "Crystal structure and ferroelectricity of cesium dihydrogen phosphate CsH_2PO_4". *Physica Status Solidi (a)* **34**, 475-481, (1976).

10 Ikeda, A. & Haile, S. M. "Examination of the superprotonic transition and dehydration behavior of $Cs_{0.75}Rb_{0.25}H_2PO_4$ by thermogravimetric and differential thermal analyses". *Solid State Ionics* **181**, 193-196, (2010).

11 Yaglov, V. N., Rudko, P. K. & Navikov, G. I. "Dehydration of Cesium Dihydrogen Phosphate". *Russian Journal of Physical Chemistry,Ussr* **46**, 310-&, (1972).

12 Louie, M. W., Kislitsyn, M., Bhattacharya, K. & Haile, S. M. "Phase transformation and hysteresis behavior in $Cs_{1-x}Rb_xH_2PO_4$". *Solid State Ionics* **181**, 173-179, (2010).

Chapter 4 Phase behavior of cation doped cubic CsH_2PO_4

4.1. Introduction

Cubic CsH_2PO_4 has high conductivity and, as such, is attractive compound as a fuel cell electrolyte for operation in the temperature range of 230~280 ºC [1]. In an earlier publication we reported the thermodynamic and kinetic of the dehydration for cubic CsH_2PO_4[2]. The lower limit of operation temperature of CsH_2PO_4 fuel cell corresponds to the phase transition temperature, T_s = 227 ºC, from monoclinic to cubic phase. This polymorphic phase transition is independent of p_{H_2O}. On the other hand, the upper limit of the operation temperature corresponds to the dehydration temperature, T_d, which depends strongly on p_{H_2O}. For example, T_d is 290 ºC at p_{H_2O} = 0.8 atm and 230 ºC at 0.15 atm. The relatively narrow stability window for cubic CsH_2PO_4 presents challenges for fuel cell operation. While these are not insurmountable, increasing Td and lowering Ts are technologically desirable. In this work we evaluated the phase behavior in the CDP-RDP (RbH_2PO_4) and CDP-KDP(KH_2PO_4) pseudo-binary systems as a means for manipulating these temperatures. Beyond near-term implications for fuel cell operation, such a study has the potential to provide broad insight into the crystal-chemical factors governing superprotonic behavior.

At ambient conditions, CDP and RDP have distinct monoclinic structures, precluding the possibility of complete solid solubility. It has been shown, however, that Rb is highly soluble in monoclinic CDP, up to 80% at ambient temperatures[3]. The structure of monoclinic and cubic $Cs_{1-x}Rb_xH_2PO_4$ is reported by Cowan [3], Louie [4], Martsinkevich [5], and Matsuo [6]. They claimed that Rb has large solubility for both phases.

Cubic structure of RbH_2PO_4 and monoclinic structure ($P2_1/m$) are also reported by Botez [7] under high pressure. Therefore, the whole range solubility of cubic CDP and cubic RbH_2PO_4 is expected. Louie reported that T_s of $Cs_{1-x}Rb_xH_2PO_4$ increases by Rb content. We reported T_d of $Cs_{0.75}Rb_{0.25}H_2PO_4$ and it was slightly lower than CDP [8]. K, being only slightly smaller than Rb, is also a good candidate for the substitution on the Cs site. The structure of monoclinic or cubic $Cs_{1-x}K_xH_2PO_4$ has not reported. The examination of cubic CDP under equilibrium condition to avoid dehydration is a challenge. Therefore, the number of reports for these compounds is not many, except for conductivity measurements. Some studies were done under the unstable conditions before the dehydration reaction completes or under extremely high pressure.

In this work, we examined $Cs_{1-x}Rb_xH_2PO_4$ and $Cs_{1-x}K_xH_2PO_4$ under humid atmosphere and observed the properties directly in the equilibrium condition by X-ray diffraction (XRD), differential scanning calorimetry (DSC), and alternating current impedance (AC impedance) measurements. We determined the solubility, T_s and T_d, and developed phase diagrams of these compounds. The lattice size and conductivity were determined carefully, then, the effects of doping to these properties were discussed.

4.2. Experimental details

4.2.1. Sample preparation

Polycrystalline powders of CsH_2PO_4 and RbH_2PO_4 were synthesized by combining the starting reagents Cs_2CO_3 (Alfa Aesar, 99.99%) or Rb_2CO_3 (Alfa Aesar, 99.99%) and H_3PO_4 (ACS, 85% w/w aqueous solution) in a molar ratio of 1:2 in aqueous solution. The solutions were then gently heated, and solid CsH_2PO_4 and RbH_2PO_4

obtained upon evaporation of water. Samples of overall composition $Cs_{1-x}Rb_xH_2PO_4$ and $Cs_{1-x}K_xH_2PO_4$ were prepared from these starting materials. Stoichiometric aqueous solutions were prepared from the end-member compounds, and again solid precipitates were obtained upon inducing water evaporation. For further experimentation the resulting materials were ground with in a mortar and pestle to yield to powders with particle size of ~ 10 μm.

Chemical compositions were verified by X-ray energy dispersive spectroscopy (EDS), performed using an Oxford INCA 300 in conjunction with a scanning electron microscope (LEO 1550 VP) at an accelerating voltage of 15 kV. Samples in the CDP-RDP system were prepared directly from the precipitates described above. In this system slight differences were determined between the nominal and actual compositions and all results are presented in terms of the actual (measured compositions). In the case of the CDP-KDP system, the solubility of K into CDP was found to display limited and highly temperature dependent solubility, and accordingly efforts were made to capture the high temperature composition. 30 at.% K-doped CDP powder was formed into discs, 9.3 mm in diameter and typically 1 mm in thickness, by uniaxial pressing. Samples were annealed in a quartz container for 4 days under humidified atmosphere (p_{H_2O} = 0.8 atm) at 204 and 244 ºC and then rapidly quenched by putting the container into water to minimize exsolution. Then, the discs were roughly ground to be powder form.

Table 4.1. The dopant concentrations which were obtained by EDS measurements

Sample	Nominal (at.%)	c_{Rb} (at.%)	Sample	Nominal (at.%)	c_K (at.%)
19%Rb	20	19.4 ± 1.2	30%K_200°C	30	17.5 ± 2.5
50%Rb	50	50.1 ± 1.3	30%K_240°C	30	27.1 ± 2.4
78%Rb	75	77.8 ± 1.8			

4.2.2. In situ XRD measurements

XRD measurements were carried out using an X'pert MD (Panalytical) diffractometer equipped with an in-house-constructed sealed, high-temperature stage (Figure 4.1).

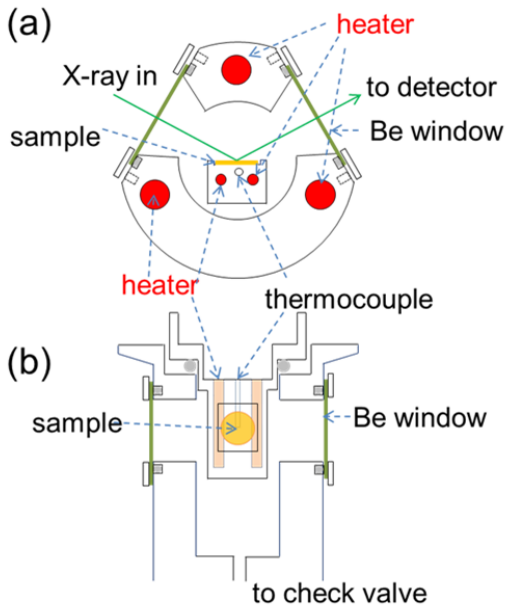

Figure 4.1. The schematic view of the high temperature sealed stage (a) side view and (b) up view

Two resistive heaters in the sample stage provide heat to the sample, the temperature of which is monitored and controlled using a thermocouple (K-type) also embedded in the stage. Three additional resistive heaters, typically set to ~ 150 °C, are embedded in the walls of the chamber and are utilized to prevent water condensation. The chamber is further equipped with a check valve to limit the system pressure to 2 atm. Be windows permit incident and diffraction X-rays to enter and exit the chamber. A thin glass plate was placed on the sample stage to prevent possible reaction between the sample and stage material. For the measurement, 20 at.% Si was added to the sample powder as an internal 2θ reference. No reaction between Si and the materials investigated was observed.

Measurements were typically carried out in the temperature range 150 to 300 °C in 10 °C increments. At each temperature step, measurements were started after waiting more than 30 minutes for equilibration of the sample.

Exemplary diffraction data obtained from this system are presented in Figure 4.2 for the parent compound CDP. Consistent with the widely confirmed phase transformation behavior, the data show CDP to remain entirely in the monoclinic phase to 220 °C. A two-phase mixture of the monoclinic and cubic phases is obtained at 230 °C, and from 240 to 290 °C only diffraction peaks from the cubic phase are evident. The material becomes entirely amorphous at 300 °C, corresponding to the liquid phase. Based on the retention of the cubic phase to such high temperature [1], we estimate that a water partial pressure of ~ 1 atm is attained in the sealed chamber. For all measurements, crystallographic parameters were determined by Rietveld refinement using RIETAN-FP software [9]. The known thermal expansion behavior of Si [10] provided an internal 2 θ standard to ensure accurate lattice parameter refinement. To facilitate refinement of atomic positions, the P-O distance was fixed (at 1.52 Å [3]) irrespective of temperature. The refined parameters for CsH_2PO_4 (Pm3m) structures are shown in Table 4.2. Where occupancy of Cs1, P1 is 1 and that of O1 is 0.1667, T is the temperature of the sample; a is the lattice constant; x, y, z is the atomic coordinate of the atoms; B is the isotopic atomic displacement; S is the goodness of the fit ; and R_p is the R-factor.

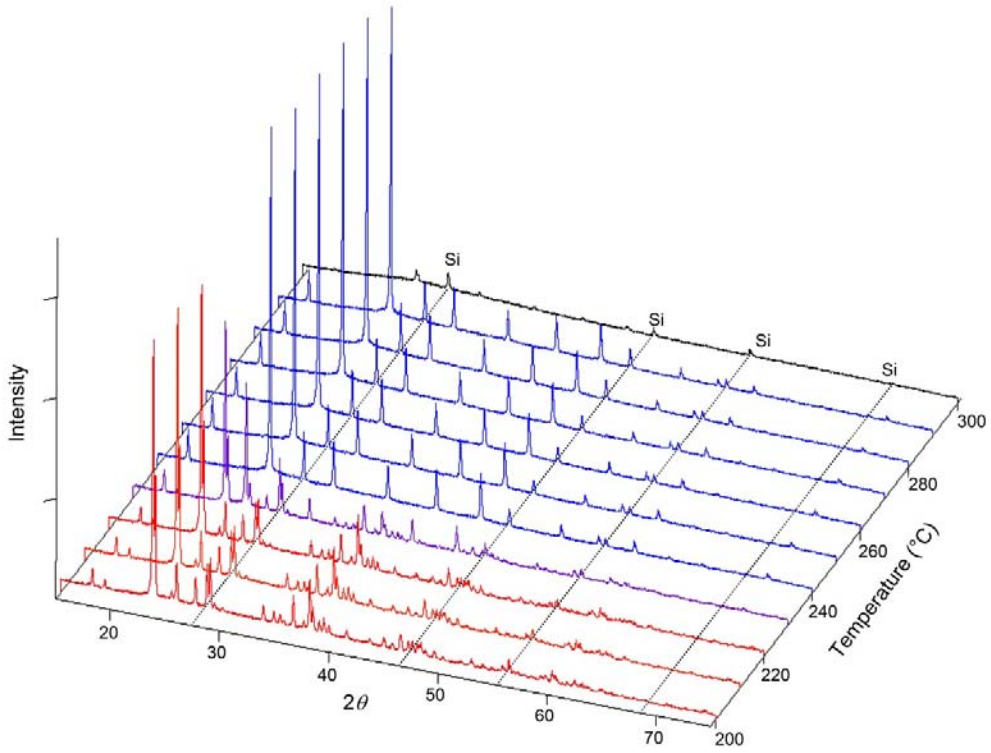

Figure 4.2. XRD profile of CDP with Si (as internal standard) at several temperatures

Table 4.2. The fitting parameters of Rietveld refinements for CsH_2PO_4

T (°C)	a (Å)	Cs1/Cs				P1/P				O1/O				S	R_p
		x	y	z	B	x	y	z	B	x	y	z	B		
230	4.9673(9)	0	0	0	8.2	0.5	0.5	0.5	4.4	0.5	0.221	0.374	4.4	----	----
240	4.9683(2)	0	0	0	8.2(1)	0.5	0.5	0.5	4.4(2)	0.5	0.221(1)	0.374(1)	4.4(2)	1.38	3.94
250	4.9707(2)	0	0	0	8.7(1)	0.5	0.5	0.5	4.9(2)	0.5	0.222(1)	0.374(2)	4.9(2)	1.32	3.79
260	4.9728(2)	0	0	0	8.7(1)	0.5	0.5	0.5	4.8(2)	0.5	0.222(1)	0.373(2)	4.8(2)	1.34	3.80
270	4.9748(2)	0	0	0	8.9(1)	0.5	0.5	0.5	4.7(2)	0.5	0.223(1)	0.374(1)	4.7(2)	1.30	3.77
280	4.9764(2)	0	0	0	9.3(1)	0.5	0.5	0.5	4.9(2)	0.5	0.223(1)	0.367(2)	4.9(2)	1.31	3.80
290	4.9777(2)	0	0	0	9.4(1)	0.5	0.5	0.5	6.0(2)	0.5	0.222(1)	0.374(1)	6.0(2)	1.18	3.49

4.2.3. DSC measurements

Thermal analysis was performed using an in-house-constructed differential scanning calorimeter (DSC), shown schematically in Figure 4.3, capable of accessing temperatures as high as 350 °C under water partial pressures as high as 0.8 atm. The system is a modification to an apparatus described previously as part of the authors' study of the phase behavior of CsH_2PO_4 [2]. In the present design, the sample stage is made of constantan alloy and two junctions of E-type thermocouples are welded to it at the lower side. The resistance of the path of a chromel-wire, constantan sample stage to the other chromel wire generates the thermoelectric voltage which is generated between sample and reference Pt container. The voltage is measured using a nanovolt meter (Keithley 182) with ± 100 nV accuracy, corresponding to a precision of 0.02 mW. The sample temperature is measured using a thermocouple welded to the sample side of the constantan sample stage. Information on the heating and humidification system is available in previous report [2]. Prior to examination, the sample powders were combined with 20 wt.% amorphous silica powder (Alfa Aesar, S.A 330–410, 325 mesh) and homogenized by mechanical agitation. Then they were annealed 2 hours at 350 °C and 6 hours at 250 °C under p_{H_2O} = 0.6 atm. By this heat treatment, the fine microstructured, doped CDP is formed and it accelerates the dehydration or hydration kinetic as we mentioned in the previous report [2]. The typical heating rate is 0.5 K/min, and the typical sample mass is 60 mg in this work. The typical peak height of phase transition of CsH_2PO_4 is 5.0 mW in this measurement condition.

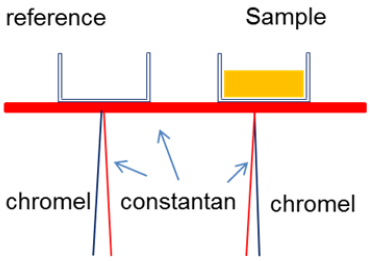

Figure 4.3. The schematic view of the measurement cell of DSC

4.2.4. AC impedance measurements

Conductivity of the samples was determined by A.C. impedance spectroscopy (HP 4284A). Samples were formed into discs, 9.3 mm in diameter and typically 2 mm in thickness, by uniaxial pressing ~491 MPa for 10 min to achieve a density of 99%. Sputtered films of Pt or Ag, approximately 100 nm in thickness, served as electrodes. Samples were placed in a horizontal tube furnace and held in place using Pt wire current collectors. Measurements were carried out in the temperature range 180 to 280 °C under humidified N_2, p_{H_2O} = 0.9 atm, achieved by passing the inlet gas first through a water bubbler held at 98 °C. Step changes in temperature of 5 to 10 °C were applied and the system allowed to equilibrate for at least 30 minutes or until the impedance response had stabilized before recording the final data. The temperature was measured using an alumina sheathed E-type thermocouple placed in direct contact with the sample.

4.3. Results and discussion

4.3.1 Overall phase characteristics

Integration of the results of the comprehensive structural, thermal and transport measurements of the materials, yielded the phase diagrams presented in Figure 4, part (a) showing the CsH_2PO_4-RbH_2PO_4 system and (b) the CsH_2PO_4-KH_2PO_4 system. Circles designate phase transition temperatures, squares dehydration temperatures, and triangles

phase boundaries, where data in blue were acquired by DSC measurements, those in black by in situ XRD measurements, and those in red by EDS chemical analysis. The CDP-RDP system has simple isomorphous phase behavior. The end-members are entirely miscible at temperatures above 150 °C in both the monoclinic and cubic phases. The superprotonic transition temperature monotonically increases and the dehydration temperature largely decreases with increasing Rb content, resulting in a narrowing of the superprotonic region. At ambient temperature (not shown) the solubility limit of Rb into CDP is ~ 80 at. % [3], and the transformation of RDP into the CDP-like monoclinic phase at 117 °C [11] facilitates complete solid solubility above this first transition.

In sharp contrast to the CsH_2PO_4-RbH_2PO_4 system, the CsH_2PO_4-KH_2PO_4 system displays eutectic behavior. On introduction of K into CDP, the superprotonic transition temperature shifts downward until the eutectic temperature of ~208 °C (20 °C lower than the superprotonic temperature of neat CDP) is reached. The maximum solubility of K into monoclinic CDP is ~ 20 at %, and that into cubic CDP is 27 at.%. The high temperature solubility limit is surprisingly temperature insensitive. Beyond 27 at% the cubic CDP-rich phase co-exists a KPD-rich phase, where the latter either adopts the crystalline monoclinic structure of KDP [12], or at higher temperature, becomes a liquid. Overall, dehydration temperature in this system decreases sharply on introduction of K, particularly so within the single-phase superprotonic region. Accordingly, there is an overall shift of the stable cubic region to lower temperature with increasing K content, along with a slight narrowing of its stability window.

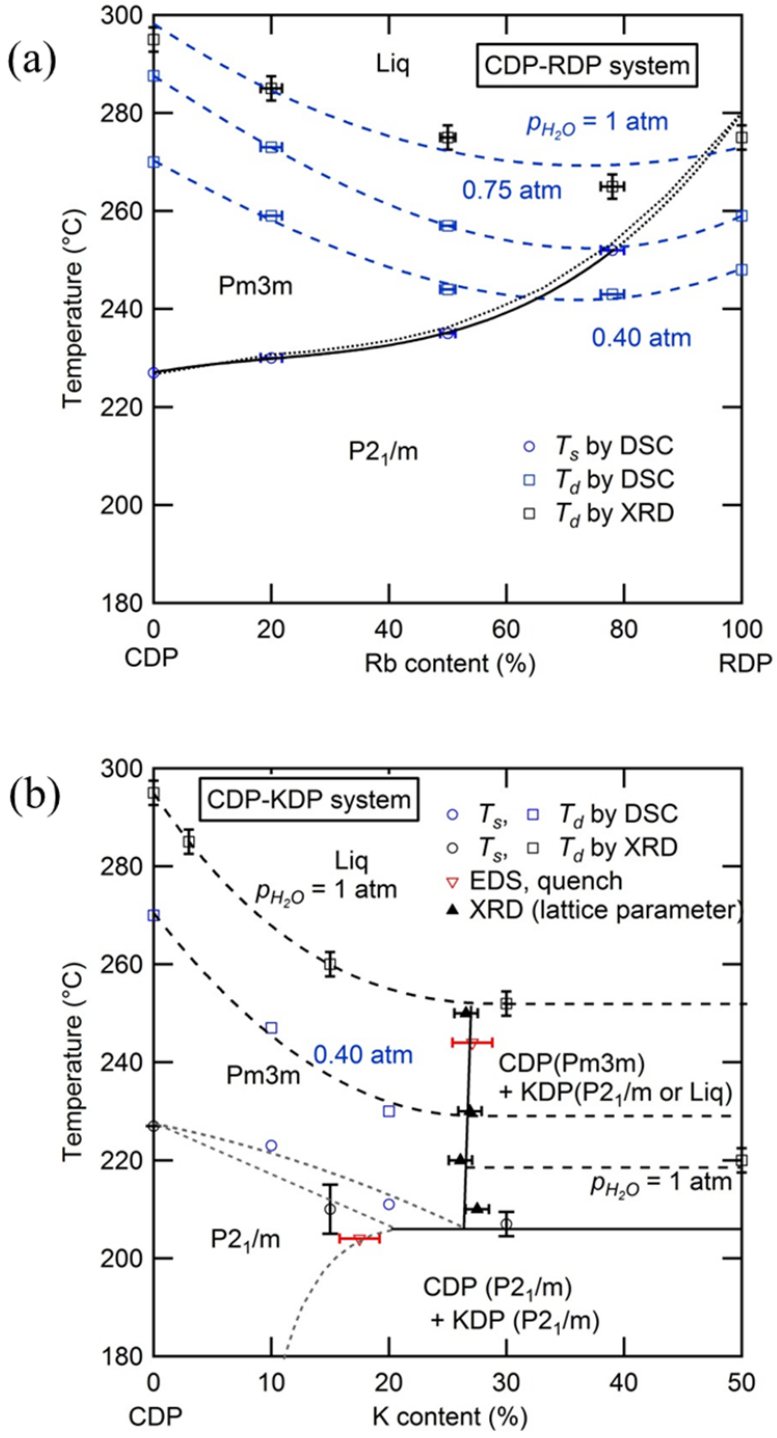

Figure 4.4 Phase diagram of (a) CDP-RDP and (b) CDP-KDP systems

4.3.2 Determination of Phase Behavior in the $Cs_{1-x}Rb_xH_2PO_4$ system: $0 \leq x \leq 1$

In situ XRD data were collected for the specific compositions in the $Cs_{1-x}Rb_xH_2PO_4$ system of x = 0.19, 0.5, 0.78 (the actual compositions, Table 4.1) and for the end-member RbH_2PO_4, in addition to CsH_2PO_4 as reported above. Example diffraction results are presented in Figure 4.5 both as function of temperature (parts a and b) for given compositions (x = 0.5, 1), and as a function of composition (part c) at high temperature (T = 260 °C). The data shows that the $Cs_{1-x}Rb_xH_2PO_4$ compounds transform from the CDP-type monoclinic phase to the cube CsCl-type phase of superprotonic CsH_2PO_4. Based on prior studies, the solubility limit of Rb into CDP at ambient temperatures is ~ 80 at. % [3]. Beyond this composition, Rb rich compositions and, in particular, the RbH_2PO_4 end-member adopt a distinct monoclinic structure of space group $P2_1/m$. At 117 °C RbH_2PO_4 transforms to the CDP-type monoclinic structure [11], consistent with the complete solid-solubility between CDP and RDP at high temperature. Furthermore, in contrast to all other compositions examined in the $Cs_{1-x}Rb_xH_2PO_4$ system, no cubic phase was observed for RbH_2PO_4. The diffraction peaks are lost at 270 °C suggesting the occurrence of a liquid phase. It is possible the cubic superprotonic phase may be accessible under higher p_{H2O}, as it is under high total pressure (1 GPa) [7]. However, such conditions were not examined here. For all the compounds, at sufficiently high temperatures, the behavior was marked by the absence of diffraction peaks. By analogy to CsH_2PO_4, this behavior is taken to reflect presence of a partially dehydrated liquid and the temperature at which the crystalline phase is no longer observed as taken to be the decomposition temperature. Weight loss at this temperature was not independently

confirmed, but the DSC measurements, as discussed below, are consistent with this interpretation.

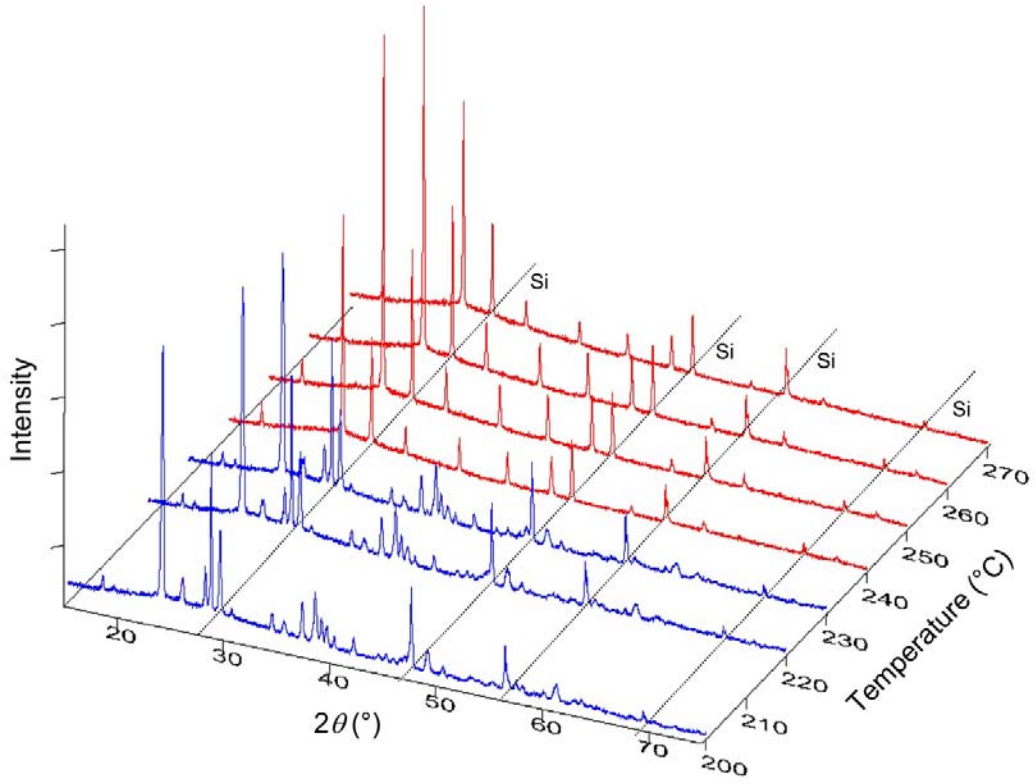

Figure 4.5(a). XRD profiles of $Cs_{0.5}Rb_{0.5}H_2PO_4$ with Si (as internal standard) at several temperatures

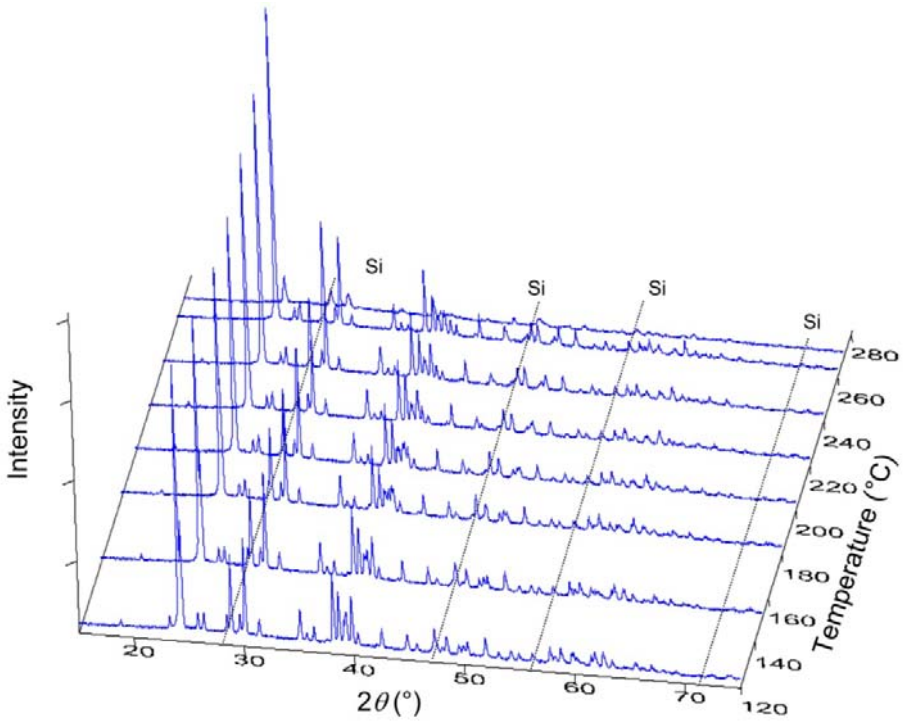

Figure 4.5(b). XRD profiles of RbH_2PO_4 with Si (as internal standard) at several temperatures

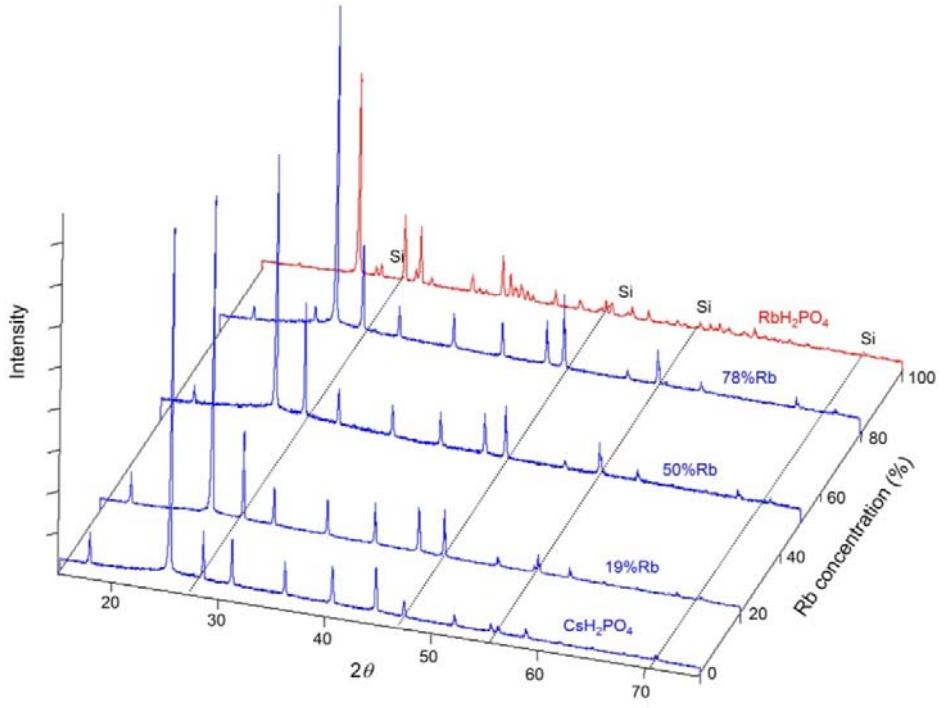

Figure 4.5 (c). XRD profiles of $Cs_{1-x}Rb_xH_2PO_4$ with Si (as internal standard) at 260°C

Selected DSC profiles for compounds in the $Cs_{1-x}Rb_xH_2PO_4$ system are presented in Figure 6, part a for fixed x = 0.19 and part b for fixed p_{H2O}. Two thermal events are evident in all cases. At fixed stoichiometry, the first event occurs at a given temperature, 230 °C in this example, whereas the second depends on the water partial pressure. This behavior is consistent with the identification of the first transition as a polymorphic transformation, involving no change in sample composition, and of the second transition as a dehydration or partial dehydration event, involving loss of H_2O from the structure. With increasing Rb content (Figure 6b), the temperature of the polymorphic transition monotonically increases, whereas the decomposition temperature generally decreases but finally increases slightly for the RbH_2PO_4 end-member. These features are reflected in the phase diagram presented in Figure 4(a), for which T_S and T_d are defined in terms of the onset of the thermal anomaly.

In principle, the monoclinic to cubic phase transition should pass through a two-phase region. The relatively sharp DSC peaks, spanning no more than ~ 9 K, indicate that the two-phase region is rather narrow, as displayed in the phase diagram. No attempt was made in the diffraction measurements to capture the compositional breadth of the two phase region, a rather subtle feature of the phase diagram. Similar to the superprotonic transition, the dehydration anomaly displays a relatively sharp peak, despite the likely transformation to a partially dehydrated liquid and continuous weight loss at high temperature [2]. Such behavior is similar to that observed in CDP in which the dehydration is confirmed to occur over a wide temperature range but with a relatively sharp thermal signal, reflecting the fact that the majority of the weight loss occurs shortly after the onset of dehydration. The enthalpies of transformation/dehydration are largely independent of

composition, with a typical value of 11.5 kJ/mol for the superprotonic transition and 31.4 kJ/mol for dehydration (comparable to the thermal properties of CDP [2]).

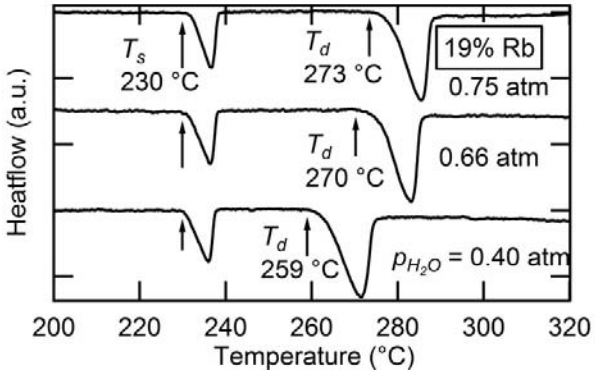

Figure 4.6(a). DSC profiles of $Cs_{1-x}Rb_xH_2PO_4$ (x = 0.19) under several water vapor pressure. The first peaks for each profiles are phase transition and the second peaks are dehydration temperature.

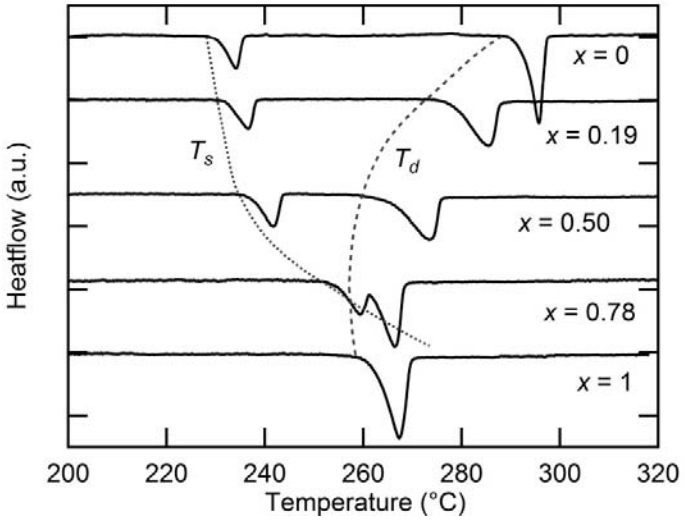

Figure 4.6(b). DSC profiles of $Cs_{1-x}Rb_xH_2PO_4$ (x = 0~1) under p_{H2O} = 0.75 atm.

4.3.3 Phase Behavior in the $Cs_{1-x}K_xH_2PO_4$ system: $0 \leq x \leq 0.3$

In the case of the $Cs_{1-x}K_xH_2PO_4$ system, *in situ* XRD data were collected for the specific compositions x = 0.03, 0.15, and 0.3, with higher potassium concentrations being

of less interest with respect to superprotonic behavior. Selected results are presented in Figure 4.7.

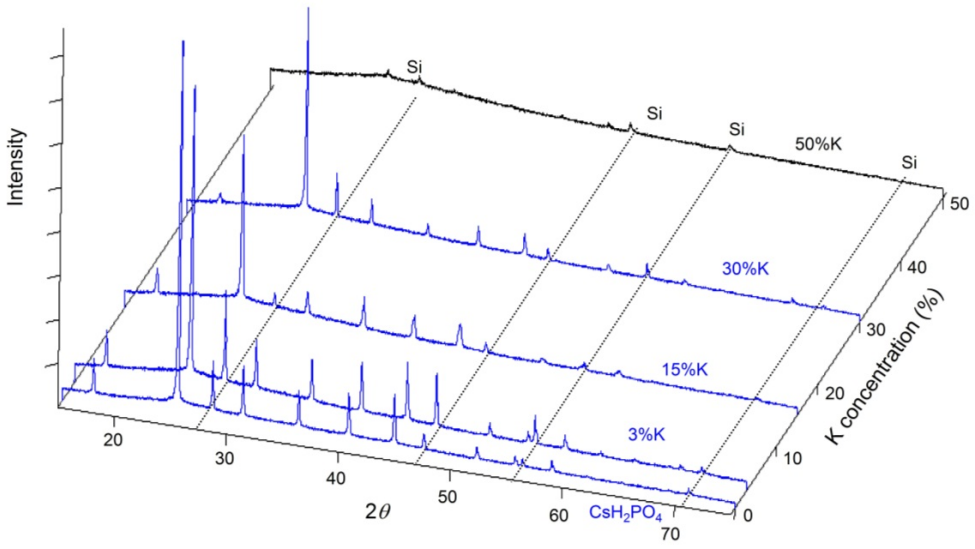

Figure 4.7(a). XRD profile of $Cs_{1-x}K_xH_2PO_4$ with Si (as internal standard) at 250°C

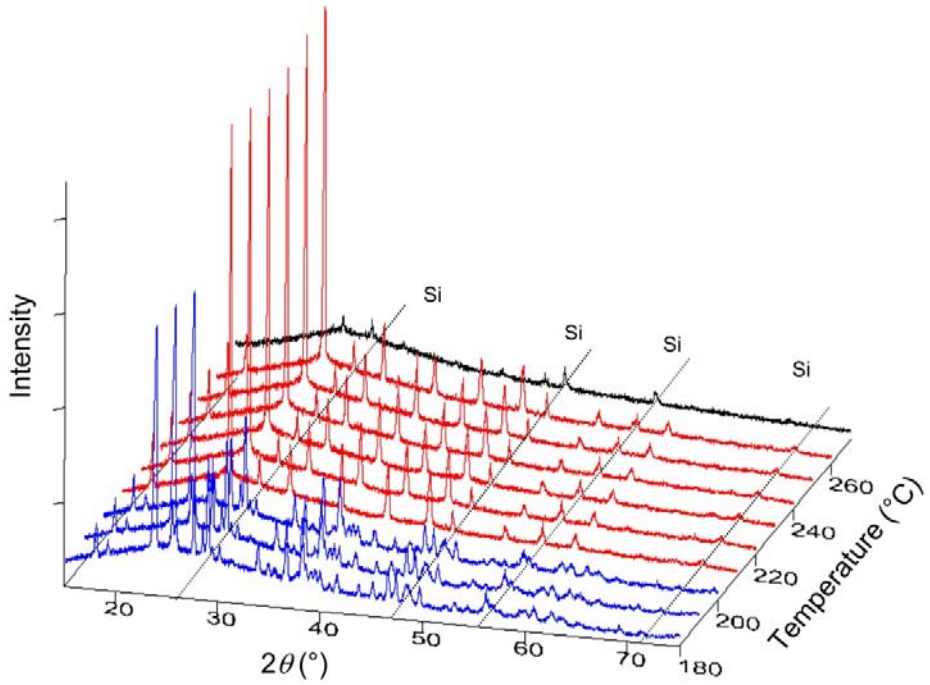

Figure 4.7(b). XRD profile of $Cs_{1-x}K_xH_2PO_4$ (x = 0.15) with Si at several temperatures.

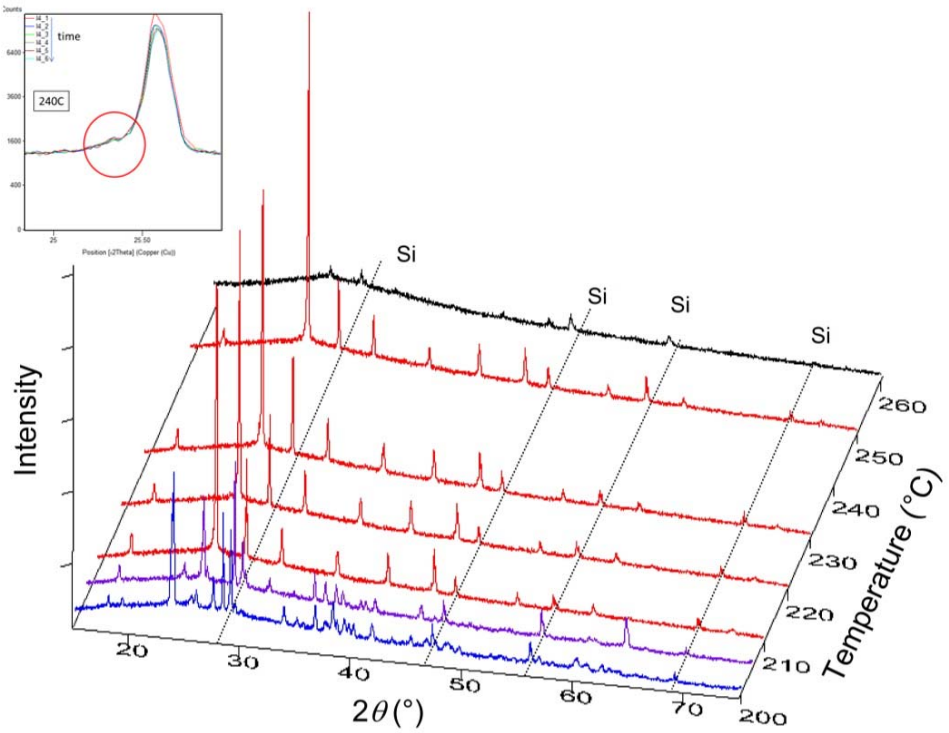

Figure 4.7(c). XRD profile of $Cs_{1-x}K_xH_2PO_4$ (x = 0.3) with Si at several temperatures.

At 250 °C, the diffraction data show clear evidence of the cubic CsCl-type phase for all four compositions (Figure 4.7a). Since the x = 0.50 composition has obviously larger background, the liquid phase exists as the secondary phase at this temperature. As a function of temperature, the x = 0.15 composition is composed of a mixture of the CDP-type and KDP-type monoclinic phases up to 200 °C (Figure 4.7b). At temperatures between 210 and 260 °C only peaks from the CsCl-type cubic phase are evident, and finally at 270 °C all diffraction peaks disappear and presumably the liquid dehydrate appears. This behavior is generally reproduced for the x = 0.3 composition (Figure 4.7c). A distinction can be observed 210~240 °C, in which case a small peak at 2θ = 25.3° indicates the existence of KDP-type monoclinic. It is hard to see in the lower temperature region due to overlap with CDP-type monoclinic peaks.

At first glance, the diffraction results suggest that the cubic phase of CDP can accommodate as much as 30% K. An evaluation of the lattice parameter dependence on composition, however, suggests a lower solubility limit. In Figure 4.8 is shown the lattice parameter of cubic CKDP as a function of composition at 230 and 250 °C. At low K content, the cell constant decreases linearly, in accord with Vegard's empirical law. The data points for the x = 0.3 composition, however, deviate from the linear relationship. Extrapolation of the lattice parameter trendline to the measured values at x = 0.3 suggests an actual composition (*i.e.* solubility limit) of 27 at % at both temperatures. This method of analysis is justified by the observation of a linear dependence of lattice parameter on dopant content in the superprotonic cubic phase within RDP-CDP system (as discussed below).

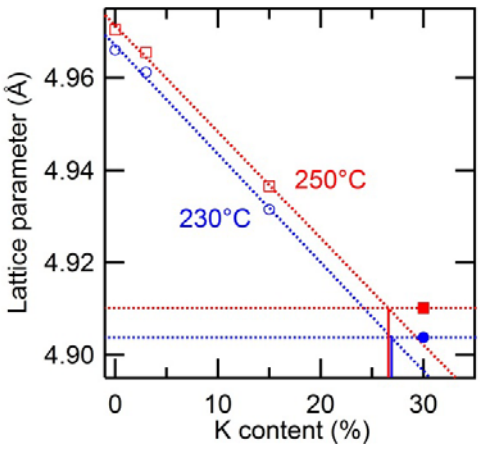

Figure 4.8. The lattice parameter change by K doping at 230 and 250 °C

As in the case of the CDP-RDP system, diffraction measurements at sufficiently high temperatures showed that the CDP-KDP materials become amorphous, for all compositions examined. Again, it is presumed that the amorphous phase is a liquid dehydrate, as supported by the DSC measurements. Similar to the introduction of Rb into superprotonic CDP, it is evident that introduction of K lowers the dehydration

temperature for a given p_{H2O}. In this case, however, the transition temperature to the cubic phase also decreases with K content and the temperature window for the superprotonic phase does not become vanishingly small.

DSC measurements under several water vapor pressures were performed for the 10 and 20%K compounds. Figure 4.9 shows DSC profiles 10%K. According to the result of XRD measurements and reported DSC profile of CDP[2], the first peaks are corresponding to phase transformation with the starting temperature of the reaction, T_s, and the second peaks are corresponding to the first dehydration with that temperature, T_d. The peak for the first dehydration reaction of potassium doped CDP has a tail in the low temperature side. It can be due to the phase separation to potassium rich liquid and cesium rich solid (cubic).

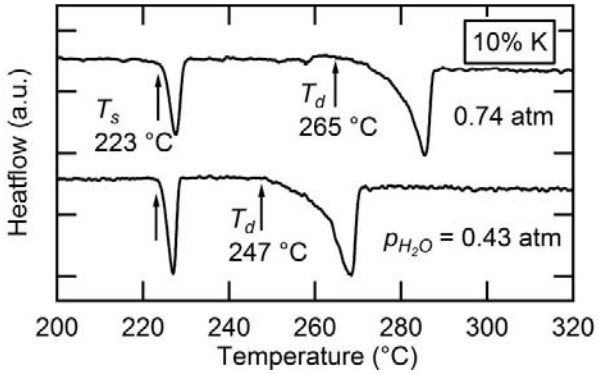

Figure 4.9. DSC profiles of the 10%K composition at p_{H2O} = 0.43 and 0.74atm.

4.3.4 Structural and Transport Properties

The thermal expansion behavior of the cubic phase in the CDP-RDP and CDP-KDP systems is summarized in Figure 4.10 and Table 4.3, where the coefficients of thermal expansion, α, in the table are of the form $\Delta a/a_0 = \alpha(T-T_0)$, with T_0 = 260 °C. The

thermal expansion coefficients are around 4×10^{-5} K^{-1} for each of the compounds with negligible impact from doping. The volume expansion $\Delta V/V_0$ for CDP which was determined as $1.57(3) \times 10^{-4}$ K^{-1} in this work is slightly smaller than that in Louie [4] as $1.98(2) \times 10^{-4}$ K^{-1}. The obtained lattice parameters of CDP well agree with Louie's values and are slightly larger than the other reports [13-15].

Table 4.3. The thermal expansion coefficients of doped CDP

Compound	A ($10^{-5}K^{-1}$)	a_0 (Å)	T (°C)	Compound	A ($10^{-5}K^{-1}$)	a_0 (Å)	T (°C)
undoped	3.92(11)	4.9724(2)	230-290	3 %K	3.95(13)	4.9675(2)	220-280
19 %Rb	3.42(17)	4.9440(2)	230-280	15 %K	4.54(48)	4.9388(8)	210-250
50 %Rb	3.85(19)	4.8991(2)	240-270	30 %K	4.65(10)	4.9107(6)	210-250
78 %Rb	——	4.8612(3)	260				

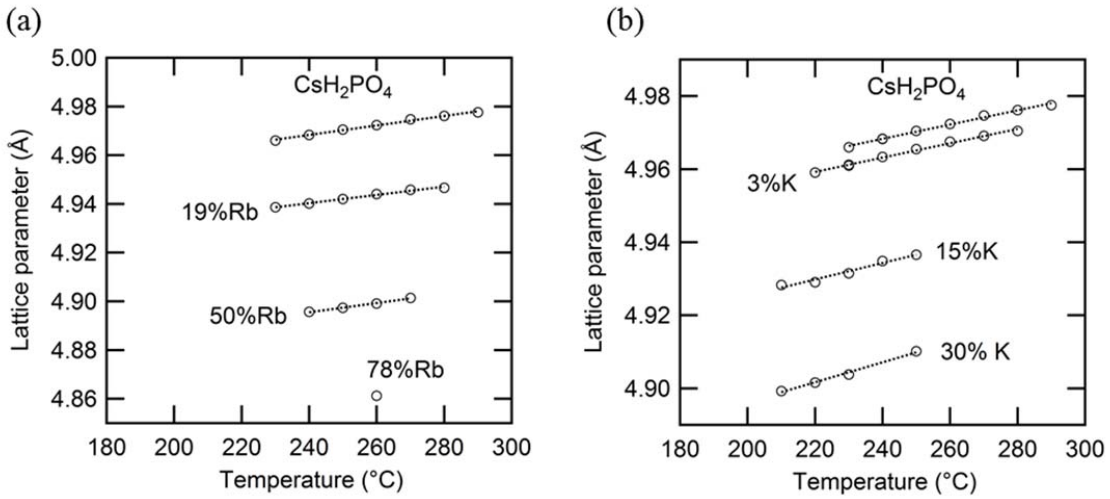

Figure 4.10. Lattice parameters of (a)Rb and (b) K doped CDP at several temperatures under p_{H_2O} ~ 1 atm (the error of the lattice parameters are within the marker size)

Figure 4.11 shows the relation between the weighted mean ionic radii [16] and the lattice parameters at 260 °C. The plots of the lattice parameters agree with each other rather well, indicating that the lattice constant of solid solution cubic phase depends simply on the averaged ionic radius of cations in the alkali ion site.

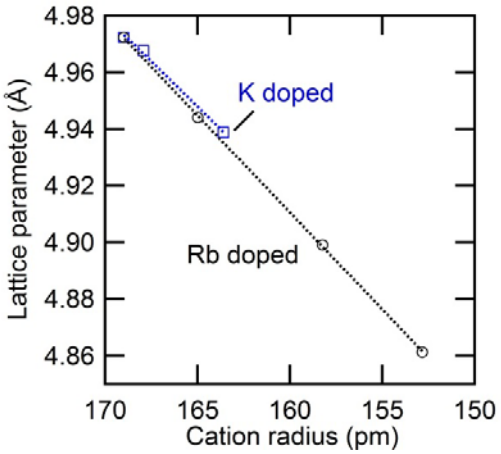

Figure 4.11. Relation between averaged ionic radius and lattice parameters of Rb and K doped CDP

The AC impedance measurements revealed that the solid solution cubic phase has high conductivity in both the CDP-RDP and the CDP-KDP systems. The impedance spectra at low temperature displayed typical features [1] in which a single, high-frequency arc reflects transport through the polycrystalline solid electrolyte, and at high temperature transport through the electrolyte is reflected in terms of the offset of the response along the real axis, Figure 4.12. In addition, the conductivity determined here for CDP is in excellent agreement with the results reported in the literature [1,17-19]. Focusing on transport in the high temperature phase, Figure 4.13, it is evident that doping uniformly decreases the conductivity of CDP in proportion with the dopant concentration. Furthermore, potassium doping makes deeper impact than Rb. The activation energies of conductivities were calculated from temperature dependence of conductivities. It turns out the activation energy decreases by doping concentration, and potassium doping makes deeper impact. Figure 14 shows the pre-exponential factors and the activation energies against the cation radius. It was turns out that both the pre-exponential factors and the activation energies

are getting smaller by doping, and the impact of K doping is greater than that of Rb doping against the averaged cation radius.

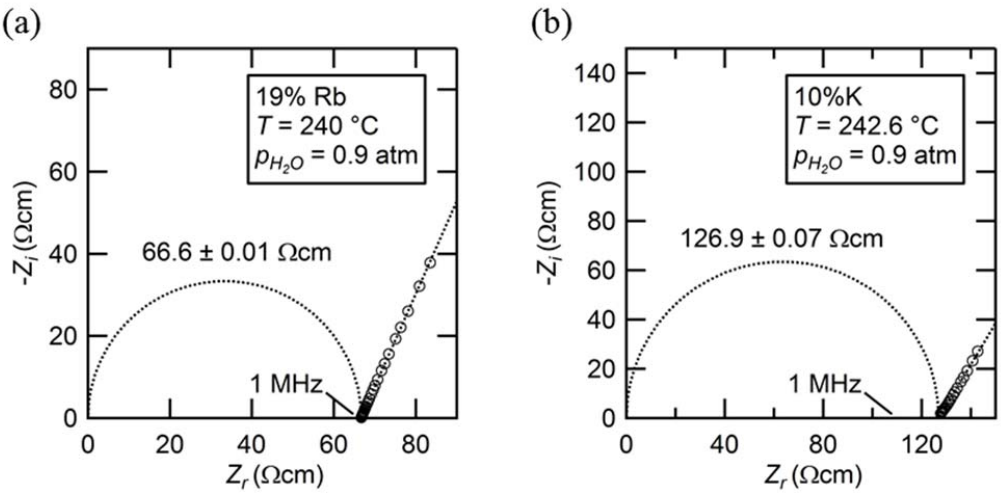

Figure 4.12. AC impedance spectrum of (a) 19%Rb (b) 10%K doped CDP

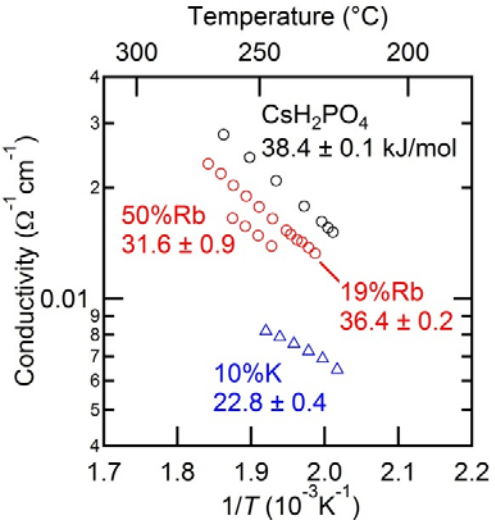

Figure 4.13. Conductivity of doped CDP (cubic) at several temperatures

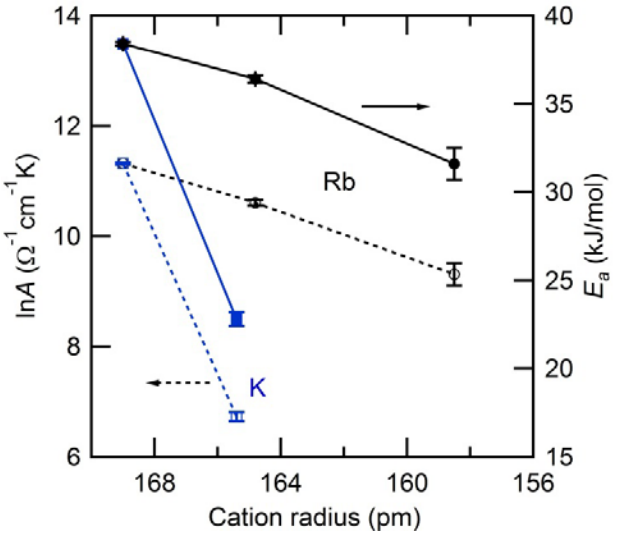

Figure 4.14. The pre-exponential factor, A and the activation energy, E_a against the cation radius for the form of $\sigma T = A\exp(-E_a/kT)$

Figure 4.14 shows the pre-exponential factors and the activation energies against the cation radius. It was turned out that both the pre-exponential factors and the activation energies get smaller by doping, and the impact of K doping is greater than that of Rb doping against the averaged cation radius. It suggests that the proton jumps, which are dominant on the long-range proton migration, are affected by the dopant atoms. Ishikawa [17] studied PFG-NMR and ^{1}H NMR T_1, and reported that the proton diffusivity which is caused by the 2.7 Å proton jump matches the actual conductivity. They claimed that 2.7 Å corresponds to the distance between oxygen atoms in a phosphate ion, therefore, this jump occurs with the rotation of PO_4^{3-} ion. However, the mechanism of the proton migration hasn't been made completely clear because the locations of protons haven't been examined for cubic structured CDP. In the vicinity of the dopant atom, protons would move differently from these in pure CDP because the dopant atoms form the distorted lattice. It is expected that a K atom makes a larger distortion than Rb even the averaged cation radii are equivalent. In the case that protons are generally sitting at the

face centered position, the protons have four nearest-neighbor cation sites. The charge potential at the proton sites may depend on the configuration of cation sites. Since both protons and cations are positive monovalent ions, the proton site in the largely shrunk lattices would not be favorable for protons other than as possible proton sites. In such a situation, the effective diffusion path of protons is fewer than undoped CDP. As the result, the proton diffusivity of K or Rb doped CDP is lower than that of undoped CDP. In respect to the change of the activation energy by doping, the proton jump from an unfavorable to a normal position seems to occur more easily than that from a normal to other normal position. Therefore, the overall activation energy can decrease by introducing such an unfavorable site.

4.4. Conclusion

The CDP-RDP system displays complete solid solubility at all temperatures above 180 °C. At intermediate temperatures, the system adopts the CDP-type monoclinic phase. At high temperatures, the materials adopt the superprotonic cubic phase of CDP. The transition temperature increases monotonically with increasing Rb content, whereas the dehydration temperature largely decreases, resulting in a narrowing of the region of stability of the cubic phase. In the case of the end-member RbH_2PO_4 compound, this phase cannot be observed under 1 atm p_{H2O} and more extreme conditions (such as high pressure) are required. While a two-phase region is expected between the monoclinic and cubic phases, the width of this region is too small for easy detection. The thermal expansion behavior is largely independent of dopant concentration, and within the single phase cubic region the cell constant obeys Vegard's law, linearly decreasing with Rb

content. The conductivity decreases by both Rb and K doping cases. The pre-exponential factor and the activation energy decreases by doping. The impact of K doping is deeper than that of Rb with the equivalent concentrations in the averaged cation radius. It suggests that the proton jumps, which are dominant on the long-range proton migration, are affected by the dopant atoms. In order to explain this phenomenon, the proton migration mechanism in cubic CDP needs to be measured precisely.

Bibliography

1 Haile, S. M., Chisholm, C. R. I., Sasaki, K., Boysen, D. A. & Uda, T. "Solid acid proton conductors: from laboratory curiosities to fuel cell electrolytes". *Faraday Discussions* **134**, 17-39, (2007).

2 Ikeda, A. & Haile, S. M. "The thermodynamics and kinetics of the dehydration of CsH_2PO_4 studied in the presence of SiO_2". *Solid State Ionics* **213**, 63-71, (2012).

3 Cowan, L. *Superprotonic Solid Acid Phase Transitions and Stability*, California Institute of Technology, (2007).

4 Louie, M. W., Kislitsyn, M., Bhattacharya, K. & Haile, S. M. "Phase transformation and hysteresis behavior in $Cs_{1-x}Rb_xH_2PO_4$". *Solid State Ionics* **181**, 173-179, (2010).

5 Martsinkevich, V. V., Ponomareva, V. G., Drebushchak, T. N., Lavrova, G. V. & Shatskaya, S. S. "Structure of $Cs_{1-x}Rb_xH_2PO_4$ solid solutions". *Inorganic Materials* **46**, 765-769, (2010).

6 Matsuo, Y., Hatori, J., Yoshida, Y. & Ikehata, S. "Rule of superprotonic phase transition in $Cs_xRb_{1-x}H_2PO_4$". *Solid State Ionics* **213**, 42-44, (2012).

7 Botez, C. E. *et al.* "High pressure synchrotron X-ray diffraction studies of superprotonic transitions in phosphate solid acids". *Solid State Ionics* **213**, 58-62, (2012).

8 Ikeda, A. & Haile, S. M. "Examination of the superprotonic transition and dehydration behavior of $Cs_{0.75}Rb_{0.25}H_2PO_4$ by thermogravimetric and differential thermal analyses". *Solid State Ionics* **181**, 193-196, (2010).

9 Izumi, F. & Momma, K. "Three-dimensional visualization in powder diffraction". *Applied Crystallography XX* **130**, 15-20, (2007).

10 Dutta, B. N. "Lattice Constants and Thermal Expansion of Silicon up to 900 °C by X-Ray Method". *Physica Status Solidi* **2**, 984-987, (1962).

11 Komukae, M., Kawashima, K. & Osaka, T. "High-temperature phase transition in RbH_2PO_4". *Journal of the Physical Society of Japan* **69**, 2076-2081, (2000).

12 Botez, C. E., Carbajal, D., Adiraju, V. A. K., Tackett, R. J. & Chianelli, R. R. "Intermediate-temperature polymorphic phase transition in KH2PO4: A synchrotron X-ray diffraction study". *Journal of Physics and Chemistry of Solids* **71**, 1576-1580, (2010).

13 Yamada, K. "Superprotonic conductor CsH_2PO_4 studied by ^{1}H, ^{31}P NMR and X-ray diffraction". *Solid State Ionics* **175**, 557-562, (2004).

14 Bronowska, W. "High-temperature phenomena in RbD_2PO_4 and CsH_2PO_4 polymeric transformations or polymorphic phase transitions?". *Materials Science-Poland* **24**, 229-236, (2006).

15 Preisinger, A., Mereiter, K. & Bronowska, W. "The Phase Transition of CsH_2PO_4 (CDP) at 505K". *Materials Science Forum* **166**, 511-516, (1994).

16 Pauling, L. *The Nature of the Chemical Bond*. (Cornell University Press, 1960).

17 Ishikawa, A. *et al.* "Proton dynamics of CsH_2PO_4 studied by quasi-elastic neutron scattering and PFG-NMR". *Solid State Ionics* **179**, 2345-2349, (2008).

18 Otomo, J. *et al.* "Effect of water vapor on proton conduction of cesium dihydrogen phosphateand application to intermediate temperature fuel cells". *Journal of Applied Electrochemistry* **35**, 865-870, (2005).

19 Boysen, D. A., Uda, T., Chisholm, C. R. I. & Haile, S. M. "High-performance solid acid fuel cells through humidity stabilization". *Science* **303**, 68-70, (2004).

Chapter 5 Phase transformation of CsH_2PO_4

5.1 Introduction

CsH_2PO_4 is an ionic crystal which is brittle and soft. After a single crystal specimen transforms with LT phase (monoclinic)→ HT phase (cubic)→LT phase, by heating up and down under humid atmosphere, a lot of micro cracks are introduced and the crystal loses its transparency. The phase transition mechanisms of metals have been studied very well. These are investigated systematically and the crystallography, kinetics, and thermodynamics of the phase transformations are revealed. However, the information of the transformation mechanism for nonmetal materials is very limited because the reports are much fewer.

The number of the experimental methods to observe the transformation of CsH_2PO_4 is not many. Especially, it is very difficult to obtain the crystallographic information for the following reasons: First, it is hard to prepare the sample which is transformed from a single or large-grain crystal of the HT phase. In the case that a LT phase crystal is used, it is not possible to observe microstructure change by LT to HT phase transition, because HT cannot be frozen to room temperature and the sample makes a second transition from HT to LT phase. Second, it is hard to observe the orientation of domains by TEM because the electron beam destroys CsH_2PO_4. Third, SEM observation is not possible at the temperature at which the cubic phase is stable.

The phase transitions of solid acid compounds are observed in many reports. The domain structure of $RbH_3(SeO_4)_2$ formed in the HT phase in the optical was reported by

Merinov [1]. The phase transition behavior of $Cs_{1-x}Rb_xH_2PO_4$ (x = 0, 0.25, 0.50, 0.75) were investigated using the crystallographic approach by Louie[2]. They tried to apply the martensitic theory [3], which describes the relation between the value of the hysteresis of phase transition and the crystal structure parameters before and after the transformation, to this compound. They found that the phase transition of this compound doesn't satisfy the relation which the theory gives.

In this study, in order to reveal the phase transition mechanism, the distribution of the domain orientation in a singly crystal CsH_2PO_4 during phase transition from monoclinic to cubic phase was observed by in-situ XRD under humidified atmosphere.

5.2 Mechanisms of Structural-phase transformation

5.2.1 Martensitic transformation[3,4]

When the austenite (high symmetry structure) phase transforms to martensite (low symmetry structure) phase, the layered microstructure is formed in the matrix domains. The nucleation of one layered domain is as fast as the sound speed. The nucleated layered domain does not glow after the nucleation. Instead, the new layered domain is formed next to the transformed domain by nucleation with different orientation. Figure 5.1 shows the schematic diagram illustrating the stages in the transformation from matrix (austenite) phase to martensite phase. In the case that the matrix domain size is not so small, and there is no interaction between individual domains, the fraction transformed, $f(t)$ is described as Equation (1).

$$f(t) = 1 - \left[1 + (1+a)bt\right]^{-\frac{a}{a+1}} \quad (1)$$

where t is time, and a, and b are constants, respectively. The layered domain width depends on temperature history, crystal structure of both austenite and martensite phases, the elastic coefficients, and so on. The value of $f(t)$ can be obtained by analyzing XRD profiles, SEM image or magnetic, electronic property with the quenched sample, or *in situ* measurements.

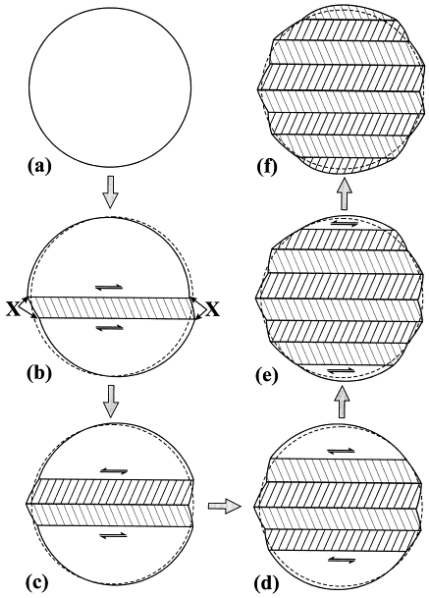

Figure 5.1. Schematic diagram illustrating the stages in the transformation of a spherical particle to self-accommodating variants. The double arrows represent the stresses in the surrounding untransformed material that oppose continued growth of a particular variant and favour the nucleation of the self-accommodating variant with an opposing shear strain. Nucleation of these self-accommodating variants are most likely to occur in the regions of stress concentration at the ends of transformed variants—i.e., in the regions marked X in (b).[5]

In the martensitic theory[3], when the domain structure of the martensite phase is described as Figure 5.2, the relation between the hysteresis, H, and the structure parameter of austenite and martensite phases, λ, is expressed as Equation (2), where λ is given as Equation (3). Figure 3 shows the plots of the factor in hysteresis, $\lambda\sqrt{(1-\lambda)\xi}$ against λ_2. λ_1, λ_2, λ_3 are called eigen values which are calculated from the transformation

matrix for austenite and martensite phases. The transformation matrix is obtained from the lattice parameters of these two phases. For this plot the other eigenvalues are determined by λ_1=0.93, and $\lambda_1\lambda_2\lambda_3$=1, and the twin system is assumed to be the one with the lowest geometric factor ξ at the given λ_2.

$$H = \frac{2\lambda\theta_c}{L}\sqrt{\frac{2\kappa\mu(1-\lambda)\xi}{l_c}} \propto \lambda\sqrt{(1-\lambda)} \tag{2}$$

$$\lambda(\lambda_2) \sim \frac{1}{2} - \frac{1}{2}\sqrt{1 - \frac{4|\lambda_2 - 1|}{|a_2 n_2|}} \tag{3}$$

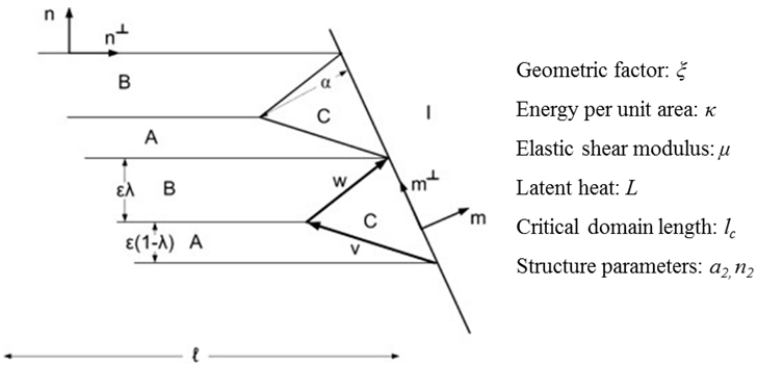

Figure 5.2. Austenite/martensite interface with a simple transition layer (C)[6]

The hysteresis is not defined precisely in the reports. Therefore, in order to discuss the result of other reports, careful examination is needed.

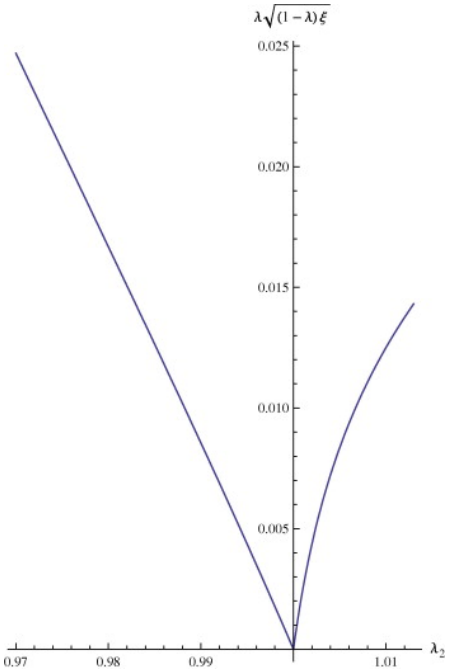

Figure 5.3. Plot of the factor in the formula for the hysteresis H vs. λ_2 that depends on lattice parameters.[3]

The deformation matrix and λ_2 is expressed as Equations (4), (5), and (6) for CsH_2PO_4.[2]

$$U = \begin{pmatrix} \gamma & \varepsilon & \varepsilon \\ \varepsilon & \alpha & \delta \\ \varepsilon & \delta & \alpha \end{pmatrix} \tag{4}$$

$$\gamma = \frac{a(\sqrt{2} + c\sin\beta)}{a_0\sqrt{2a^2 + c^2 + 2\sqrt{2}ac\sin\beta}},\ \varepsilon = \frac{ac\cos\beta}{\sqrt{2}a_0\sqrt{2a^2 + c^2 + 2\sqrt{2}ac\sin\beta}}$$

$$\alpha = \frac{1}{2\sqrt{2}a_0}\left(\frac{c(c + \sqrt{2}a\sin\beta)}{a_0\sqrt{2a^2 + c^2 + 2\sqrt{2}ac\sin\beta}} + \beta\right),\ \delta = \frac{1}{2\sqrt{2}a_0}\left(\frac{c(c + \sqrt{2}a\sin\beta)}{a_0\sqrt{2a^2 + c^2 + 2\sqrt{2}ac\sin\beta}} - \beta\right) \tag{5}$$

$$\lambda_2 = \frac{b}{a_0\sqrt{2}} \tag{6}$$

5.2.2 Nucleation and growth-typed transformation

In this mechanism, a nucleus is formed with radius r^* and probability, $e^{-\frac{\Delta G^*}{kT}}$, where ΔG^* is the free energy needed to form this critical radius, determined by the interfacial energy and volume free energy. The interfacial energy is lower at the grain surface boundary, in the vicinity of impurities or dislocations than at the inside of the grain without defects. Therefore, the nucleation happens at these preferential sites first.

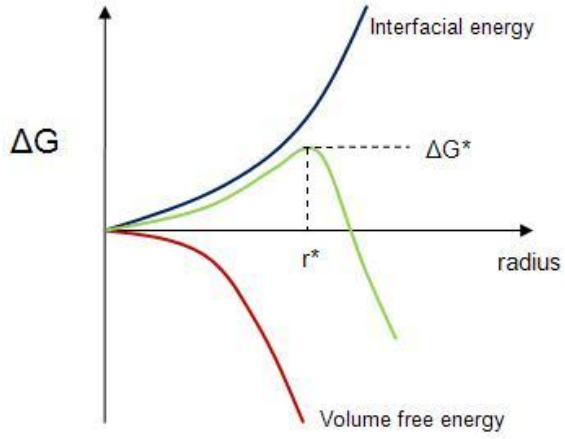

Figure 5.4. The Gibbs free energy (G) on the crystal size. Below a critical radius (r^*), a reversible process occurs; for $r > r^*$ the process becomes irreversible.[7]

The fraction transformed, $f(t)$, is described by Kolmogorov-Johnson-Mehl-Avrami equation as Equation (7)

$$f(t) = 1 - \exp(-At^n) \tag{7}$$

where t is time, A is a constant related to the Gibbs energy of grain growth and the number of nucleation sites, and n is the grain growth geometry.

5.2.3 Recrystallization

Though recrystallization is not phase transformation, this phenomenon should be remarked, because the temperature range at which the phase transition occurs (227 °C) is very close to the melting temperature (315 °C) of CsH_2PO_4 as $T_s = 0.85T_m$. It is known that the typical recrystallization temperature for metal compounds is $0.6T_m$. It depends on the concentration of the defects, the inner strain energy, and the area of grain boundaries. For ceramic materials, the inner strain energy is released by forming clacks, the preference sites in are the vicinity of clacks and grain boundaries. The angle between the crystal orientation of the nucleus which formed by recrystallization and that of the neighbor grain can be relatively large. Therefore, right after recrystallization, the grain orientation distributes randomly with some preference.

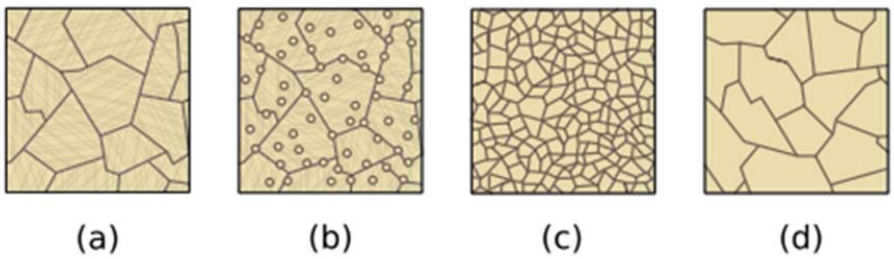

Figure 5.5. Recrystallization of a metallic material (a → b) and crystal grains growth (b → c → d)[8]

The kinetics of recrystallization are similar to the nucleation and growth-type phase transformation which is described in the previous section.

5.3 Experimental method

A single crystal of CsH_2PO_4 (40×20×5 mm^3) is obtained by slowly evaporating water from the aqua solution of CsH_2PO_4. The crystal was cut and formed to be a thin plate in size of 5×5×0.5 $mm^3$for in-situ XRD observation. The orientation of the prepared single crystal plate sample was (100). In-situ XRD measurement was carried out under humidified atmosphere using the home-made sealed high temperature stage which is described in Chapter 2 and 4. The temperature program of the measurement is shown in figure 5.6.

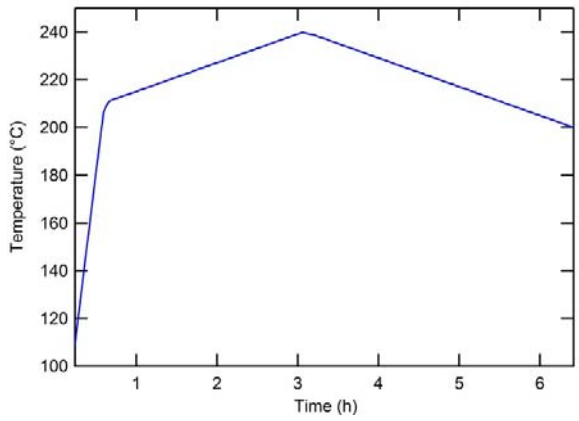

Figure 5.6 Temperature history of in-situ XRD measurement

5.4 Result and discussion

Figure 5.7 shows XRD profiles which were obtained by elevating the temperature of the single crystal sample from room temperature to 240 °C, and Figure 5.8 shows those obtained by cooling.

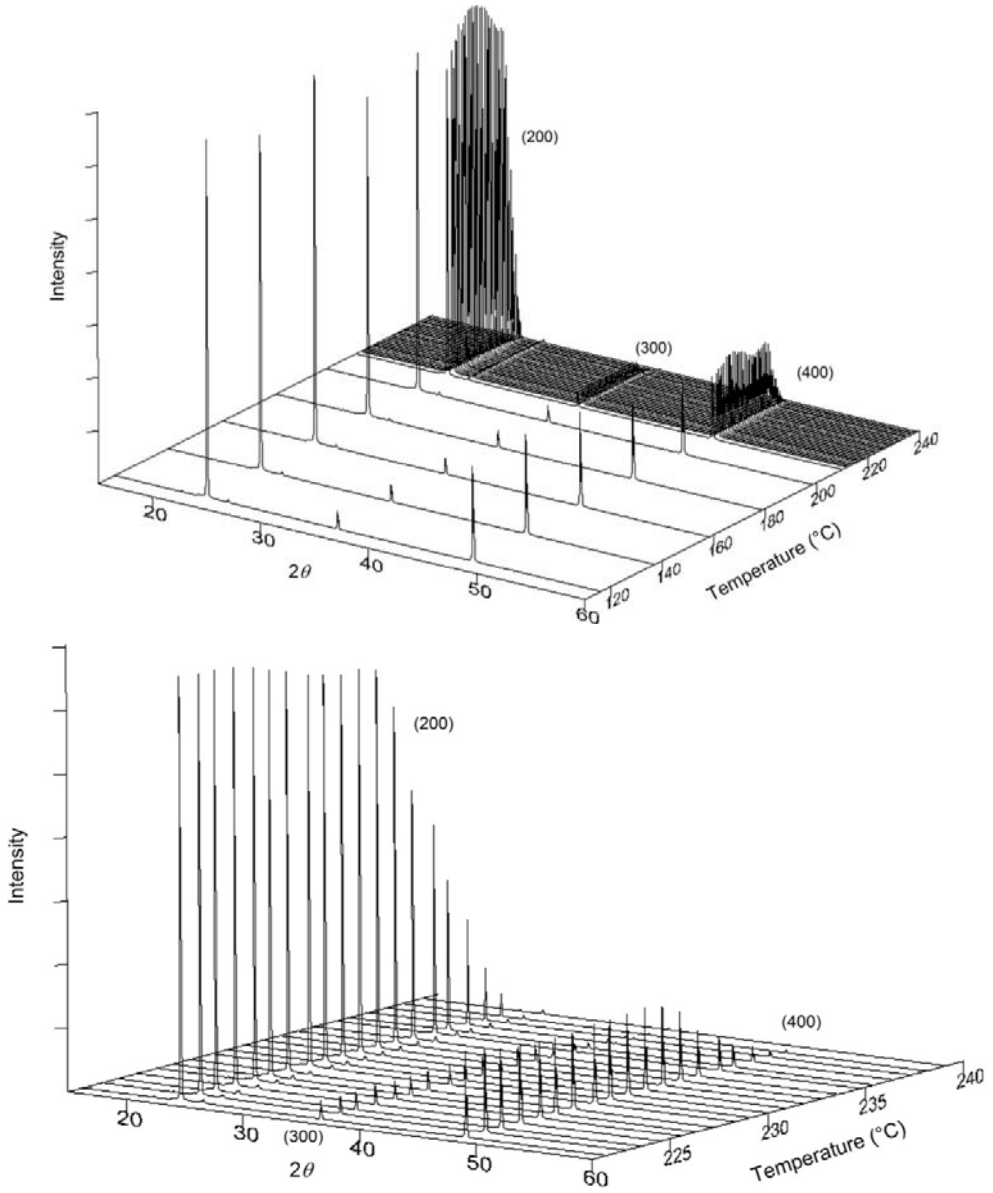

Figure 5.7. XRD profiles of single-crystal CsH_2PO_4 with elevating temperature. (top) Overview and (bottom) closer view around phase transition temperature

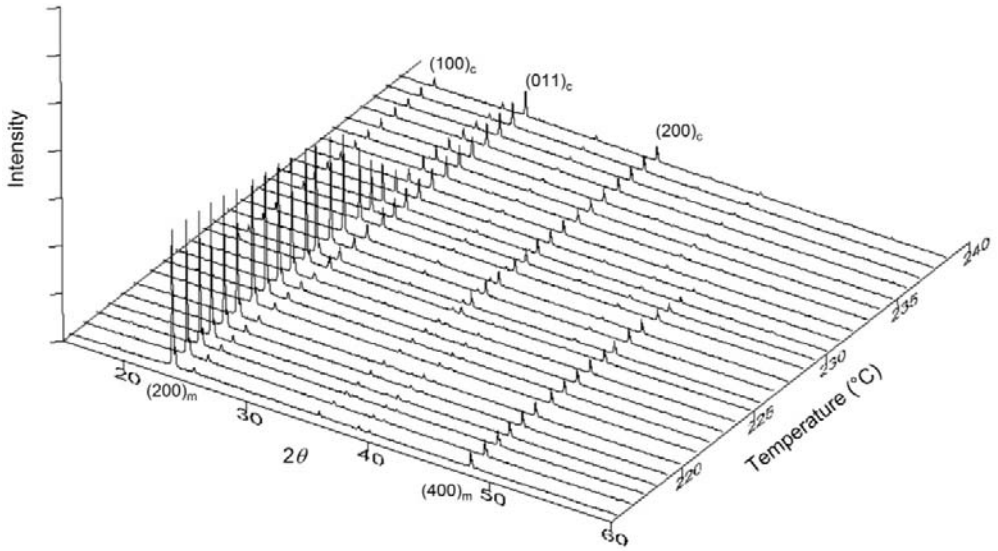

Figure 5.8. XRD profiles of single-crystal CsH_2PO_4 with cooling. The full scale of the intensity is 1/10 of Figure 5.7.

The strong peaks from the single crystal kept their intensity until phase transition started at 232 °C. The intensity decreases with elevating temperature above 232 °C, then the peak almost disappears at 238 °C. Figure 5.9 shows the change of the peak areas for monoclinic (200) and (400) directions with heating and cooling sample.

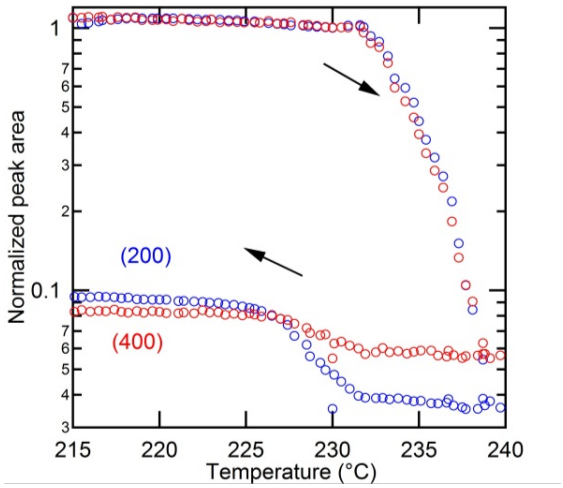

Figure 5.9. The normalized peak areas for (200) and (400) orientation with thermal cycle

It turns out that only 10% of the domains could keep their orientation. By powder XRD analysis, we can roughly estimate the trend of the distribution. Figure 5.10 (top) shows the XRD profiles of CsH_2PO_4 at around 220°C. The red curve is before transition, blue one is after transition (monoclinic→cubic→monoclinic), and the black one is obtained from powder sample as a reference. The bottom one is that of the cubic phase.

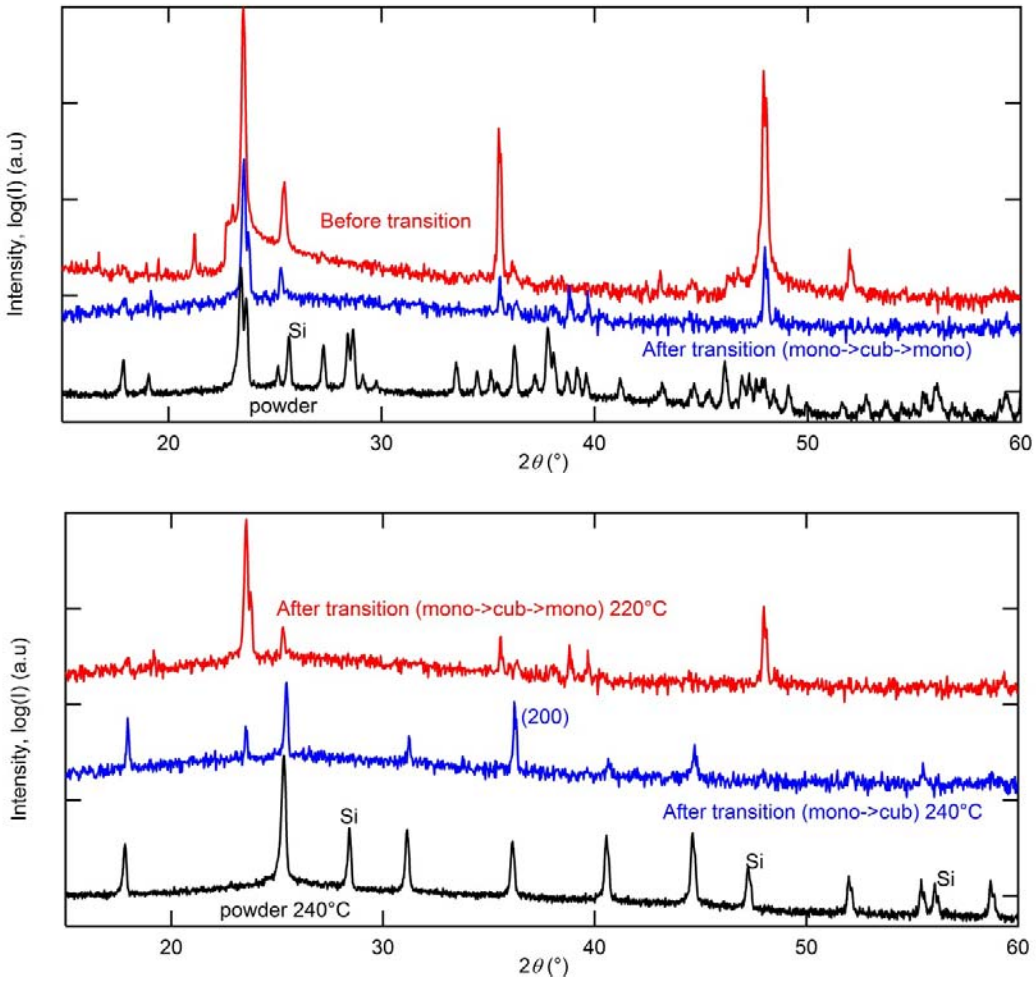

Figure 5.10. XRD profiles of (top) monoclinic phase and (bottom) cubic phase

Compared to the powder profile, the (200) and (400) peaks are larger than other peaks in the profile for the cubic phase, and the (200), (300), (400) peaks are much larger than others for the monoclinic phase. Therefore, the preferential orientation for both cubic and

monoclinic phases is (100). The Equation (8) gives the orientations of the transformed planes from $(100)_m$ by transformation matrix U_i.

$$(1 \quad 0 \quad 0)_m U_i^{-1} = (1 \quad 0.096 \quad 0.096)_c, (1 \quad 0.146 \quad 0.074)_c \tag{8}$$

The angle between $(100)_c$ and $(1\ 0.096\ 0.096)_c$ is 7.7°, and $(1\ 0.146\ 0.074)_c$ is 9.3°. Therefore, the formation of $(100)_c$ grains are expected to be the preferential orientation of the matrix crystal. Table 5.1 shows the volume fraction of the domains with specific orientation which were normalized by the amount of (200) domains. The quantities are estimated from each peak area of the single crystal profile by normalizing with the powder profile. It was assumed that the powder profile was obtained from domains with randomly distributed orientation. The distribution of the domain orientation is shown in Figure 5.11.

Table 5.1. The quantity of the domains with specific orientation. The normalized peak areas for powder and single crystal are shown as well.

Peak (hkl)	Angle between (100)	I(%) for powder	I(%) for single crystal	Quantity (%)
(100)	0	11.7	21.0	42.9
(110)	45	100	100	23.9
(111)	54.7	12.8	9.5	17.7
(200)	**0**	**11.9**	**49.8**	100
(210)	26.6	15.5	5.7	8.8
(211)	35.3	18.2	15.9	20.9

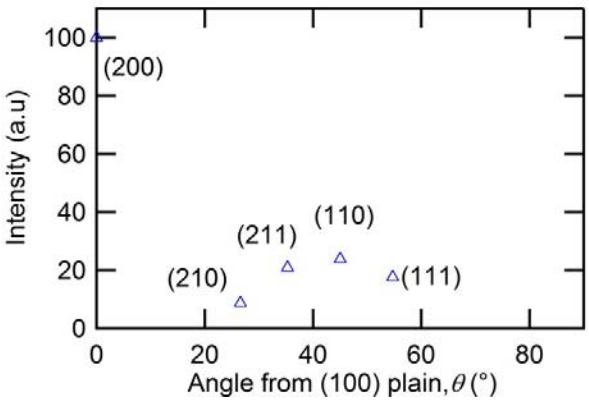

Figure 5.11. The distribution of domain orientation after transformation from monoclinic to cubic

Though the information of the distribution of domain orientation is limited, it seems that the volume fraction of the domains largely tilted from preferential orientation is not small. It is expected that most transformed domains have preferential orientation by martensite transition. Therefore, it is considered that the phase transition in CsH_2PO_4 is not simple martesite transformation. Probably, after formation of a cubic domain, it forms micro clacks. Then the whole system transforms with recrystallization events.

5.5 Conclusion

In situ XRD measurement was carried out using single crystal CsH_2PO_4 in order to study the phase transformation mechanism of this compound. A plate-like single crystal with (100) orientation was prepared, and the phase transition was observed by heating and cooling with ramp rate of 0.2 K/min. From the obtained XRD profile—the after first phase transition (monoclinic→cubic)—the distribution of the domain orientation was estimated. It was found that (100) is the preferential orientation after phase transition, however, the volume fraction of the domains with other orientations is not ignorable. Therefore, it is considered that the phase transformation in CsH_2PO_4 is not

simple martensitic, but that some other event, such as recrystallization, happens during the transition process.

Bibliography

1 Merinov, B. V., Haile, S. M. & Bismayer, U. "Crystal structure of the "intermediate" phase of the protonic conductor $Rb_3H(SeO_4)_2$". *Solid State Ionics* **146**, 355-365, (2002).

2 Louie, M. W., Kislitsyn, M., Bhattacharya, K. & Haile, S. M. "Phase transformation and hysteresis behavior in $Cs_{1-x}Rb_xH_2PO_4$". *Solid State Ionics* **181**, 173-179, (2010).

3 Zhang, Z. Y., James, R. D. & Muller, S. "Energy barriers and hysteresis in martensitic phase transformations". *Acta Materialia* **57**, 4332-4352, (2009).

4 Christian, J. W. *The theory of transformations in metals and alloys : an advanced textbook in physical metallurgy*. 2d edn, (Pergamon Press, 1975).

5 Kelly, P. M. & Francis Rose, L. R. "The martensitic transformation in ceramics — its role in transformation toughening". *Progress in Materials Science* **47**, 463-557, (2002).

6 Papandrew, A. B., Chisholm, C. R. I., Elgammal, R. A., Ozer, M. M. & Zecevic, S. K. "Advanced Electrodes for Solid Acid Fuel Cells by Platinum Deposition on CsH_2PO_4". *Chemistry of Materials* **23**, 1659-1667, (2011).

7 Wikipedia, http://en.wikipedia.org/wiki/Nucleation

8 Wikipedia, http://wkp.maluke.com/en/Recrystallization_(metallurgy)

Appendix A Phase behavior of anion doped cubic CsH_2PO_4

A.1. CsH_2PO_4–$CsHSO_4$ system

For the substitution of the PO_4^{3-} site, it is reported that $CsHSO_4$ and CsH_2PO_4 make solid solution of cubic phase $Cs(H_2PO_4)_{1-x}(HSO_4)_x$, at least in the range of $x < 0.67$ [1-5]. It is reported that at room temperature, CsH_2PO_4 and $CsHSO_4$ make intermediate phases $Cs_2(H_2PO_4)(HSO_4)$, $Cs_5(H_2PO_4)_2(HSO_4)_3$, $Cs_3(H_2PO_4)(HSO_4)_2$, and $Cs_6(H_2PO_4)(HSO_4)_5$. Figure A.1 shows the suggested phase diagram based on the reported phase transition and melting temperature by DSC measurements [3,6]. Table A.1 shows the crystal structures at RT and HT, and the phase transition and melting temperatures for $Cs(H_2PO_4)_{1-x}(HSO_4)_x$ with various x.

Table A.1. The crystal structure and T_s, T_m of $Cs(H_2PO_4)_{1-x}(HSO_4)_x$ with various x

x	Structure at RT	T_s (°C)	Structure at HT	T_m(°C)	Ref
0	P21/m	227	Pm3m	315	
0.5	C2/c	72	Pm3m		Yamane [3]
0.6	C2/c	99	Pm3m		Yamane [3]
0.67	$P2_1/n$	131	Pm3m		Yamane[3]
0.75	$P2_1/n$	132	Pm3m		Yamane[3]
0.83	C2/c	123	Pm3m+ I4/amd	175	Chisholm[6]
0	$P2_1/c$	142	I4/amd	205	Chisholm[6]

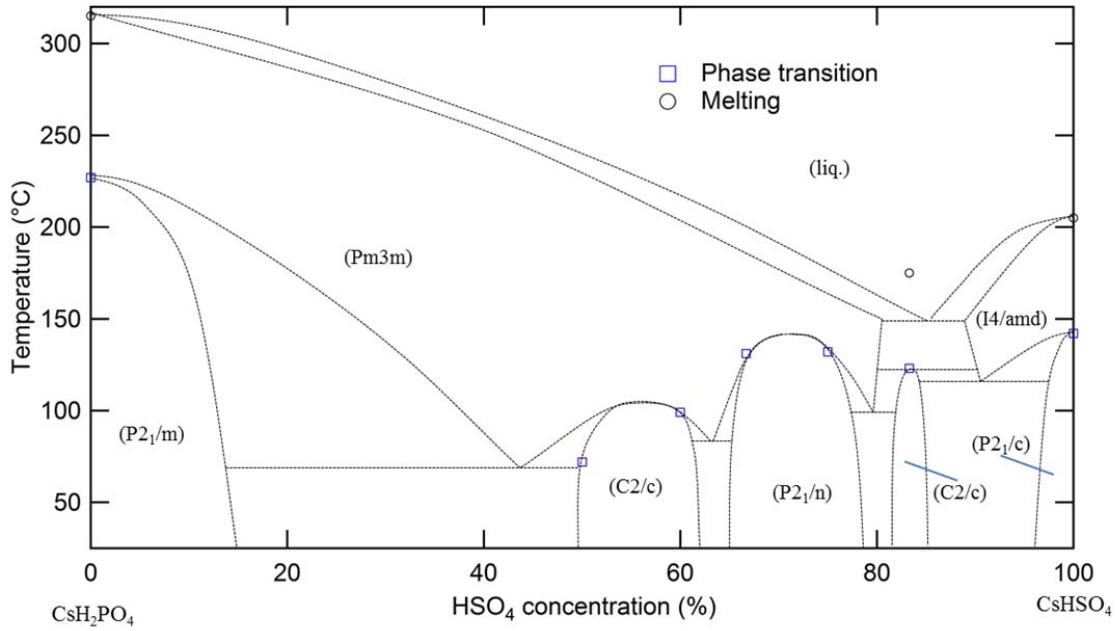

Figure A.1. The suggested phase diagram of CsH_2PO_4–$CsHSO_4$ system

In this phase diagram, I assumed that all pairs of compounds which are next to each other are eutectic. Since C2/c phase with x = 0.5~0.6 has a low phase transition temperature, it is expected that the eutectic temperature between $P2_1/m$ and C2/c phases is very close to room temperature. The lattice parameter of the quenched cubic phase and conductivity (*in situ*) were reported[3]. They claimed that the lattice parameter linearly decreases and conductivity increases with increase of x. The lattice parameters of the cubic phase at the temperature at which the cubic phase is stable have not been reported systematically.

A.2. CsH_2PO_4–CsI system

Iodine is also a good candidate for the substitution of the PO_4^{3-} site, because CsI has a cubic (Pm3m) structure. In this study, the phase diagram of the CsH_2PO_4–CsI system is determined by EDS and *in situ* XRD measurements. Then the effects of the

doping in structure and conductivity were investigated. All experimental methods are explained in Chapter 4. Figure A.2 shows the phase diagram of the CsH_2PO_4–CsI system in the vicinity of the cubic phase.

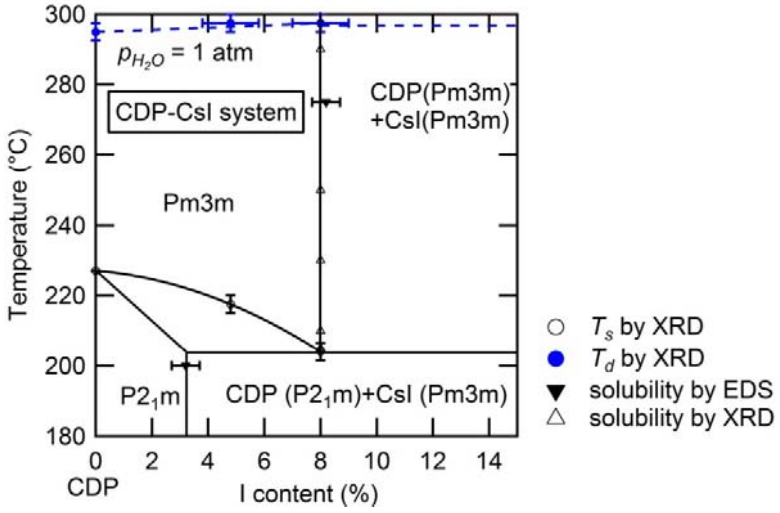

Figure A.2 he phase diagram of the CsH_2PO_4–CsI system

The solubility of iodine is around 8 at.% for cubic phase. The phase transition temperature, T_s decreases with iodine concentration up to 202 ± 2 °C. The dehydration temperature, T_d is similar to that of undoped CsH_2PO_4.

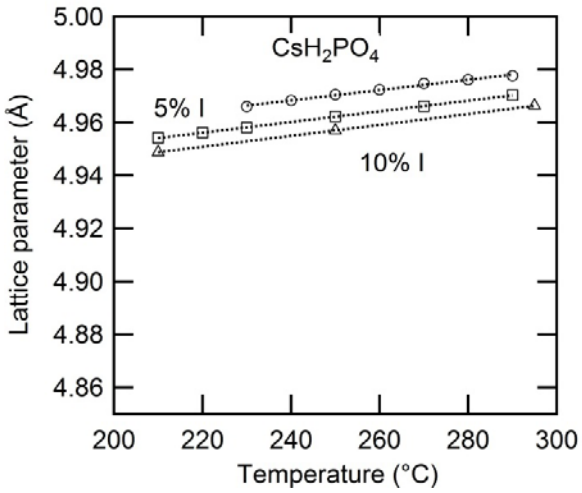

Figure A.3. The lattice constant of iodine-doped CsH_2PO_4

Table A.2. The thermal expansion coefficients of doped CDP

Compounds	A ($10^{-5}K^{-1}$)	a_0 (Å)	T (°C)
undoped	3.92(11)	4.9724(2)	230-290
5 at.%I	4.05(3)	4.9640(2)	210-295
10 at.%I (8 at.%I in cubic)	4.16(2)	4.9591(2)	210-295

The lattice parameters of 5 and 10 at.% I-doped CsH_2PO_4 at each temperature are shown in Figure A.3. The thermal expansion coefficients are calculated from obtained lattice parameters (Table A.2). There was no obvious change with doping. It was found that lattice parameter linearly decreases with iodine concentration.

The conductivity of 5 at.% I is shown in Figure A.4. It is slightly lower than undoped CDP. The activation energy of the proton diffusivity of this compound is calculated as 33.5 kJ/mol. It is smaller than that of undoped CDP.

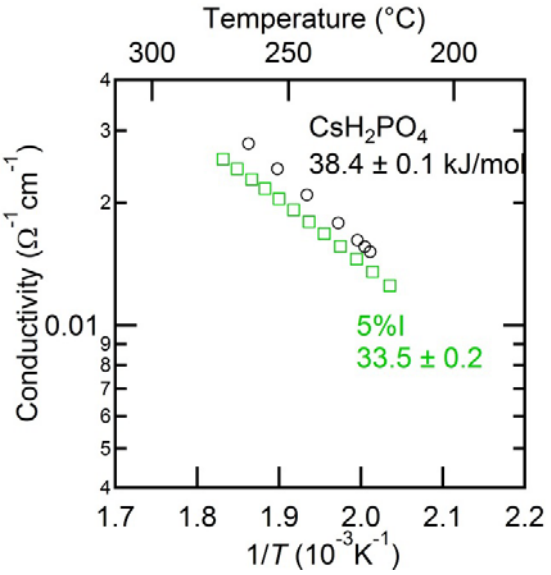

Figure A.4. The conductivity of 5 at.%I doped CsH_2PO_4

A.3 Conclusion

Both CsH_2PO_4-$CsHSO_4$ and CsH_2PO_4-CsI systems are eutectic and the cubic phase of these systems are stable at lower temperature region than the phase transition temperature of undoped CsH_2PO_4. Unfortunately, neither doped CDP is stable for practical use, because SO_4 ions react with hydrogen and I ions react with oxygen gas at the cubic stable temperature region. The lattice parameter linearly changes in both cases. Therefore, it is expected that the lattice parameter of cubic CDP is expressed as Equation (1)

$$a(r_c, r_a, T) = a_0(r_c + r_{c0})(r_a + r_{a0})\left\{A(T + T_0) + B(T + T_0)^2\right\} \quad (1)$$

where r_c, r_a, and T are the averaged cation and anion ionic radius, respectively. A and B are the thermal expansion parameters. The conductivity of I-doped CDP was observed and it was slightly lower than undoped CDP.

Bibliography

1 Chisholm, C. R. I. & Haile, S. M. "Superprotonic behavior of $Cs_2(HSO_4)(H_2PO_4)$ - a new solid acid in the $CsHSO_4$-CsH_2PO_4 system". *Solid State Ionics* **136**, 229-241, (2000).

2 Chisholm, C. R. I. & Haile, S. M. "Structure and thermal behavior of the new superprotonic conductor $Cs_2(HSO_4)(H_2PO_4)$". *Acta Crystallographica Section B-Structural Science* **55**, 937-946, (1999).

3 Yamane, Y., Yamada, K. & Inoue, K. "Superprotonic solid solutions between $CsHSO_4$ and CsH_2PO_4". *Solid State Ionics* **179**, 483-488, (2008).

4 Haile, S. M., Lentz, G., Kreuer, K. D. & Maier, J. "Superprotonic Conductivity in $Cs_3(HSO_4)_2(H2PO_4)$". *Solid State Ionics* **77**, 128-134, (1995).

5 Haile, S. M. & Calkins, P. M. "X-ray diffraction study of $Cs_5(HSO_4)_3(H_2PO_4)_2$, a new solid acid with a unique hydrogen-bond network". *Journal of Solid State Chemistry* **140**, 251-265, (1998).

6 Chisholm, C. R. I. *Superprotonic Phase Transitions in Solid Acids: Parameters affecting the presence and stability of superprotonic transitions in the $MHnXO_4$ family of compounds (X=S, Se, P, As; M=Li, Na, K, NH_4, Rb, Cs)* Ph.D thesis, California Institute of Technology, (2002).